



ARISTOTLE UNIVERSITY OF THESSALONIKI
SCHOOL OF GEOLOGY
DEPARTMENT OF GEOPHYSICS

PARASKEVI IO IOANNIDI
Graduate Geologist

SOURCE CHARACTERISTICS OF EARTHQUAKES ALONG THE
WESTERN HELLENIC ARC

MASTER THESIS

THESSALONIKI
2014

PARASKEVI IO IOANNIDI
Graduate Geologist

SOURCE CHARACTERISTICS OF EARTHQUAKES ALONG THE
WESTERN HELLENIC ARC

Submitted to the School of Geology within the framework of the Postgraduate
Programme “Applied and Environmental Geology”
Geophysics Department
Date of Oral Examination:

Supervising and examining committee

Eleftheria Papadimitriou.....Professor of Seismology (Supervisor)

Elisa Buforn PeiróProfessor of Physics of the Earth (Member)

Vassilios Karakostas.....Professor of Seismology (Member)

Reference Number of Scientific Annals of the School of Geology N^o: 836

© Paraskevi Io Ioannidi, 2014

All Rights Reserved

SOURCE CHARACTERISTICS OF EARTHQUAKES ALONG THE WESTERN HELLENIC ARC

No part of this publication may be reproduced, stored or distributed for commercial purposes. Reproduction, storage and distribution for non profitable educational or scientific purposes are permitted with the limitation of reference to the source and the preservation of the current message. Queries regarding non profitable permission requests must be appended to the author.

Opinions and conclusions included in this document express the author and do not correspond to the official attitude of A.U.Th.

Preface

In the present study, an effort is made to investigate the seismic source parameters of the Western Hellenic arc, processing seismograms from earthquakes generated in the particular area the last decade. Six were the largest events that struck during this period of time: the first ($M_w=6.0$) occurred on March 17, 2004 at 35 km depth, south of the Island of Crete, the second one ($M_w=6.6$) on January 8, 2006 at ~ 70 km. On February 2008 three strong earthquakes ruptured ~ 30 km of the western Hellenic Trench, south of Peloponnese, the February 14, 2008 $M_w=6.6$, the February 14, 2008 $M_w=6.0$ and the February 20, 2008 $M_w=5.9$ events. The most recent earthquake ($M_w=6.6$) occurred on October 13, 2013 at a depth of ~ 40 km, west of the Island of Crete. All seismograms were processed with the teleseismic bodywave inversion program developed by Kikuchi and Kanamori (2003).

The study starts with a brief, introductory reference to the general seismotectonic framework of Greece, the crustal movements and seismicity observed, focusing in particular on the seismotectonics of the under study region, the Wadatti-Benioff zone and previous studies in the area.

In the second chapter, the theoretical background of focal mechanism, seismic moment tensor inversion and spectral analysis is given.

The following chapter refers to the application of teleseismic bodywave inversion method to the selected earthquakes. Fault plane constraints are employed for all events and the final source time function is determined, along with the fault plane solution.

The fourth chapter presents the spectral analysis for two of the earthquakes, the January 8, 2006 $M_w=6.6$ Kythera earthquake and the October 12, 2013 $M_w=6.5$ W Crete earthquake. The first event was chosen because it is the greatest in magnitude that is studied here and the second event because of its recent occurrence and the fact that it has not been fully examined yet.

Finally, the last chapter presents a discussion over interesting findings and drawbacks during the elaboration of the study and then briefly concludes with final parameters obtained for every earthquake, comparing them to the known seismotectonic regime of the under study area.

At the end of the present study, references and supplementary material are cited. The last comprises data processing and additional teleseismic station tables that were excluded from the main part of the study.

Acknowledgements

This work has been accomplished at the Geophysics Department, School of Geology, Aristotle University of Thessaloniki with the collaboration of the Faculty of Physical Sciences, Complutense University of Madrid within the Framework of the LLP Erasmus Programme.

First of all, I would like to express my gratitude to my supervisor Professor Eleftheria Papadimitriou for her guidance, caring and constant support. She helped me grow from student and laid the foundation to become a future researcher. Additionally, it was her bilateral agreement with Professor Elisa Buforn Peiró that gave me the opportunity to work abroad part of my M.Sc. Thesis. With that being said, I would like to give my sincere thanks to my supervisor in Complutense University of Madrid, Professor Elisa Buforn Peiró for accepting me as a M.Sc. Erasmus student, as well as for her patient help, guidance and encouragement throughout my stay there. The content of the present study was built after her decisive suggestions. Moreover, I am grateful to Professor Vassilios Karakostas for his interest in my progress and his important insight any time it was needed.

In addition, I wish to express my gratitude to Anastasia Kiratzi, Professor of Seismology, for her substantial contribution to the elaboration of the spectral analysis which, without her help, would have been difficult for me to achieve. I am also grateful to all the professors and employees at the Department of Geophysics for their concern in my progress and help any time I needed it. Thank are also deserved to all the M.Sc. and Ph.D. students. Particularly, I thank my friend and colleague of the Department of Physics of the Earth, Astronomy and Astrophysics Marta Carranza for her support during my stay in Spain and her interest in my progress. In addition, my friend and colleague Konstantinos Michailos has been encouraging me constantly since the beginning of this study, in both Universities and helped my many times during the elaboration of the present study. I thank him sincerely.

Last but not least, words cannot express how grateful I am to my family who played the most important role in my period of studies. I want to thank each and every one of them: my mother and father for their moral and financial support and all the sacrifices they made on my behalf, my sister who supported me and my family while I was away, my grandmother who made sure nothing was missing so I could work without further preoccupation. I would also like to thank all of my dearest friends who supported me in the many and long hours of elaboration of the study. Particularly, Stelios Anastasiadis has been a great encouragement for me, inciting me to strive towards my goal. I thank all of you. It would have been impossible to make it without you.

Data and Resources

The facilities of IRIS Data Services, and specifically the IRIS Data Management Center, were used for access to waveforms, related metadata, and/or derived products used in this study. IRIS Data Services are funded through the Seismological Facilities for the Advancement of Geoscience and EarthScope (SAGE) Proposal of the National Science Foundation under Cooperative Agreement EAR-1261681. Global Seismographic Network (GSN) is a cooperative scientific facility operated jointly by the Incorporated Research Institutions for Seismology (IRIS), the United States Geological Survey (USGS), and the National Science Foundation (NSF), under Cooperative Agreement EAR-1261681.

Fault plane solutions from P-wave polarities were obtained with Program MECTSA (Udias et al., 1984). Bodywave inversion was carried out with the Kikuchi and Kanamori algorithm (M. Kikuchi and H. Kanamori, Note on Teleseismic Body-Wave Inversion Program, <http://www.eri.u-tokyo.ac.jp/ETAL/KIKUCHI/>). Spectral analysis was accomplished with SAC (Goldstein et al., 2003; Goldstein and Snoke, 2005). Focal mechanism solutions used for the creation of the maps were taken from the Geophysics Department of the Aristotle University of Thessaloniki (<http://geophysics.geo.auth.gr>) and for the creation of the maps the Generic Mapping Tools version 5.1.1 (Wessel and Smith, 1998, <http://gmt.soest.hawaii.edu/>) was used. Use of Matlab® (release R2010b) was also used to plot some of the figures. This work was partially supported by the Commission of the European Communities within the Framework of the LLP Erasmus Programme.

CONTENTS

| | |
|---|-----|
| Preface | i |
| Acknowledgements | iii |
| Data and Resources | iv |
| CHAPTER 1: SEISMOTECTONIC PROPERTIES..... | 1 |
| 1.1 Introduction | 1 |
| 1.2 Seismotectonic regime | 1 |
| 1.3 Wadati-Benioff zone in the area | 3 |
| 1.4 Slab pull and rollback in the Aegean | 4 |
| 1.5 Focal mechanism distribution..... | 5 |
| 1.6 Previous studies in the area..... | 7 |
| CHAPTER 2: THEORETICAL BACKGROUND | 9 |
| 2.1 Focal mechanism..... | 9 |
| 2.1.1 Fault geometry | 9 |
| 2.2 Equivalent body forces | 12 |
| 2.2.1 Radiation pattern | 14 |
| 2.2.2 Fault plane solution..... | 16 |
| 2.3 Source Time Function..... | 16 |
| 2.4 Seismic moment tensor inversion..... | 18 |
| 2.4.1 Theory..... | 18 |
| 2.4.2 Application | 19 |
| 2.5 Spectral analysis..... | 20 |
| CHAPTER 3: FAULT PLANE SOLUTIONS THROUGH TELESEISMIC WAVEFORM MODELLING..... | 25 |
| 3.1 Introduction | 25 |
| 3.2 March 17, 2004 $M_w=6.0$ Crete earthquake | 26 |
| 3.2.1 Focal mechanism determination from P-wave polarities | 26 |
| 3.2.2 Depth determination..... | 27 |
| 3.2.3 Constraints on the fault plane | 31 |
| 3.2.4 Results | 33 |
| 3.3 January 08, 2006 $M_w=6.6$ Kythera earthquake..... | 34 |
| 3.3.1 Focal mechanism determination from P-wave polarities | 34 |

| | | |
|---|--|------|
| 3.3.2 | Depth determination..... | 35 |
| 3.3.3 | Constraints on the fault plane | 35 |
| 3.3.4 | Results | 37 |
| 3.4 | February 2008 – Methoni earthquakes..... | 38 |
| 3.4.1 | 14 February 2008 $M_w=6.6$ earthquake..... | 39 |
| 3.4.2 | 14 February 2008 $M_w=6.0$ earthquake..... | 43 |
| 3.4.3 | 20 February 2008 $M_w=5.9$ earthquake..... | 48 |
| 3.5 | October 12, 2013 W Crete earthquake | 52 |
| 3.5.1 | Focal mechanism determination from P-wave polarities | 52 |
| 3.5.2 | Depth determination..... | 53 |
| 3.5.3 | Constraints on the fault plane | 54 |
| 3.5.4 | Results | 55 |
| CHAPTER 4: FAULT PARAMETERS THROUGH SPECTRAL ANALYSIS | | 57 |
| 4.1 | Introduction | 57 |
| 4.1.1 | January 8, 2006 $M_w=6.6$ Kythera earthquake | 58 |
| 4.1.2 | October 12, 2013 $M_w=6.5$ W Crete earthquake | 60 |
| CHAPTER 5: DISCUSSION – CONCLUSIONS..... | | 63 |
| 5.1 | Discussion | 63 |
| 5.2 | Summary of the results | 64 |
| REFERENCES | | I |
| APPENDIX A: DATA TREATMENT | | XI |
| Introduction | | XI |
| Data acquisition and preparation | | XI |
| Teleseismic bodywave inversion..... | | XIII |
| General inversion | | XIII |
| Fixed mechanism inversion..... | | XVI |
| APPENDIX B: TELESEISMIC STATIONS..... | | XVII |

CHAPTER 1: SEISMOTECTONIC PROPERTIES

1.1 Introduction

The aim of the present study is the definition of source parameters of strong earthquakes along the western part of the Hellenic arc, where subduction of the oceanic Mediterranean lithosphere under the Aegean microplate takes place. The methods employed for the determination of source parameters, such as source time function, focal depth, magnitude, scalar moment and fault dimensions, were teleseismic bodywave inversion and spectral analysis of far-field displacement.

1.2 Seismotectonic regime

The broader Aegean area is located in the Alpine-Himalayan zone, therefore exhibiting high seismicity rates, with 60% of the seismic energy radiated in Europe and 2% of the global seismicity, with earthquakes up to $M_W=8.3$ (Papazachos, 1990). Because of its position along the convergence boundary of the Eurasian and African plates, it constitutes the last remnant part of Tethys that has not yet participated in the developing alpine orogenesis and therefore represents the still undeformed African plate margin. This singularity of the Aegean area gives the opportunity of studying seismotectonic phenomena in the offing.

The morphotectonic features that it exhibits are equivalent to those of an island arc that lies in the region of subduction of an oceanic plate under a continental one. Its most prominent features from north to south are the following (Papazachos *et al.*, 1991; Fig. 1.1):

- The Back-arc Aegean area, which includes the Aegean Sea, the mainland of Greece, Albania, FYROM, south Bulgaria and western Turkey and is created by tensional forces behind the arc,
- The inner volcanic arc that is formed by the successive volcanic centres of Sousaki, Methana, Milos, Santorini and Nisiros. These volcanoes are connected to the subduction and melting of the rocks of the African plate at a depth of 150 km, behind the convergence boundary of the two plates,
- The outer sedimentary arc, which includes the western Hellenides mountain range of continental Greece, the island of Crete and the island complex of Dodecanese,
- The Hellenic Trench, an undersea depression of maximum depth of up to 5 km that extends from the Ionian Sea in the west until the south of Crete and Rhodes. Its maximum depth has been found at the Ionian Sea (4500 m), a depth that is also the biggest found in the entire Mediterranean Sea.

- The Mediterranean Ridge, an undersea compressional uplift of the crust that crosses the eastern Mediterranean southern of the Hellenic Trench and parallel to the Hellenic Arc.

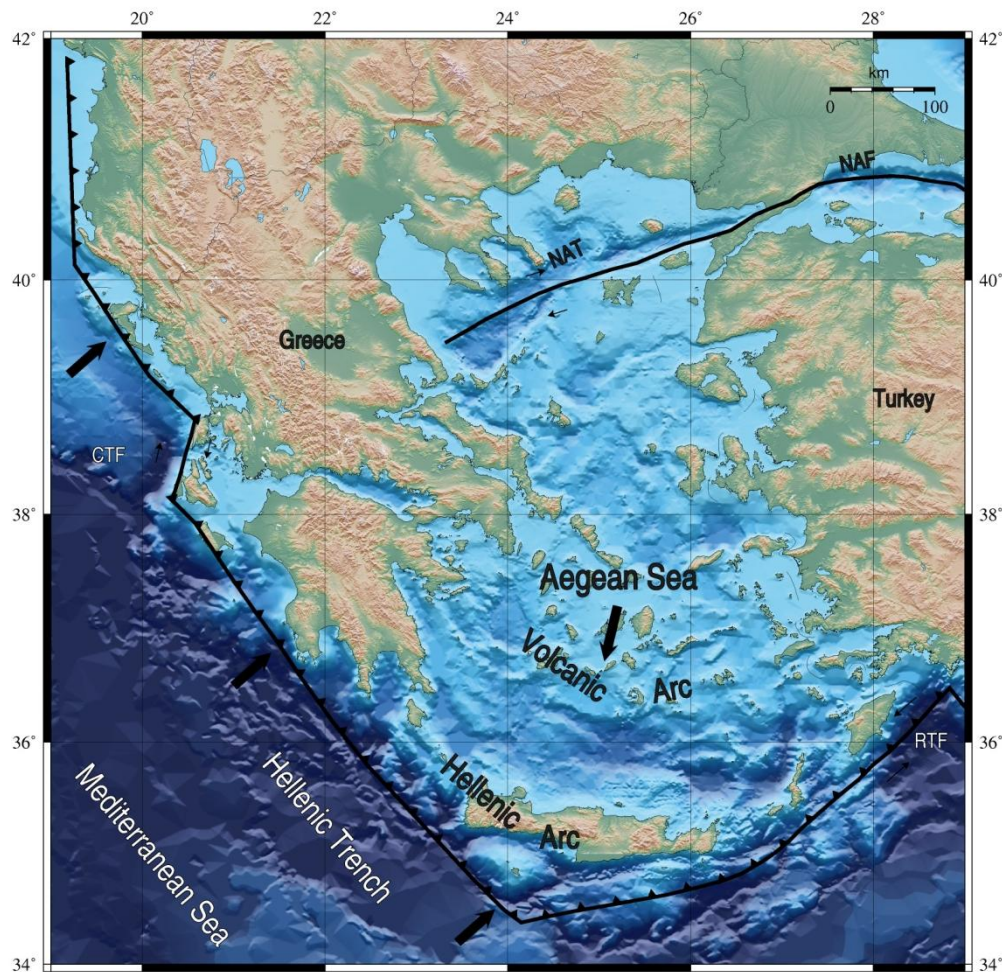


Fig. 1.1 Main features of the broader Aegean area. From the inner to the outer arc, the Aegean Sea, the volcanic arc, the Hellenic arc and the Hellenic Trench are shown. NAT: North Aegean Trough, NAF: North Anatolia Fault, CTF: Cephalonia Transform Fault, RTF: Rhodes Transform Fault.

During the aforementioned collision of the African plate with Eurasia (McKenzie, 1972, 1978; Jackson and McKenzie, 1988; Jackson, 1994; Papazachos and Kiratzi, 1996; Papazachos *et al.*, 1988; McClusky *et al.*, 2000; Kiratzi and Louvari, 2003) the continental block of Arabia which has been detached from Africa through the Red Sea opening, is moving northwards and with a velocity greater than that of Africa. Therefore, the Arabian microplate is pushing the Eurasian boundary in Anatolia (Asia Minor) which in turn reacts as an independent microplate and is forced to a sinistral rotation, pushing the Aegean microplate. This last microplate is compelled to a southwestern movement, which is accommodated by the great dextral North Anatolia Fault (Fig. 1.2).

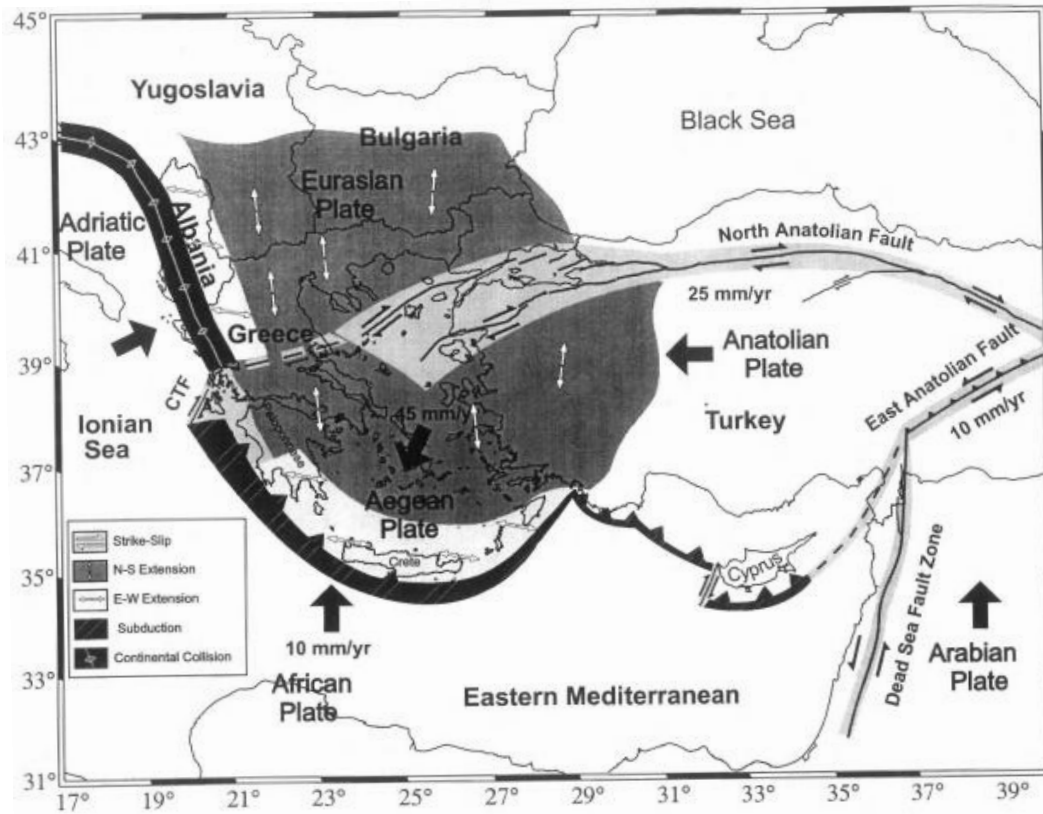


Fig. 1.2 Simplified map of the Aegean Sea and the surrounding area showing the major plates and microplates involved in the active tectonics (Papazachos *et al.*, 1998). Black arrows indicate the motion of the plates relative to Eurasia (from DeMets *et al.*, 1990; Kastens *et al.*, 1996). The small white arrows indicate the direction of internal deformation (extension) over the greater Aegean area. CTF: Cephalonia Transform Fault.

1.3 Wadati-Benioff zone in the area

The existence of the Benioff zone in southern Aegean was found by Papazachos and Comninakis (1970, 1971) who used the arrival time difference of P and PcP phases in order to determine the exact focal depth of intermediate depth earthquakes ($60 \text{ km} \leq h \leq 180 \text{ km}$). The existence of this zone was the most significant evidence for the subduction of the Eastern Mediterranean plate beneath the Aegean microplate.

Following this discovery, more precise data, such as fault plane solutions with waveform modeling (Taymaz *et al.*, 1990, Benetatos *et al.*, 2004), modern tomography methods (Papazachos and Nolet, 1997), large scale experiments of seismic methods (Bohnhoff *et al.*, 2001) showed that the Benioff zone in the southern Aegean consists of two different parts, a shallow ($h \leq 100 \text{ km}$) and a deeper one ($100 \text{ km} \leq h \leq 180 \text{ km}$).

The geometry of the zone was found by Papazachos *et al.* (2000) who suggested that the zone starts at a depth of 20 km under the outer side of the sedimentary part of the Hellenic Arc (western Peloponnese-west of Kythera-south of Crete-southeast of Rhodes) and dips toward the back-arc area where it reaches a

depth of 150 km under the volcanic arc in the southern Aegean (Fig. 1.3). Because of the occurrence of some deeper earthquakes, up to a focal depth of 180 km, the Wadati-Benioff zone can be separated into two branches, as already mentioned. The shallower part dips with an angle of 30°, whereas the deeper with an angle of 45° (both with an accuracy of 5°-10°, due to scattering of the intermediate depth seismicity). This change in dipping is in agreement with previous studies in the area (Papazachos and Nolet, 1997), although they suggested that the change of dipping occurs at shallower depths (~80 km). The writers also conclude that the Wadati-Benioff zone defines the area of coupling between the Aegean and the Mediterranean plates. This is supported by the fact that great earthquakes (up to $M_w=8.3$) occur in the shallow branch.

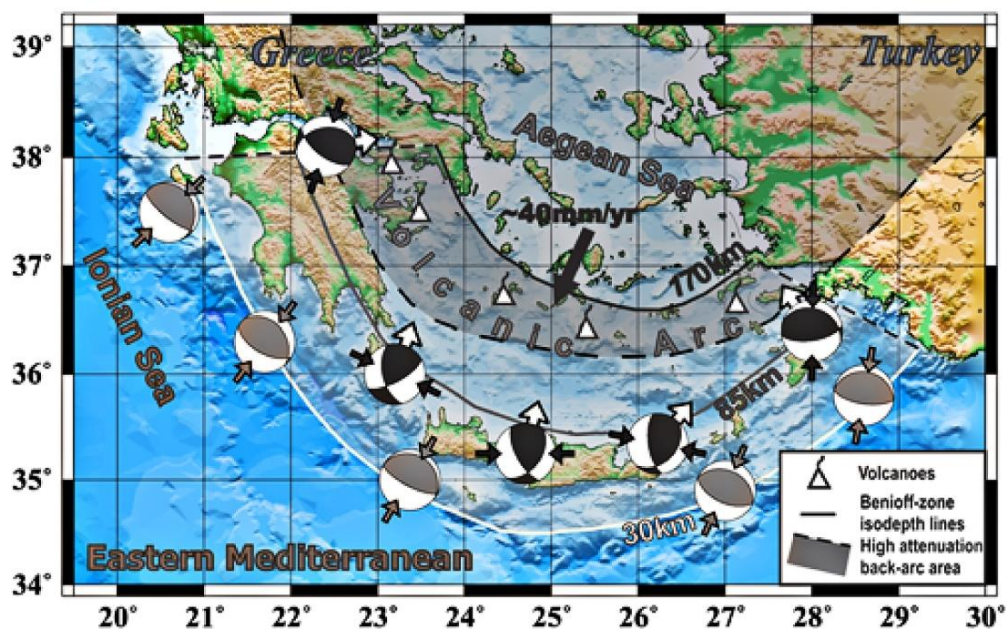


Fig. 1.3 Schematic geotectonic setting of the Hellenic subduction and its Benioff zone. The Aegean microplate is overriding the African plate at a convergence of ~35-40 mm/yr in a northeast-southwest direction (thick black arrow). Typical fault-plane solutions (Papazachos *et al.*, 2000; black and gray focal mechanism plots) are in very good agreement with the regional subduction tectonics. The shaded area roughly depicts the high-attenuation area (back arc) as identified by previous studies, clearly associated with the volcanic arc (Skarlatoudis *et al.*, 2013).

1.4 Slab pull and rollback in the Aegean

While a cold lithospheric slab enters the hot mantle, it creates negative buoyancy (a positive mass anomaly). If the slab remains attached to the surface plate, a slab pull force arises that pulls the slab downwards into the mantle (Lowrie, 2007), acting as a force toward the subduction zone. When this descending slab is long and heavy, it can sink more rapidly than the rate of plate convergence. Then the slab becomes steeper and bends away from the arc. This oceanward retreat of the trench due to the gravitational pull of the slab is mentioned as rollback and plays a major role because it explains the extensional events in an overall convergent region.

Rollback of the Aegean slab, which is triggered by the slab encountering the more viscous lower mantle, might be responsible for trench migration. This rollback would explain the extensional stress regime of the overriding plate and may have facilitated the southwestward extrusion of the Aegean plate (LePichon and Angelier, 1981; Dewey, 1988; Zhong and Gurnis, 1995; Widiyantoro *et al.*, 2004). As far as the western part is concerned, the idea of roll-back is supported by the existence of deep focus earthquakes (larger than 100 km) which indicated that the oceanic lithosphere of the Eastern Mediterranean is “sinking” in this part of the Ionian Sea, also indicated by tomographic results (Papazachos and Nolet, 1997). These results report the idea that rollback of the descending lithospheric plate towards the remaining scarp of oceanic crust beneath the Ionian Sea may cause gravitational spreading of the expanding Aegean lithosphere.

Inversion of fault mechanism for earthquakes within the dipping oceanic Mediterranean lithosphere reveals a down-dip orientation for σ_3 at a plunge of 48° trending to the north. σ_1 was found to be oriented dominantly orthogonal to the strike of the plate boundary and vary with strike of the Hellenic arc at a plunge of 39° (Bohnhoff, 2005b). This indicates that slab pull is the dominant force within the dipping African lithosphere causing gravitational instability at the southern edge of the Aegean domain and resulting in rollback of the slab (LePichon and Angelier, 1979; Jackson and McKenzie, 1988).

1.5 Focal mechanism distribution

Focal mechanism solutions account for the aforementioned morphotectonic frame and provide a better understanding of the active tectonics of an area, since they yield information on the fault plane orientation, the slip direction and main stress axes orientation (Papazachos, 1961; Delibasis, 1968; McKenzie, 1972, 1978; Ritsema, 1974; Papazachos *et al.*, 1984, 1998; Scordilis *et al.*, 1985; Kiratzi and Langston, 1989; Hatzidimitriou *et al.*, 1991; Taymaz *et al.*, 1990 and Papadimitriou, 1993 among others). Fig. 1.4 shows the existence of thrust faulting along the western coastline of continental Greece, beginning from the north (coasts of Albania) and terminating in the island of Lefkada. This compressional zone is attributed to the collision between the two continental lithospheres, Apulian microplate and Eurasian plate. Thrust faulting is observed along the convex side of the Hellenic arc (Papadimitriou, 1993; Papazachos *et al.*, 1998, among others). These two compressional zones are connected with the Cephalonia Transform Fault (Scordilis *et al.*, 1985). The mainland of Greece is dominated by normal N-S striking faults across the Hellenides mountain chain and Peloponnese, attributed to the orogenic process taking place in the region and the back arc Aegean Sea by normal E-W striking faults, due to the almost N-S extension of the Aegean microplate (McKenzie, 1970).

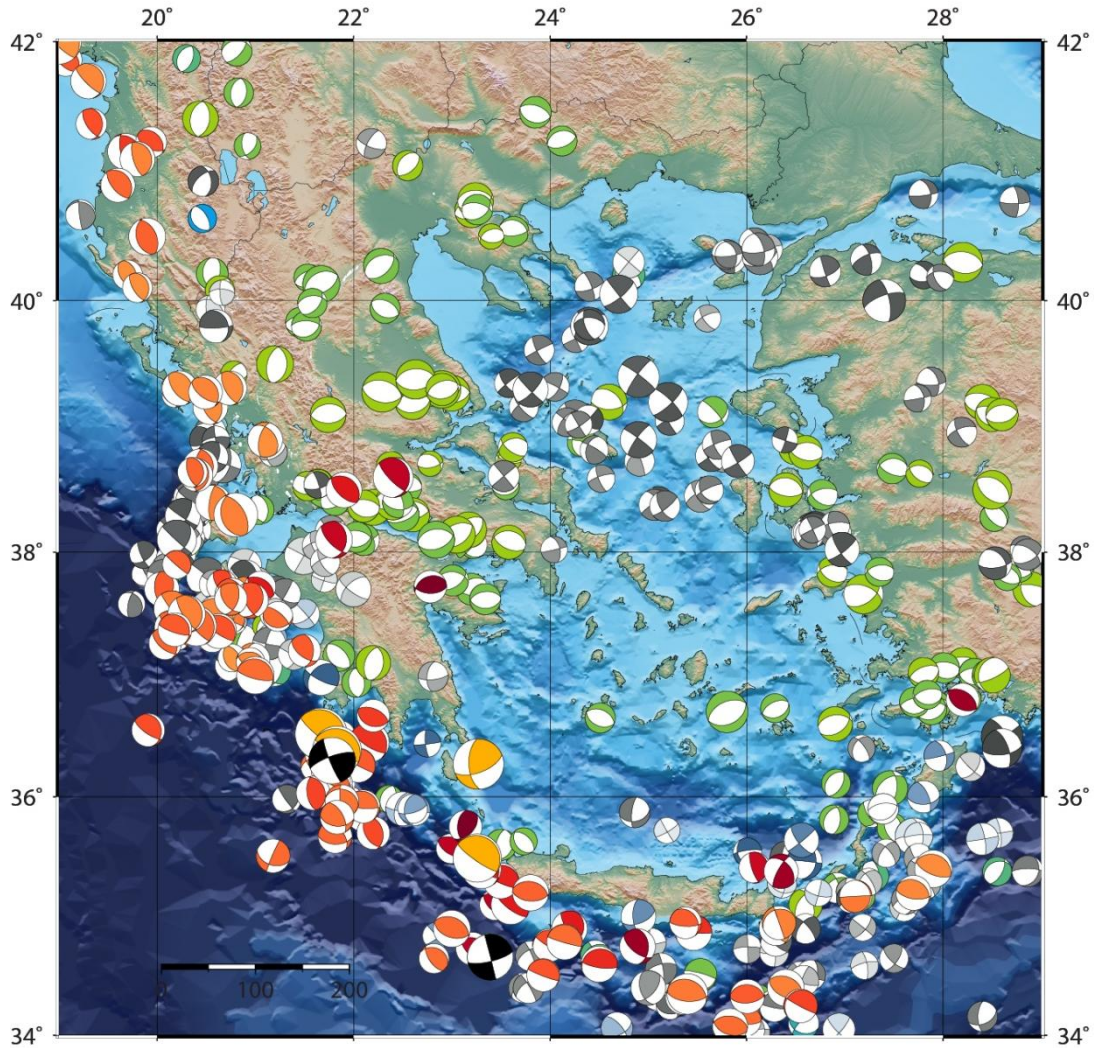


Fig. 1.4 Fault plane solutions of shallow and intermediate depth (up to 100 km) strong ($M > 4.4$) earthquakes for the period between 1953 and 2012 in the broader Aegean area (data were obtained from the Geophysics Department of Aristotle University of Thessaloniki, <http://geophysics.geo.auth.gr>). Green to blue scale denotes normal faulting with increasing focal depth; grey scale denotes strike-slip mechanisms with increasing focal depth; orange to red scale denotes reverse faulting with increasing focal depth. All beach ball diagrams are proportional to the magnitude of the equivalent earthquake, with reverse faults being slightly enlarged in order to highlight the convergent margins. The four yellow and two black beach balls in the western Hellenic arc showing significantly larger depiction represent the earthquakes studied here. The compressional regime due to convergence and subduction is recognized across the outer Hellenic arc.

The earthquakes studied here occurred in the western part of the Hellenic Trench where reverse low-angle thrust faulting has been determined (Papazachos and Delibasis, 1969; McKenzie, 1972; Taymaz *et al.*, 1990; Papazachos *et al.*, 1991; Papadimitriou, 1993; Kiratzi and Louvari, 2003; Benetatos *et al.*, 2004 *etc.*), attributed to the convergence between the African and the Eurasian plates, and especially to the overriding of the Aegean microplate on the oceanic Mediterranean plate (Papazachos and Comninakis, 1971; McKenzie, 1972; Papazachos *et al.*, 1998).

1.6 Previous studies in the area

The use of P-wave polarities data and bodywave inversion is common practice for the focal mechanism determination worldwide. Kikuchi et al. (1993) investigated the complexity of the 1988 Armenia earthquake using teleseismic bodywave inversion, while focal mechanisms of deep earthquakes in southern Spain have been determined using polarities data (Hatzfeld and Frogneux, 1978; Grimison and Cheng, 1986; Buforn *et al.*, 1988, 1991; Morales *et al.*, 1999), and bodywave modelling (Buforn *et al.*, 1997). Lay *et al.* (2013) studied the largest under-thrusting earthquake (February, 2013, $M_w=8.0$) that has been instrumentally recorded in the region of the Santa Cruz Islands, using far-field bodywave seismograms.

Important insights on the active tectonic of the broader Aegean area have come up from studying the focal mechanisms of strong earthquakes. In Greece, the first fault plane solutions were determined using the first P-wave arrivals as they were recorded in large distances (Hodgson and Cock, 1956; Papazachos, 1961; Delibasis, 1968; Papazachos and Delibasis, 1969; Ritsema, 1974; McKenzie, 1972, 1978), P-wave polarities of regional earthquakes (Hatzfeld *et al.*, 1989; Hatzidimitriou et al., 1991, etc.) as well as bodywave modeling (Soufleris and Stewart, 1981, Anderson and Jackson, 1987, Papadimitriou P., 1988; Papadimitriou E., 1993; Kiratzi and Langston, 1989, 1991; Ioannidou, 1989, Taymaz *et al.*, 1990, 1991, Kiratzi *et al.*, 1987, 1991; Benetatos *et al.*, 2004; Roumelioti *et al.*, 2009 among others).

Very important features of the Aegean area were found, such as the tensional stress regime across the western Hellenides mountain chain (Papazachos *et al.*, 1984, among others) and in the northern part of the Aegean lithosphere (McKenzie, 1970). Recognition of the reverse fault zone across the convex part of the Hellenic arc (Papazachos and Delibasis, 1969), of Cephalonia (Scordilis *et al.*, 1985) and Rhodes (Παπαζάχος και συνεργάτες, 2001) transform faults and the left-lateral fault of Skyros (Karakostas *et al.*, 2003) were also attributed to the aforementioned methods.

Empirical relations between seismic moment, different magnitudes and fault dimensions were determined by Kiratzi et al. (1985), using shallow, moderate to strong events in the Aegean. Fault length, width and average displacement were calculated from the moment magnitude of shallow earthquakes in Greece by Papazachos (1989). Scaling laws in this region were also available from Main and Burton (1990), Ambraseys and Bommer (1990), Papazachos and Kiratzi (1992) and Kiratzi and Papazachos (1995). These laws are in agreement with relations that convert other magnitudes to moment magnitude, M_w^* , for different types of seismographs (Papazachos et al., 1997, 2001b, 2002; Margaris and Papazachos,

1999). Finally, Papazachos et al. (2004) derived empirical relations between fault dimensions and moment magnitudes for different types of faults.

CHAPTER 2: THEORETICAL BACKGROUND

2.1 Focal mechanism

In this chapter, the parameters for the fault geometry description are given along with the methods (P-wave polarities, bodywave inversion and spectral analysis) employed to study them. Some of these parameters described are the radiation pattern, the source time function and the equivalent body forces.

2.1.1 Fault geometry

Earthquakes are caused by rapid displacement of a fracture in the crust, under the action of tectonic forces (Udías, 1999). During this rapid displacement the accumulated strain is released in the form of energy (mechanical, elastic, heat, etc.). In order to illustrate the rupture process, the parameters that describe the motion of a shear fracture or a fault plane are used, with the fault plane being a flat plane embedded in the Earth's crust along which slip occurs during an earthquake,. These are the azimuth, ϕ_1 , which is defined as the angle between the trace of the fault (intersection of the fault plane with the horizontal) and the geographical North ($0^\circ \leq \phi_1 \leq 360^\circ$) and is measured so that the fault plane dips to the right-hand side; the dip, δ , which is the angle between the fault plane and the horizontal at a right angle to the trace ($0^\circ \leq \delta \leq 90^\circ$) and the slip or rake, λ , which takes values between 0° and 360° (or $-\pi \leq \lambda \leq \pi$, Aki and Richards, 1980) and is the angle between the direction of the relative displacement or slip and the horizontal measured on the fault plane (Fig. 2.1).

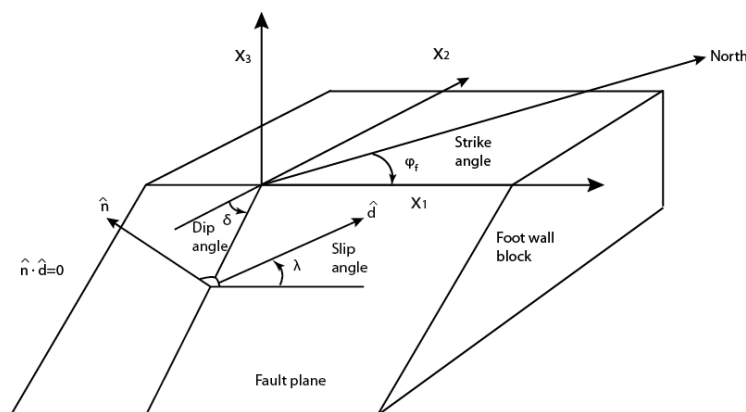


Fig. 2.1 Parameters of the motion on a fault. \hat{n} is the unit vector normal to the surface that separates the footwall from the upper hanging wall (not shown), \hat{d} is the slip vector that describes the motion of the hanging wall with respect to the footwall. The coordinate axes are x_1 , x_2 and x_3 , where x_3 is the vertical, x_1 is oriented along the fault in the plane of the Earth's surface, such that the fault dip angle, δ , measured from the $-x_2$ axis is less than 90° . The slip angle, λ , is measured between the x_1 axis and the \hat{d} in the fault plane. ϕ_1 is the strike of the fault measured clockwise from north (adapted from Stein and Wysession, 2003).

The different types of faulting arise from the different values of λ . Therefore, for $\lambda=90^\circ$ ($\lambda=\pi/2$) pure thrust or reverse faults are observed (depending on the dip angle¹), for $\lambda=-90^\circ$ ($\lambda=-\pi/2$) pure normal faults, for $\lambda=0^\circ$ and $\lambda=180^\circ$ ($\lambda=\pm\pi$) pure strike-slip faults and for intermediate values, dip-slip (normal or reverse) or strike-slip faults with strike-slip and dip-slip component, respectively (Fig. 2.2).

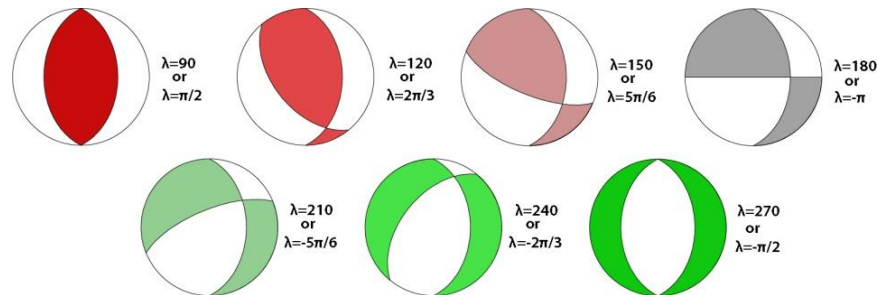


Fig. 2.2 Fault mechanisms as lower hemisphere equal area projections for earthquakes with the same N-S striking fault plane ($\delta=0^\circ$), but with slip angles varying from pure thrust ($\lambda=0^\circ$), to pure strike-slip ($\lambda=180^\circ$), to pure normal (270°) faulting (Adapted from Stein and Wysession, 2003).

The displacement or slip, Δu , is defined as the distance traveled in the relative motion of a point on one side of the fault with respect to that on the other side. If Δu varies along the fault plane, its mean value is $\Delta \bar{u}$. Another important parameter is the area of the fault, noted as Σ . Since real faults have finite dimensions and complicated geometries, they are usually treated as rectangular. Therefore, the fault area, Σ , can be described by the length, L , and width, w , of a fault. The orientation of the fault can be described by three angles, ϕ , δ and λ , whereas its dimensions are given by its area Σ ($\Sigma=L*w$).

All the above parameters are seeking for solving the problem of source mechanism, i.e. they relate observed seismic waves to focal parameters in order to describe the source signal produced by the rupture, also called the source time function (see Chapter 2.3). The direct problem of the source time function consists in determining theoretical seismograms from source models. On the other hand, in the inverse problem, the aforementioned parameters are deduced from the observed seismograms. In both cases, the first step is to determine the seismic source in terms of a mechanical model that represents the physical fracture (Madariaga, 1983; Udías, 1991; Koyama, 1997).

There are two different ways to approach rupture, the kinematic and the dynamic model (Udías, 1999). The first type considers the slip of the fault without relating it to the causative stresses. Rupture is, therefore, described fully in terms of the slip vector as a function of the coordinates on the fault plane and time. From this kind of model, determining the corresponding elastic displacement field is relatively

¹ Thrust faults by definition are reverse faults that dip with low angles (usually up to 40-45°).

easy. Dynamic models, on the other hand, consider the complete fracture as a process that relates the fault slip to the stress acting on the focal region. Describing rupture from the properties of the material of the focal region and the stress conditions is the objective of a complete dynamic description. Dynamic models present greater difficulties and their solutions can be, in many cases, found only by numerical methods. In this study, only kinematic point source models will be used for the determination of the focal mechanism of the earthquake studied.

When an earthquake is produced by rupture of the Earth's crust, a mechanical representation of its source in terms of fractures or dislocations in an elastic medium can be achieved (Udías, 1999). A dislocation constitutes an internal surface inside an elastic medium across which there is a discontinuity of displacement or strain. In this case, only displacement dislocations are considered. The focal region consists of an internal surface, Σ , with two sides (positive and negative, Fig. 2.3). This surface can be considered to be derived from the focal volume V_0 that is flattened to form a surface with both sides together without any volume. The coordinates on this surface are ξ_i and the normal at the points are $n_i(\xi_k)$. If there are no body forces ($\mathbf{F}=0$), the stresses are continuous through Σ and the conditions on the external surface Σ are homogeneous. Then, equation (1) gives the displacement \mathbf{u} in the region of the station (x_s).

$$u_n(x_s, t) = \int_{-\infty}^{+\infty} d\tau \int_{\Sigma} \Delta u_i(\xi_S, \tau) C_{ijkl} n_j(\xi_S) G_{nk,l}(\xi_S, \tau; x_s, t) dS \quad (2.1)$$

where ξ_s and τ are the spatial-time coordinates of the focal region and x_s and t the coordinates of the observation point; n_j is the j component of the normal unit vector on the surface Σ , which is the surface in the focal region; $G_{nk,l}$ represents the derivative of the Green's function with respect to the spatial coordinate ξ_i (Fig. 2.3). Consequently, the seismic source is represented by a dislocation or discontinuity in displacement given by the slip vector $\Delta \mathbf{u}$ on the surface Σ , which corresponds to the relative displacement of the two sides of the fault (Udías, 1999).

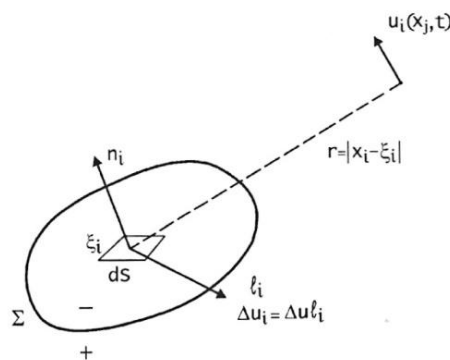


Fig. 2.3 A dislocation Δu on a surface Σ and elastic displacement $u(x,t)$ at a distance r in an infinite medium (Udías, 1999).

2.2 Equivalent body forces

The source can be represented by a system of body forces acting at a point, called the equivalent body forces. It is important to note that the equivalent forces are only a simple model of representing the complex faulting process (Stein and Wysession, 2003). Several systems of forces have been proposed to represent the source of an earthquake, such as a single force, a single couple and a double couple (Fig. 2.4).

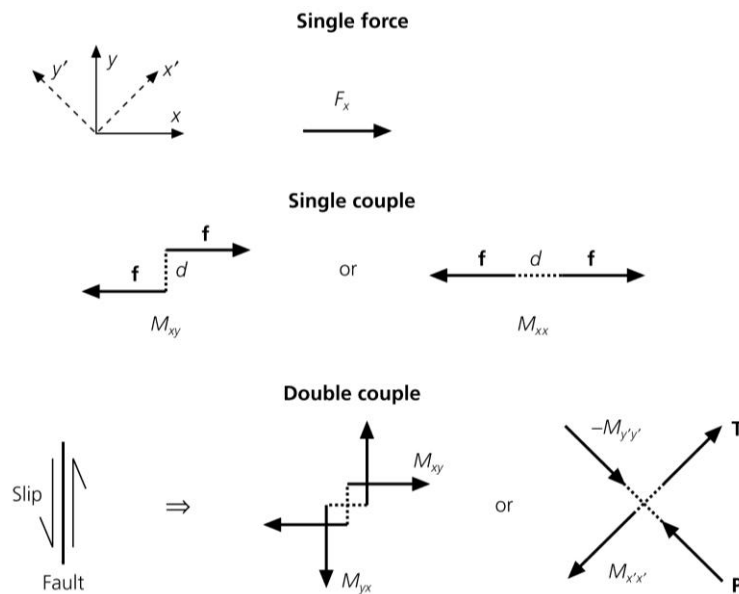


Fig. 2.4 Equivalent body force descriptions of a single force, a single couple and a double couple. The force couple can take two forms. One shown for M_{xy} , has two forces f offset by distance d such that a torque is exerted. The other, shown for M_{xx} , is a force dipole which exerts no torque. Slip on a fault can be described by the superposition of either couples like M_{xy} and M_{yx} or dipoles like $M_{x'x'}$ and $M_{y'y'}$ (Stein and Wysession, 2003).

The last system represents two couples of forces perpendicular to each other, equivalent to two linear dipoles of forces (Fig. 2.5). They correspond to pressure, P, and tension, T, forces acting 45° to the couples and are commonly used in earthquake modeling (Udías, 1999; Stein and Wysession, 2003). For three components of force and three possible arm directions, there are nine generalized couples (Fig. 2.6). Thus the equivalent surface force corresponding to an infinitesimal surface element $d\Sigma(\xi)$ can be represented as a combinations of nine couples (Udías, 1999; Aki and Richards, 2002).

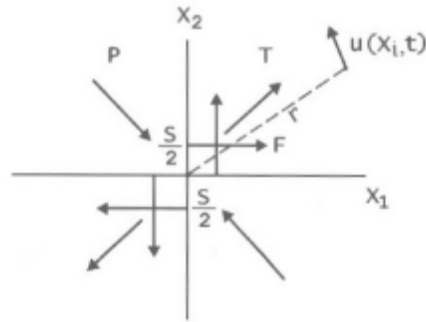


Fig. 2.5 A double couple of forces without a moment acting at the origin and the displacement $u(x,t)$ at a distance r . An equivalent system of two linear dipoles of pressure and tension forces P and T is shown (Udías, 1999).

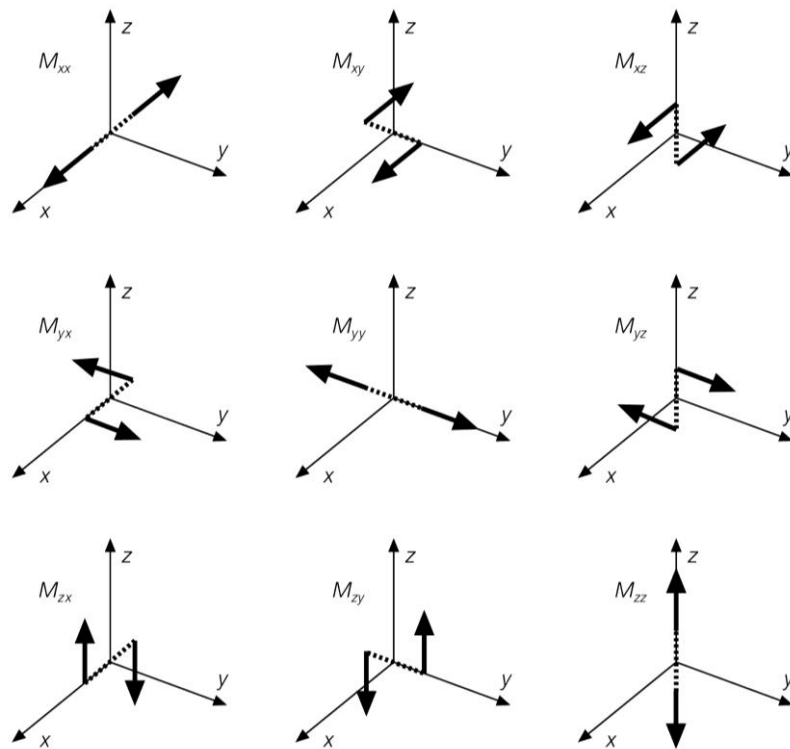


Fig. 2.6 The nine force couples which are the components of the seismic moment tensor. Each consists of two opposite forces separated by a distance d (dashed line), so the net force is always zero (Stein and Wyssession).

Because the equivalent body forces are a double couple, they would be the same if the slip were left-lateral on the y - z plane or right-lateral on a fault in the x - z plane. Thus, seismic waves from a point double-couple source are the same regardless of which plane the fault plane and which the perpendicular auxiliary plane is (Stein and Wyssession, 2003). The magnitude of the equivalent body forces is the scalar moment, M_0 , of an earthquake, measured in $\text{dyn}\cdot\text{cm}$ or $\text{N}\cdot\text{m}$.

2.2.1 Radiation pattern

If in equation (2.1) we assume a point source model and a semi finite medium for the focal plane, then the equation can be written for the P- and the S-waves, respectively, as:

$$u_j^P = \frac{1}{4\pi\rho\alpha^3r} M_0(n_k l_i + n_i l_k) \gamma_j \gamma_i \gamma_k f(t - \frac{r}{\alpha}) \quad (2.2)$$

$$u_j^S = \frac{M_0}{4\pi\rho\beta^3r} (n_k l_i + n_i l_k) (\delta_{ij} - \gamma_i \gamma_j) \gamma_k f(t - \frac{r}{\beta}) \quad (2.3)$$

where $M_0 = \mu\Delta uS$, δ_{ij} is the delta function and $\gamma_i = \partial r / \partial x_i$ etc. The terms $(n_k l_i + n_i l_k) \gamma_j \gamma_i \gamma_k$ and $(n_k l_i + n_i l_k) (\delta_{ij} - \gamma_i \gamma_j) \gamma_k$ represent the radiation pattern and $f(t - r/\alpha)$ and $f(t - r/\beta)$ are the source time functions for the P- and the S-waves, respectively. The indexes i, j, k are the unit vectors across the x_1, x_2 and x_3 axes, respectively.

Therefore, for a step source time function (see Chapter 2.3), elastic displacements in the far field for P- and S-waves are impulses that arrive at a distance r at times $t = r/\alpha$ and $t = r/\beta$, respectively (Udías, 1999).

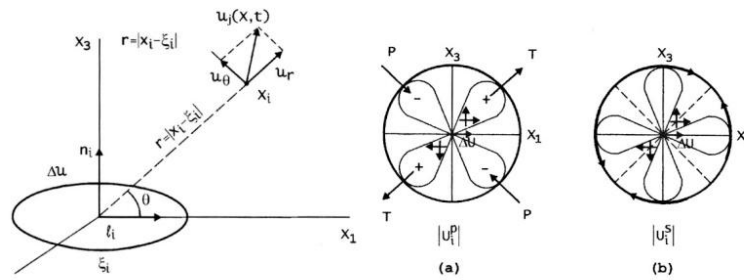


Fig. 2.7 Displacement $u(x,t)$ at a distance r due to a shear dislocation with slip in the x_1 direction on a plane normal to the x_3 axis and the equivalent radiation pattern in the plane (x_1, x_3) , double couple and P and T axes. (a) for P-waves, (b) for S-waves (Udías, 1999).

If we consider the radiation field in spherical coordinates, the displacement due to compressional (P) waves is

$$u_r = \frac{1}{4\pi\rho\alpha^3r} \dot{M}(t - r/\alpha) \sin 2\theta \cos \varphi \quad (2.4)$$

The terms are relevant to Equations (2.2) and (2.3). The first is an amplitude term with decay $1/r$ as for an infinite medium. The second reflects the pulse generated from the fault, which propagates with the P-wave velocity, α , and arrives at distance r in time $t = r/\alpha$ and $\dot{M}(t)$ is called the source time function (see Chapter 2.3). The third part, $\sin 2\theta \cos \varphi$, describes the P-wave radiation pattern and consists in the spatial distribution of amplitudes around the source. It is four-lobed (Fig. 2.8), with each lobe having alternating directions of motion, outward or positive (compression) and inward or negative (dilation) (Udías, 1999). There are two

nodal planes (x_1, x_2) and (x_2, x_3), the first corresponding to the fault plane and the second to the normal to this and to the direction of $\Delta \mathbf{u}$, called the auxiliary plane. Onto these two planes the displacement is zero; they are called the nodal planes. Thus, the fault and auxiliary planes are nodal planes separating compressional and dilatational quadrants. The maximum amplitudes are between the nodal planes, at 45° and coincide with the directions of \mathbf{l} (0,1,0) and \mathbf{n} (0,0,1) (Udías, 1999). In both cases, the radiation pattern is symmetric and we can interchange \mathbf{n} and \mathbf{l} without changing the result. This is the reason why with the radiation pattern it is not possible to distinguish between the fault plane and the auxiliary plane.

Similarly, the S-wave displacement has two components, $u_\theta \hat{\mathbf{e}}_\theta + u_\phi \hat{\mathbf{e}}_\phi$, where

$$u_\theta = \frac{1}{4\pi\rho\beta^3r} \dot{M}(t - r/\beta) \cos 2\theta \cos \varphi \quad (2.5)$$

$$u_\phi = \frac{1}{4\pi\rho\beta^3r} \dot{M}(t - r/\beta) (-\cos \theta \sin \varphi) \quad (2.6)$$

As shown in Fig. 2.8, the S-wave radiation pattern does not have nodal planes, but it describes a vector displacement perpendicular to the P-wave nodal planes and is zero in the null axis. It converges toward the center of the compressional quadrants, i.e. the location of the T axis. It also diverges from the centers of the dilatation quadrants, i.e. the P axis. The S-wave radiation pattern does not reflect so clearly the fault plane, but can be used to study the fault geometry. An interesting feature of equations (2.4), (2.5) and (2.6) is that they show why S-wave amplitudes on seismograms are usually bigger than those of P-waves: the equations predict an average ratio of α^3/β^3 , or about 5.

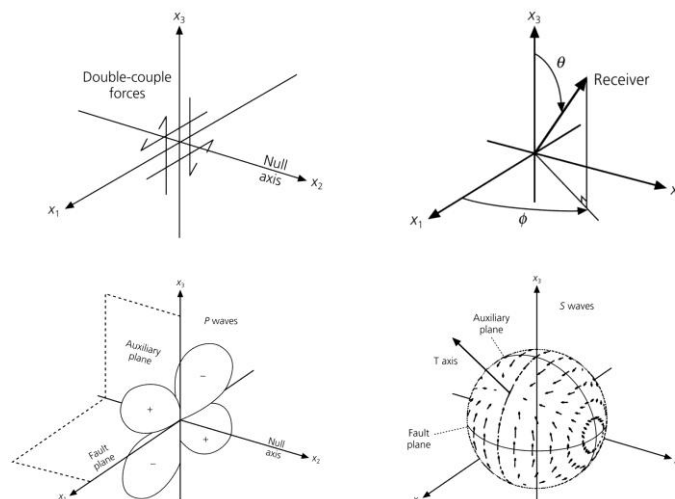


Fig. 2.8 A fault oriented coordinate system for describing the radiation pattern of an earthquake. The body wave radiation pattern for a double couple source has symmetry in the spherical coordinate system shown, corresponding to three axes shown in the top left Fig.. θ is measured from the x_3 axis, the normal to the fault (x_1-x_2) plane and ϕ is measured in the fault plane (top right). The P-wave radiation pattern has four lobes that go to zero at the nodal planes, which are the fault and auxiliary (x_2-x_3) planes (bottom left). The S-wave radiation

pattern describes a vector displacement that does not have nodal planes but is perpendicular to the P-wave nodal planes (bottom right). S-wave motion converges toward the T axis, diverges from the P axis and is zero on the null plane (Pearce, 1997, 1980; Stein and Wysession, 2003).

2.2.2 Fault plane solution

The fault geometry can be studied by seismograms recorded at different distances and azimuths. The simplest method is based on the polarity, or first motion of body waves. This method is based on the radiation pattern of the first P-wave arrival between variously distributed seismic stations (Stein and Wysession, 2003). According to the first motions, four quadrants can be defined, two compressional and two dilatational (Fig. 2.9). This division occurs on the nodal planes in the directions of which the first motion changes from compression to dilatation, and therefore the seismograms show small or zero motion.

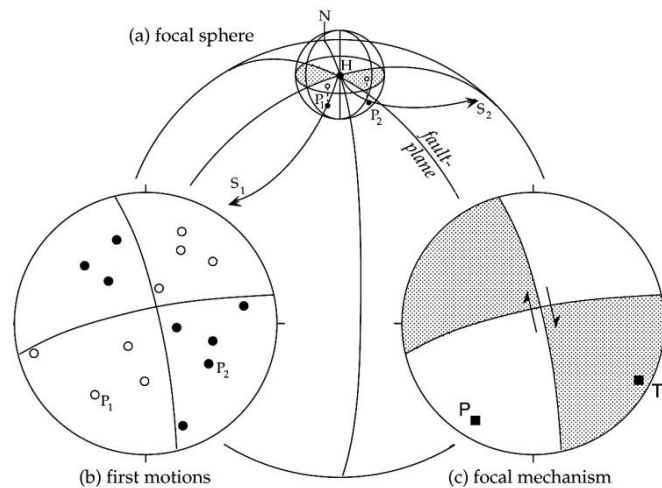


Fig. 2.9 Determination of the focal mechanism of an earthquake using the first P-wave motions. a: focal sphere surrounding the earthquake focus, with two rays S_1 and S_2 that cut the sphere at P_1 and P_2 respectively. b: points P_1 and P_2 are plotted on a lower hemisphere stereogram as first-motion pushes (black circles) or tugs (empty circle). c: the best-fitting great circles define regions of compression (shaded) and tension (empty). The P and T axes are located on the bisectors of the angles between the fault-plane and the auxiliary plane (Lowrie, 2007).

Once the first motion for every different station is represented as a horizontal stereographical projection of the lower hemisphere, the two orthogonal planes need to be separated in four quadrants, representing compressional regions (positive) and dilatational ones (negative). The source orientation is obtained with numerical methods through a least squares adjustment. This orientation is described either with orientation of the two nodal planes (azimuth, dip, and slip) or of the P (maximum compression), T (maximum tension) axes (Lowrie, 2007).

2.3 Source Time Function

The ground motion recorded on a seismogram is considered to be the combination of the earthquake signal, the earth structure through which the waves propagated and the seismometer characteristics. Thus a seismogram can be written

$$u(t) = x(t) * e(t) * q(t) * i(t) \quad (2.7)$$

where $x(t)$ is the source time function, $e(t)$ represents the effect of reflections and conversions of seismic waves at different interfaces along the ray path and the effect of geometrical spreading of the rays due to the velocity structure², $q(t)$ describes the anelastic attenuation, whereby some of the waves' mechanical energy is converted to heat and $i(t)$ describes the instrument response of the seismometer.

The source time function represents the slip dependence on time (Udías, 1999; Stein and Wysession, 2003). The simplest case of a source time function is the step function, which is valid for a short fault that slips instantaneously (Fig. 2.12a). Real faults, though, give rise to more complicated source time functions. This happens because the fault has finite dimensions and therefore the radiated signal is not impulsive (the finiteness effect) and is characterized by the rupture time, T_R . This effect results in lengthening the time function (Fig. 2.10).

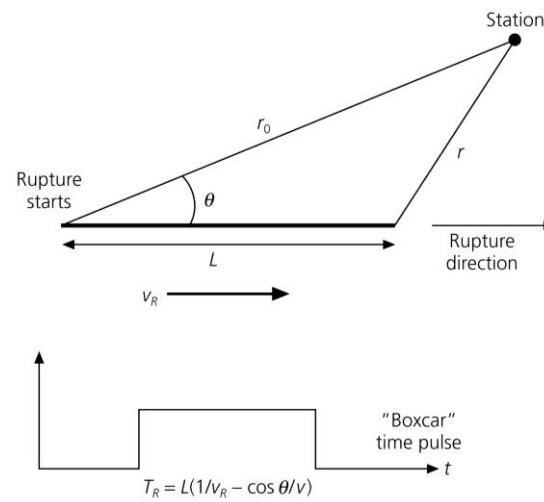


Fig. 2.10 For a fault of length L , the duration of the source time function varies as a function of azimuth, depending on the ratio of the rupture velocity v_R and the wave velocity v .

Another effect that has the same result is the fact that slip does not occur instantaneously. On the contrary, some time is needed, called the rise time, T_D , for the slip to reach its maximum value (rise time effect, Fig. 2.11). In equations (2.2) and (2.3) the source time function is a step function $\Delta u(t) = \Delta u H(t)$, its derivative is the delta function. The radiation patterns don't have any dependence on time; time dependence is contained in the source time function, $f(t - r/\alpha)$ and $f(t - r/\beta)$.

² At distances $30^\circ < \Delta < 90^\circ$ from the source, the effects of upper mantle triplications and core structure ($e(t)$), can be ignored.

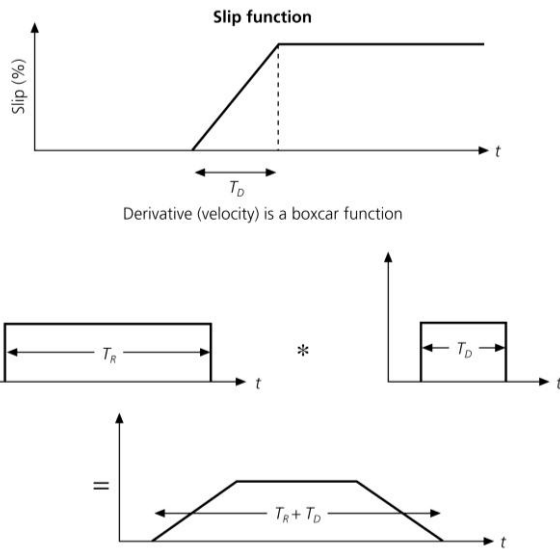


Fig. 2.11 The source time function depends on the derivative of the history of slip on the fault. A ramp time history (top) with duration T_D has a boxcar time derivative. When convolved with the boxcar time function due to rupture propagation (center), a trapezoidal source time function results (bottom).

The simplest models of source time function for a single event are presented in Fig. 2.12. For a more complex event, a combination of triangles and/or trapezoids of different sizes can be used. In this way, a mechanism with several accelerations, decelerations and stops of the rupture process can be represented by a point source (Udías, 1999).

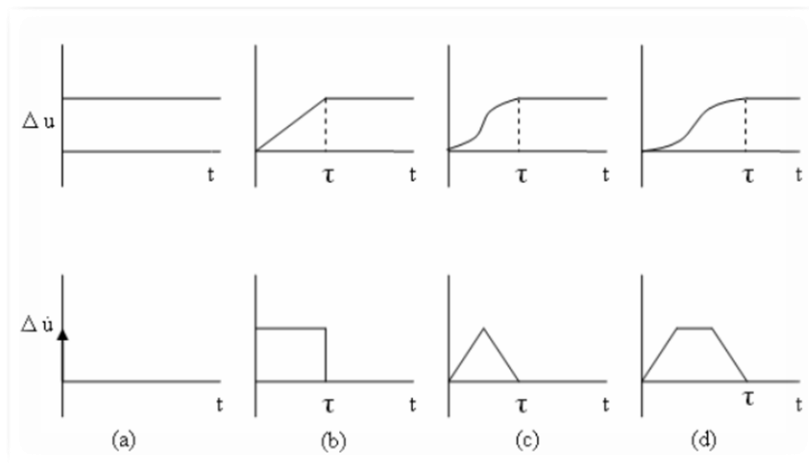


Fig. 2.12 The source time function for a slip velocity, $\Delta \dot{u}(t)$ and its relation to that for a slip $\Delta u(t)$: (a) an impulsive function; (b) a rectangular function with duration τ ; (c) a triangular function of duration τ ; and (d) a trapezoidal function of duration τ (Udías, 1999).

2.4 Seismic moment tensor inversion

2.4.1 Theory

The seismic moment is a quantity that depends on the source strength and fault orientation and characterizes all the information on the source that can be learned from observing waves generated from a source that is considered to be a

point-source (Aki and Richards, 2002). Elastic displacement outside the focal region u_i can be expressed in terms of a unit surface m_{ij} and the corresponding Green function, as already mentioned (Udías, 1999). In the absence of external forces and torques, the sum of all internal forces and moments is null; then by an appropriate choice of the origin of coordinates, $m_{kj}G_{ik,j}=0$ and we obtain

$$u_i = \int_{-\infty}^{\infty} d\tau \int_{V_0} m_{kj} G_{ik,j} dV \quad (2.8)$$

If the moment tensor is defined only on a surface Σ , we use m_{ij} , the moment tensor density per unit surface and write (2.8) as a surface integral

$$u_i = \int_{-\infty}^{\infty} d\tau \int_{\Sigma} m_{kj} G_{ik,j} dS \quad (2.9)$$

These two equations show that elastic displacements outside the focal region can be derived from the seismic moment tensor and the derivatives of the Green's function integrated over the focal region (V_0 or Σ). m_{ij} can represent a very general type of source. It corresponds to any system of internal body forces, provided that the net effect of their sum and the sum of their moments are null. The moment tensor is, thus, a very convenient form in which to represent the source of an earthquake in a general way (Udías, 1999).

For a point source, equations (2.8) and (2.9) can be written as the convolution of the seismic moment tensor with the derivation of Green's function

$$u_k(t) = M_{ij}(t) * G_{ki,j}(t) \quad (2.10)$$

Taking the Fourier transform, in the frequency domain, the relation is the following

$$u(\omega) = M(\omega) \cdot G(\omega) \quad (2.11)$$

For the linear problem, equations (2.10) and (2.11) may be written in matrix form as

$$\mathbf{u} = \mathbf{GM} \quad (2.12)$$

A number of observations larger than the number of unknowns and solutions is obtained by a least squares procedure:

$$\mathbf{M} = (\mathbf{G}^T \mathbf{G})^{-1} \mathbf{G}^T \mathbf{u} \quad (2.13)$$

2.4.2 Application

The seismic moment tensor inversion is widely employed in determining the focal mechanism and the kinematic rupture process of a fault. The inversion study of

the rupture process began in the early 1980s. After several years of development, gradually a variety of the different inversion methods has been formed, e.g. the body wave inversion method (Barker and Langston, 1981, 1983; Kikuchi and Kanamori, 1982, 1983, 1991; Estabrook, 1999; Shomali and Slunga, 2000).

The teleseismic bodywave inversion method of Kikuchi and Kanamori (1982, 1986, 1991, 2003) is widely used to determine the fault plane orientation, focal depth, scalar moment and source time function. It is a numerical, iterative process based on a least squares adjustment of the residuals between the amplitudes of the observed and synthetic seismograms. The basic idea is to compare the two seismograms of P and SH waves at each station, adjusting the parameters until the synthetic seismograms best fit the observed. This evaluation can be done either visually or numerically. For this method, it is common practice to use earthquakes at teleseismic distances for avoiding the upper mantle and core triplications (Barker and Langston, 1981). There are many numerical programs that realize this modeling (Deschamps *et al.*, 1980; Kikuchi and Kanamori, 1982, 1991, 2003; Nábělek, 1984).

Some initial values are needed as input, before generating the synthetic seismograms. These are the parameters of the preliminary fault plane orientation, obtained from the P-wave first motions. For the source time function a triangular or trapezoidal function is used. Since the synthetic waveform changes for different depths of the supposed source, it is yet one more parameter to be found during the inversion. For this, the synthetic seismogram is found for a range of depths taking into account only the P-waves and considering as optimal the depth for which the residual mean square error is the least. Along with the depth, the total duration of the slip is estimated. After that, the SH component is added considering the same source time function. Then the source time function is divided into two or more subevents, in order to obtain more detailed synthetic seismograms that best fit the observed. The final step is to calculate the slip distribution on the seismic fault, using as input the parameters found during the inversion.

2.5 Spectral analysis

The amplitude spectra of body and surface waves are used to obtain certain source parameters such as seismic moment and source dimensions (Hanks and Wyss, 1972). According to Udías (1999) the amplitude spectra of seismic waves depend on the source dimension and not on the model of the source. The seismic moment is determined from the flat part of the spectrum for low frequencies of the waves, after the instrument's response has been deconvolved and all factors that affect wave propagations have been corrected (i.e. radiation pattern, etc., see Chapter 2.2.1).

The far-field displacement due to any reasonable kinematic model of an earthquake is expected to have a spectrum with a constant value at low-frequencies

and proportional to a negative power of frequency at higher frequencies (Aki and Richards, 1980). It is roughly characterized by three parameters: the low-frequency area that can be fitted by a straight line parallel to the frequency axis and is proportional to the scalar moment, the high-frequency area that can be fitted by a line with slope -2 and their intersection that marks the corner frequency f_0 (Brune 1970, 1971; Fig. 2.13). Other source spectral models have also been proposed, that consider two corner frequencies, ω^{-1} and ω^{-2} for lower and higher frequencies that stand for $2/T_R$ and $2/T_D$, T_R being the rupture time and T_D the rise time of the source time function (see Chapter 2.3). A third corner frequency can be added, ω^{-3} , representing the effects of fault width.

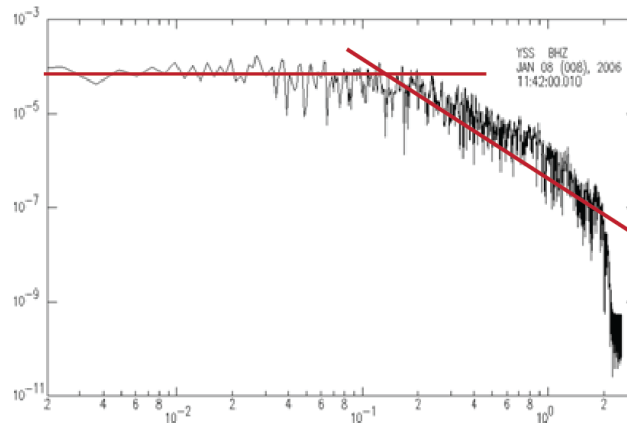


Fig. 2.13 Determination of the seismic moment and the radius of the source from the amplitude spectrum of P-waves.

The scalar moment for P-waves according to Keilis-Borok (1959) is given by:

$$M_0(P) = \frac{\Omega_0(P)}{R_{\theta\varphi}(P)} 4\pi\rho R\alpha^3 \quad (2.14)$$

where $\Omega_0(P)$ is the mean spectral amplitude for low-frequencies for the vertical component of the seismogram, $R_{\theta\varphi}(P)$ is the radiation pattern coefficient, ρ is the density, R is the epicentral distance and α is the P-wave velocity at the source.

There are several models for calculating the source dimensions, both circular and rectangular. In Brune's circular model (1970; 1971, as extended by Hanks and Wyss, 1972), the radius of the fault is given by equation:

$$r(P) = \frac{0.37\alpha}{f_{cp}} \quad (2.15)$$

where α is the P-wave velocity and f_{cp} is the corner frequency of the P-wave spectra. Sato and Hirose (1973) consider a different constant value proportional to the radius also for a circular model:

$$r(P) = \frac{0.24\alpha}{f_{cp}} \quad (2.16)$$

whereas Madariaga's circular model (1976) considers the radius relative to the S-waves velocity:

$$r(P) = \frac{0.32\beta}{f_{cp}} \quad (2.17)$$

β the S-wave velocity. For a rectangular fault, the length, L, and width, w, are given by Eq. (2.18), following Haskell's model (Haskell, 1964):

$$\sqrt{Lw} = \frac{1.7\alpha}{2\pi f_{cp}} \quad (2.18)$$

The scalar moment M_0 determines the zero-frequency level, which rises as the earthquake becomes larger. The relationship between the slip in an earthquake, its fault dimensions and its seismic moment is closely tied to the magnitude of stress released by an earthquake (stress drop). Estimating the average slip from the seismic moment and for a circular fault with a radius r, the stress drop is given by (Keilis-Borok, 1959):

$$\Delta\sigma = \frac{7}{16} \frac{M_0}{r^3} \quad (2.19)$$

and the general displacement, \bar{u} , as calculated from the relation of Aki (1966):

$$M_0 = \mu A \bar{u} \quad (2.20)$$

μ being the shear modulus (equal to $5.0 \cdot 10^{10}$ N/m²) and A the fault surface in km². The moment magnitude was deduced through the scalar moment, given in dyn*cm, according to Hanks and Kanamori (1979):

$$M = \frac{2}{3} \log M_0 - 10.7 \quad (2.21)$$

After obtaining the aforementioned parameters, the average $\langle x \rangle$ values for each one need to be computed, following Archuleta *et al.* (1982):

$$\langle x \rangle = \text{anti log} \left(\frac{1}{N} \sum_{i=1}^N \log x_i \right) \quad (2.22)$$

where N is the number of stations used. This relation is used because in the case of simple average, the mean values are biased towards larger values. The corresponding standard deviation of the logarithm $SD(\log \langle x \rangle)$ and the multiplicative factor, E_x , are also given from the relations of Archuleta (1982):

$$SD(\log \langle x \rangle) = \left[\frac{1}{N-1} \sum_{i=1}^N (\log x_i - \log \langle x \rangle)^2 \right]^{1/2} \quad (2.23)$$

$$E_x = \text{anti log}(SD(\log \langle x \rangle)) \quad (2.24)$$

Generally, many measures of stress drop are reported, i.e. interpretation of bodywave spectra (Brune, 1970), rms value of acceleration from strong motion records (Hanks and McGuire, 1981), but they do not agree with one another, for reasons that are difficult to evaluate. Various estimates usually agree with only a factor of four or five; this is not an error, but an ambiguity in the underlying physics (Scholz, 1990).

CHAPTER 3: FAULT PLANE SOLUTIONS THROUGH TELESEISMIC WAVEFORM MODELLING

3.1 Introduction

This chapter describes the application of the inversion algorithm to the data. Selection of the data was based upon the earthquake magnitude of the events ($M_w \geq 6.0$) and their origin time (after 2000). These criteria assure that every event was recorded by a number of worldwide stations, providing a wealth of good quality data. The western Hellenic Arc was constrained as the study area after the imposition of the conditions, since it was the region with the most events that fitted the criteria.

Fig. 3.1 displays the available fault plane solutions for earthquakes that occurred along the subduction, along with the fault plane solutions accomplished in this study with bodywave inversion. The first one ($M=6.0$) occurred on March 17, 2004 at a depth of 35 km south of the island of Crete, the second one ($M=6.6$) on January 8, 2006 at ~70 km. On February, 2008 three strong events ruptured 30 km off the western Hellenic Trench, south of Peloponnese, the February 14, 2008 $M=6.6$, the February 14, 2008 $M=6.0$ and the February 20, 2008 $M=5.9$ events. The most recent event ($M=6.5$) occurred on October 13, 2013 at a depth of 40 km, east of the Island of Crete.

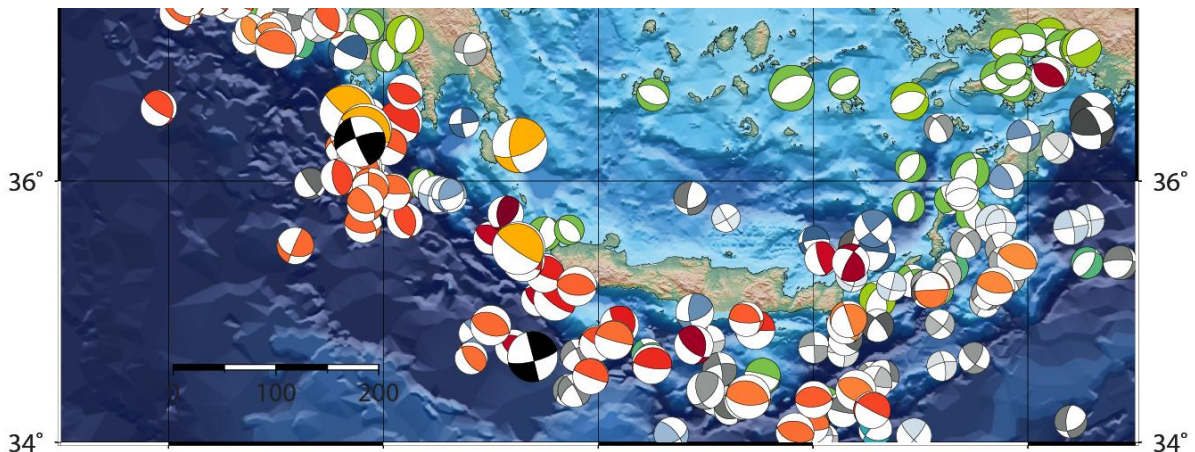


Fig. 3.1 Map of the Hellenic Arc. Therein shown epicenters for $M \geq 4.5$ events (colored circles), focal mechanisms of $M \geq 5.0$ events (fault plane solutions obtained by the Geophysics Department of Aristotle University of Thessaloniki, <http://geophysics.geo.auth.gr>) and focal mechanism of the under study events (bigger black and yellow beach balls). Normal faults are noted with green, reverse faults with light red and strike-slip faults with gray.

For the determination of the fault plane and rupture process parameters, P- and S-waveforms were used, a time window including P, pP, sP and S phases was chosen, a bandpass filter between 0.01 and 1 Hz was applied in most cases, and a rupture velocity of 2.4 to 3.0 km/s was considered. This velocity range was selected,

since the source time function presented the least rms errors and no significant change was observed for each of the aforementioned values.

3.2 March 17, 2004 $M_w=6.0$ Crete earthquake

On March 17, 2004 at 05:20:57 UTC a strong earthquake ($M_w=6.0$) occurred at the southern part of the Hellenic arc south of the Island of Crete in the Libyan Sea (Fig. 3.1) at 34.779°N 23.397°E , with a focal depth of 20 km (<http://geophysics.geo.auth.gr>). The focal mechanism was found to be of strike-slip type, with one nodal plane trending E-W and the other N-S, nearly vertically (Fig. 3.3, gCMT catalog, <http://www.globalcmt.org>).

3.2.1 Focal mechanism determination from P-wave polarities

For the determination of the focal mechanism the P-wave polarities from 35 IRIS stations in epicentral distances between 10° and 90° with adequate azimuthal coverage and the computer program MECSTA (Udías *et al.*, 1984) were used. Fig. 3.2 shows the focal mechanism which evidences strike-slip faulting, with one nearly vertical (86°) nodal plane striking NNW-SSE and one striking ENE-WSW, being of slightly smaller dip angle (74°). Black circles denote stations where the P-wave polarity was recorded upward, giving a compressional quadrant, whereas white circles denote stations where the first P-wave motion was recorded downward, representing the dilatational quadrant. Additionally, the nodal planes orientation, the maximum compression axis, P, and the maximum tension axis, T, were also determined with the same program. The ratio of well to poorly constrained stations ($N=35/37$) is noted by the score 94%. The solution obtained accounts for a right lateral vertical (89°) strike-slip fault striking N-S or a left lateral almost vertical (74°) strike-slip fault trending E-W. However, the distribution of compressional and dilatational quadrants around the source (Fig. 3.2) accounts for left lateral faulting extending N-S and right lateral faulting trending E-W.

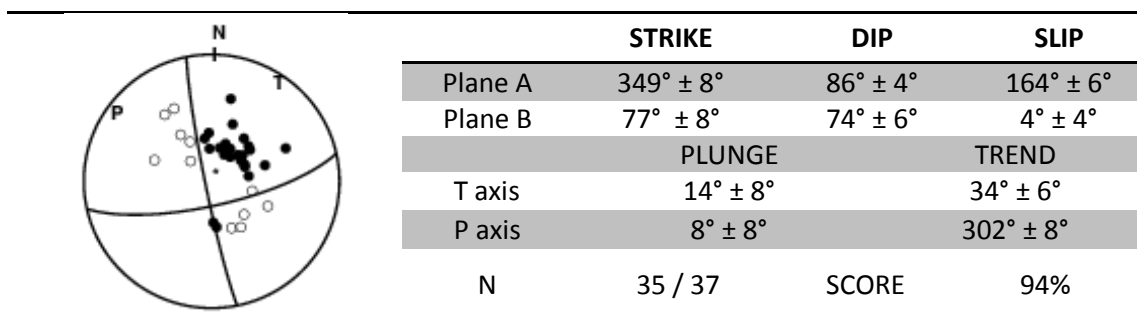


Fig. 3.2 Determination of the fault plane solution as lower hemisphere equal area projection for the March 17, 2004, $M_w=6.0$ Crete earthquake. N: North, T: tensional axis, P: compressional axis; black quadrants represent stations where the first P-wave polarity was recorded as compression, open circles represents stations where the first P-wave polarity was recorded as dilatation.

Fig. 3.3 shows the fault plane solution determined for the same earthquake, obtained by the global Centroid Moment Tensor catalog – gCMT. The values of strike

and dip of both planes are in agreement with the ones obtained by MECSTA. However, the values of rake account for left lateral faulting extending N-S and right lateral faulting trending E-W.

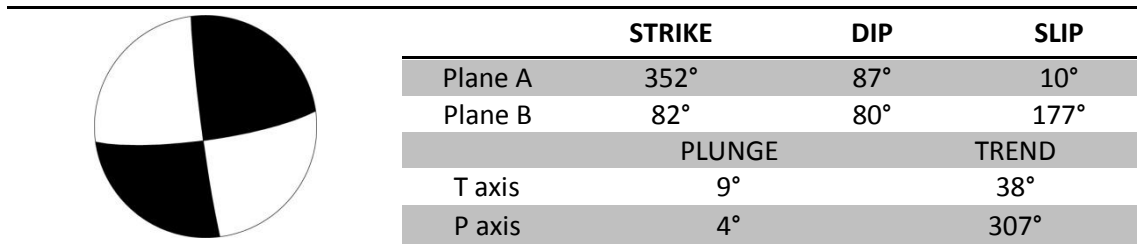


Fig. 3.3 Fault plane solution as lower hemisphere equal area projection for the March 17, 2004, $M_w=6.0$ Crete earthquake, according to the global Centroid Moment catalog (gCMT, www.globalcmt.org). Black quadrants denote areas of compression, empty quadrants denote areas of dilatation.

Additional data are necessary for the determination of the fault plane between the two nodal planes, such as directivity, distribution of aftershocks, geological data etc. For the particular event, though, no additional data were available. Therefore, inversion was carried out for both planes and the one exhibiting the least rms values was considered as the fault plane, which is the E-W striking one (see Chapter 3.2.3).

3.2.2 Depth determination

After the focal mechanism determination from P-wave polarities, the waveform inversion is carried out with the program of Kikuchi and Kanamori (1982, 1991, 1993, 2003). Data from the same stations were used, only with one extra limitation of using stations between 30° and 90° epicentral distance, in order to avoid upper mantle and core triplications (Barker and Langston, 1981). Of the available IRIS stations, only the ones with the highest signal-to-noise ratio were inverted.

For the first step of the inversion, the general algorithm was used, giving one or more discrete sources. Only the P-waves were inverted, in order to determine the form of the source time function, later to be enhanced with the algorithm for the fixed inversion. The important element for this step is to ensure that with this source time function, all the polarities of the synthetic waveforms are clearly in the same sense as the observed ones. In fact, all polarities of the synthetic waveforms match the corresponding observed ones, except for two stations, where the downward polarities of the synthetic waveform are not very clear (Fig. 3.4). These two stations are expected to improve in the following steps. Parameters such as the M_0 , the magnitude and the error are not taken into account in this phase.

Fig. 3.4 shows the results of this preliminary inversion for a triangular source time function, with rise time 2s. Time scale (in s) above the waveforms represents the duration of the waveform to be inverted. In the left column, the figures from top

to bottom represent the source time function and the focal mechanism. On the left of every couple of waveforms, in the first line the peak-to-peak amplitude in microns is given. In the second line the station id is stated (network.station code name.instrument code number³) and in the third line the station's azimuth. The top waveform is the observed whereas the second is the synthetic one.

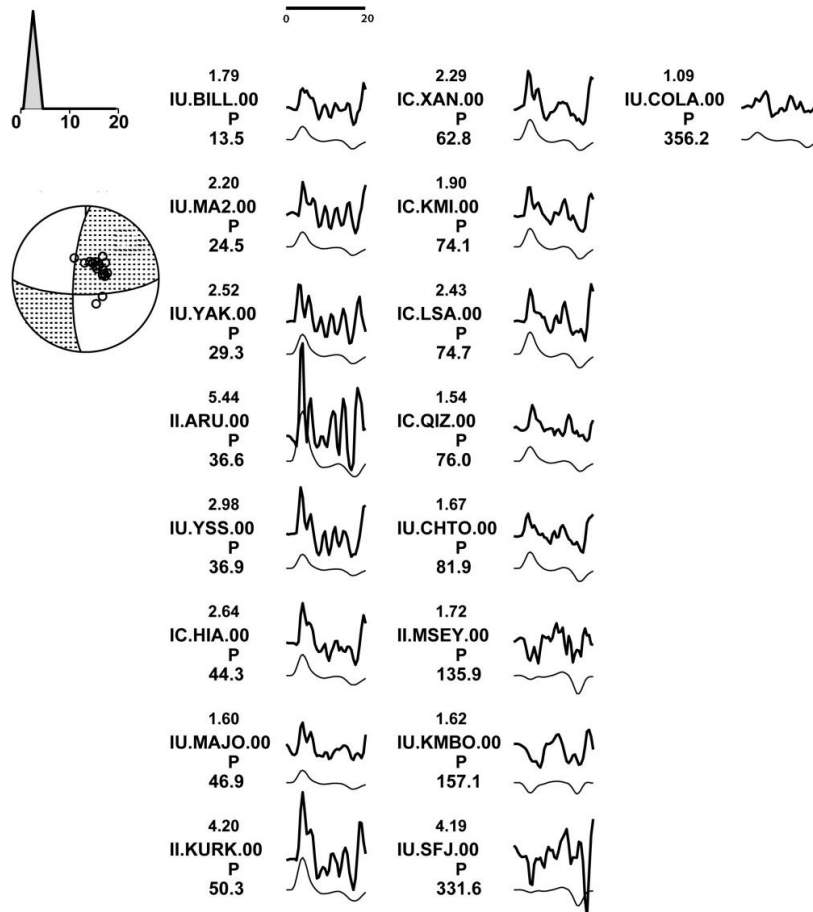


Fig. 3.4 Preliminary inversion results of the March 17, 2004 $M_w=6.0$ Crete earthquake, using only P-waves. Time scale of inversion (in secs) is shown above the waveforms. On the left of every couple of waveforms, in the first line the peak-to-peak amplitude in microns is given. In the second line the station id is stated (network.station code name.instrument code number) and in the third line the station's azimuth. The top waveform is the observed whereas the second is the synthetic one. In the left column, the figures from top to bottom represent the source time function, the inversion reference points and the fault plane solution.

It is of great importance to accurately define the focal depth of the earthquake because the inversion results depend on the depth of the reference point. Proper results are achieved by carrying out a preliminary inversion, using only the P-waveforms, for the same source time function, but for different depths. Depths ranging from 20 km to 45 km with a step of 5 km were considered, since these values lie in the range of depths proposed by several institutions (see Chapter 3.2.4). When the depths with the least rms errors were obtained, inversion was

³ For explanation see Appendix B.

repeated for different depths with a step of 1 km in the range of 20 to 40 km. The results are shown in Fig. 3.5 and Fig. 3.6, respectively. The final depth was determined by selecting the one with the minimum rms error. In this case, the minimum error corresponds to a depth of 33 km (rms=0.6934,) and it is taken as the depth of the reference point.

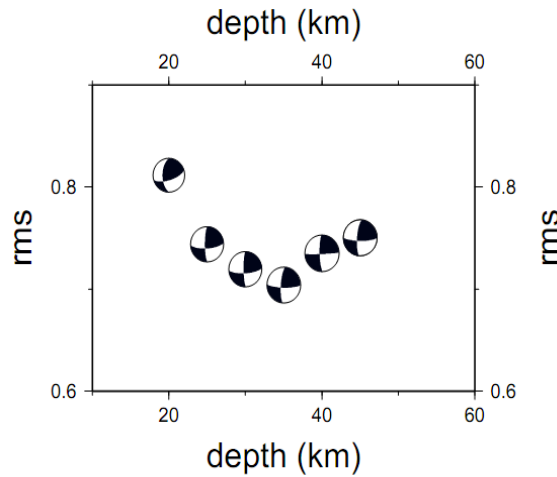


Fig. 3.5 Rms error to depth diagram with a step of 5 km, for March 17, 2004, $M_w=6.0$ Crete earthquake. The source time function is triangular with 4s total duration.

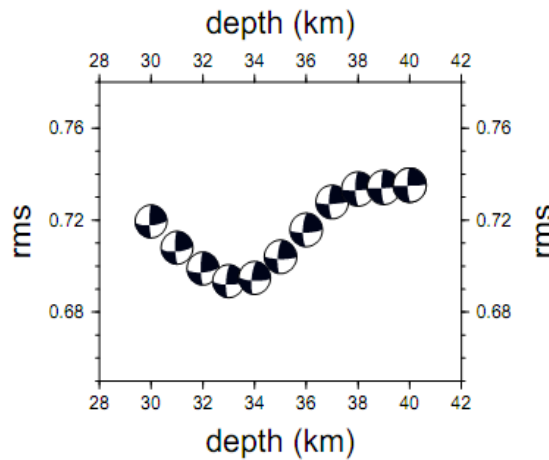


Fig. 3.6 Rms error to depth with a step of 1 km for the March 17, 2004, $M_w=6.0$ Crete earthquake. The notations are the same as in Fig. 3.5

After obtaining the general source time function, the depth and the preliminary focal mechanism, the SH-waves are added, keeping the values for all the aforementioned parameters the same (Fig. 3.7). It is important to point out that during the inversion, the weights for the P stations were 1, whereas for the SH waves were 0.2 due to the greater amplitudes of the SH waves compared to the P waves. The amplitude normalization factor for both data, synthetic and observed, is the same.

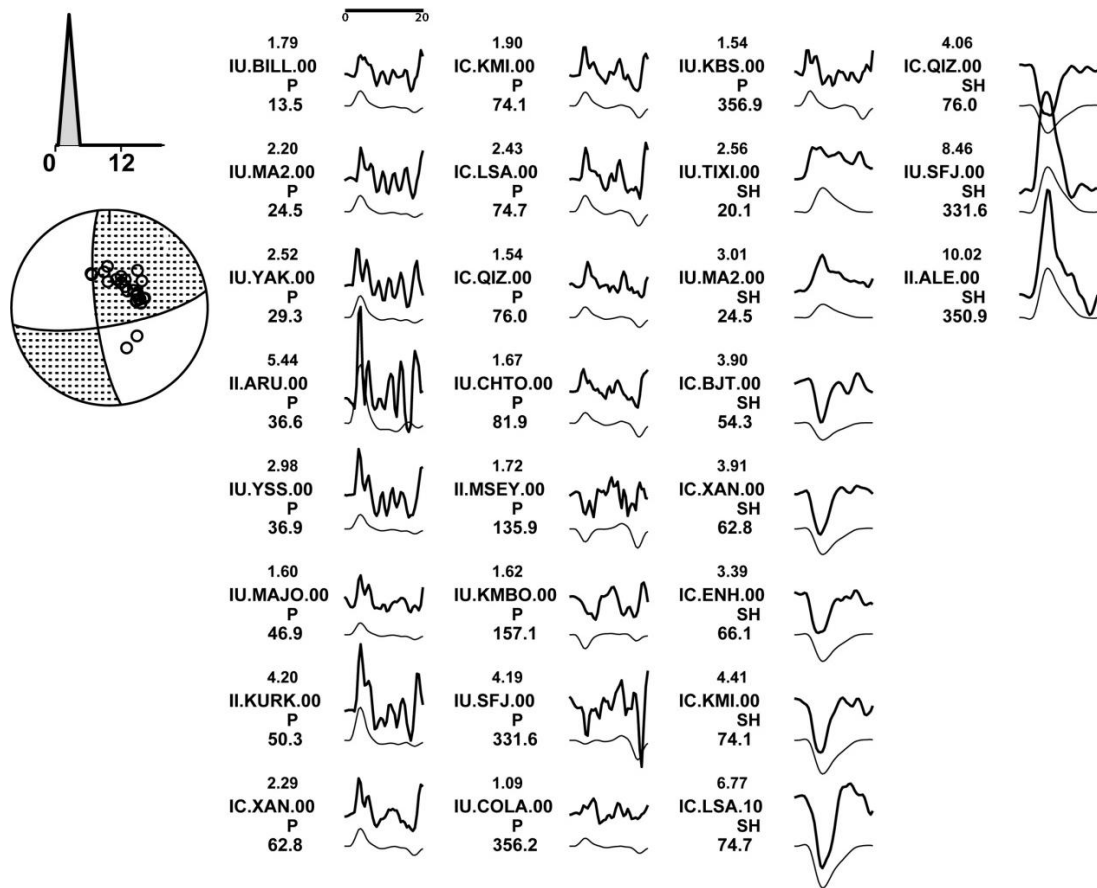


Fig. 3.7 Inversion with P and SH-waves for the March 17, 2004 $M_w=6.0$ Crete earthquake. The notations and symbols are same as Fig. 3.4.

After assuring concordance of the synthetic waveforms polarities with observed SH-waves, the refinement follows. More details are now sought for the source time function. Thus, the simple source time function consisting of one asperity considered above is now improved by dividing it into more asperities, of smaller size and rupture time. The number of asperities is increasing progressively, each time resulting in smaller rms error. In this case, four asperities are considered, as show in Fig. 3.8. The diagram with the dip and the rake accounts for the seismic fault area. The circles are the asperities and the diameter of each one is proportional to its size and hence the rupture duration. This distribution of asperities gives the equivalent source time function, in this case 6s of total rupture duration, with two distinct peaks, each one representing the larger asperities broken during the earthquake.

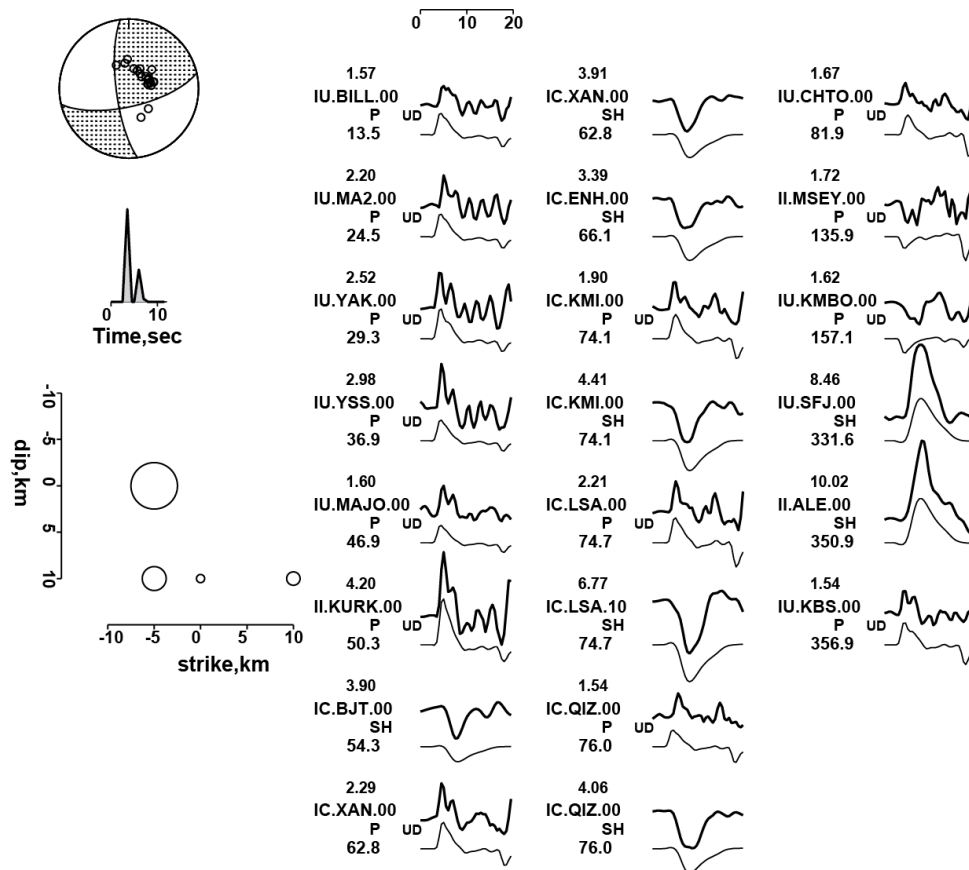


Fig. 3.8 Detailed inversion for the March 17, 2004 $M_w=6.0$ Crete earthquake. The diagram on the bottom left corner represents the seismic fault area and the empty circles the asperities broken during the rupture. The rest of the notations and symbols is the same as in Fig. 3.4.

3.2.3 Constraints on the fault plane

In lack of seismotectonic data for the particular earthquake, inversion was carried out for both nodal planes. The plane that presented the least rms error was considered to be the fault plane (E-W striking). Therefore, constraints were accomplished only for this plane. In order to check whether the fault plane solution was chosen correctly, a set of tests needed to be carried out to the strike, the dip and the rake of the fault plane. They consisted in changing one of these parameters, while keeping the other two constant, in order to better understand how each one affects the final solution.

Several inversions are carried out, with the strike varying from 67° to 97° with a 10° step. It is observed that for all the values of the strike, the polarities of the synthetic waves are in the same sense with those of the observed ones. The only changes noted are in the amplitude of the generated waveforms. For example, while the strike increases, the amplitude of ENH station for the SH-waves and MSEY and KBS stations for the P-waves is decreasing, while that of LSA station is increasing. The best strike solution is determined to be equal to 77° , as it can be seen from the results of the strike tests and the rms error (Fig. 3.9).

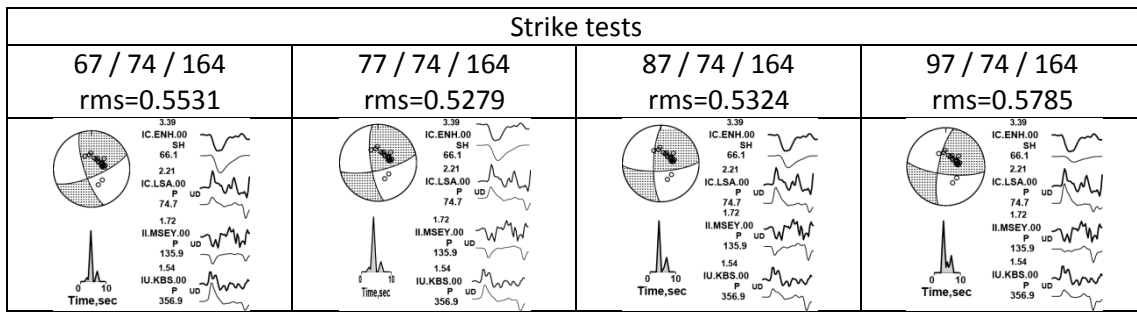


Fig. 3.9 Results of the strike test of the fault plane for the March 17, 2004, $M_w=6.0$ Crete earthquake. Above every fault mechanism, the strike, dip and rake are noted and the corresponding rms error. The notations and symbols of the fault mechanism, the source time function and the waveforms are the same as in Fig. 3.4.

After having determined the strike of the fault plane, tests concerning its dip are carried out, starting from 64° with a step of 5° (Fig. 3.10). A successive increase in the amplitudes of every synthetic waveform and for every station is observed. Since no significant changes are noted in the polarities as well as the periods and amplitudes of the waveforms, the dip value that provide the least rms is considered, that is 69° .

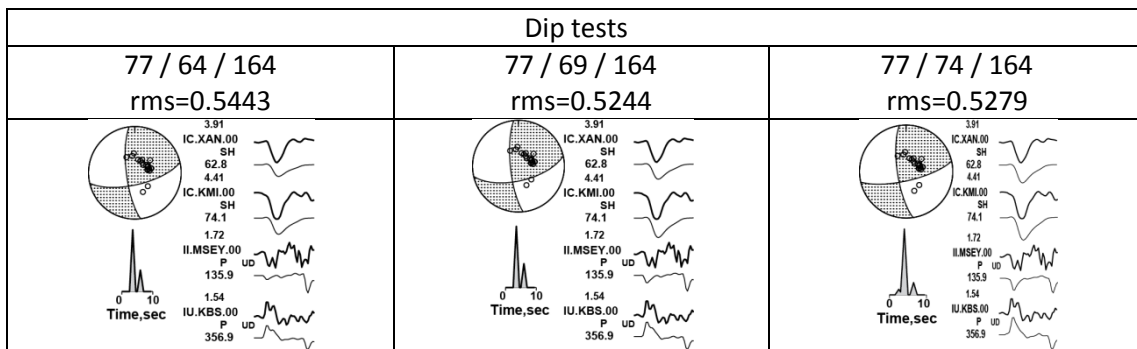


Fig. 3.10 Results of the dip test of the fault plane for the March 17, 2004, $M_w=6.0$ Crete earthquake. The notations and symbols are the same as in Fig. 3.9.

With the strike and dip already constrained, the rake value undergoes testing, starting from 154° and ending at 169° , the step being 5° (Fig. 3.11). The small variance in the rms value is an indication of the small differences between the inversion results. Therefore, the rms is taken into account for the determination of the best fitting rake value ($\lambda=159^\circ$). Summing up, the apt fault plane solution is considered to be $77^\circ/69^\circ/159^\circ$.

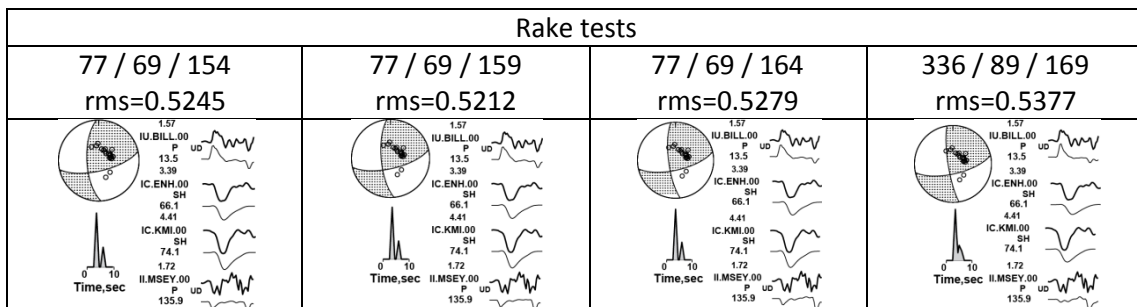


Fig. 3.11 Results of the rake test of the fault plane for the March 17, 2004, $M_w=6.0$ Crete earthquake. The notations and symbols are the same as in Fig. 3.9.

3.2.4 Results

After constraining the optimal fault mechanism, the final inversion is carried out. Fig. 3.12 shows the results of the bodywave inversion. As in most earthquakes, a double couple and a triangular source time function are assumed. The source time function has a rise time equal to 1s and a total duration of 6s, the total duration of the waveform to be inverted is 20 seconds, so as to contain the entire P and SH wave arrival. The focal mechanism corresponds to a right-lateral steep (69°) strike-slip fault, extending nearly E-W, which in lack of other data was assumed according to the best fitting inversion that was carried out for both planes. The magnitude is found equal to $M_w=6.0$ and the scalar moment $M_0=0.107 \cdot 10^{19}$. Table 3.1 lists source parameters provided by different Institutions.

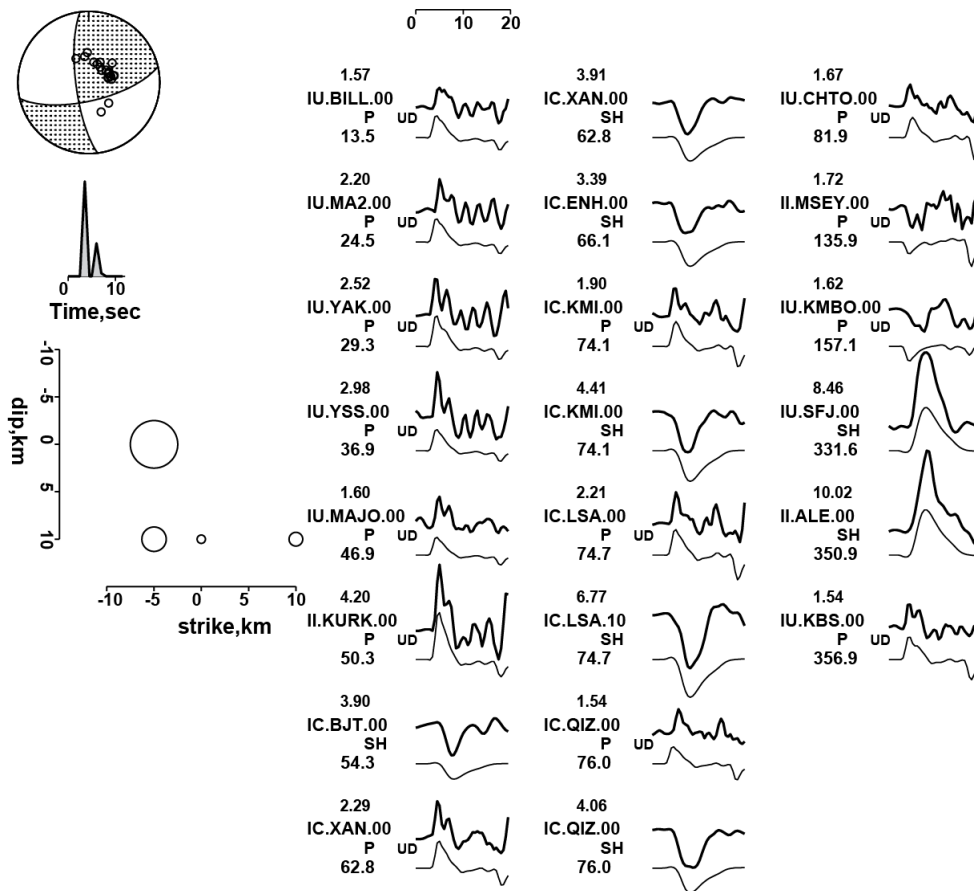


Fig. 3.12 Final inversion for the March 17, 2004 $M_w=6.0$ Crete earthquake. The notations and symbols is the same as in Fig. 3.4.

Table 3.1 Fault plane solutions from different references for the March 17, 2004 $M_w=6.0$ Crete earthquake. Given parameters are the depth in km, the M_w , the orientation of the compressional and tensional axes, the nodal planes orientation, the duration in seconds of the source time function and the scalar moment in Nm. HRV: CMT-Harvard; SED: Swiss Seismological Service at ETH Zürich; USGS: U.S. Geological Service.

| Depth (km) | M_w | P-plunge (°) | P-azimuth (°) | T-plunge (°) | T-azimuth (°) | Strike (°) | Dip (°) | Slip (°) | STF (s) | M_0 (10^{19} Nm) | References |
|------------|-------|--------------|---------------|--------------|---------------|------------|---------|----------|---------|-----------------------|-------------------------|
| 12 | 6.0 | 4 | 307 | 9 | 38 | 82 | 80 | 177 | 5 | 0.110 | HRV |
| 25 | 6.1 | 14 | 307 | 4 | 216 | 82 | 83 | -176 | 9 | - | SED |
| 32 | 6.1 | 5 | 310 | 6 | 40 | 85 | 82 | 180 | - | 0.160 | USGS |
| 35 | 6.0 | - | - | - | - | 169 | 62 | 8 | 6 | 0.170 | Yolsal and Taymaz, 2012 |
| - | - | 8 | 302 | 14 | 34 | 77 | 74 | 4 | - | - | This study - polarities |
| 33 | 6.0 | - | - | - | - | 77 | 69 | 159 | 6 | 0.107 | This study - inversion |

3.3 January 08, 2006 $M_w=6.6$ Kythera earthquake

On January 8, 2006, at 11:34:54 UTC a strong ($M_w=6.6$) earthquake occurred in the submarine area south of Peloponnese causing limited damage on nearby islands of Kythera and Antikythera and in western Crete (Karakostas *et al.*, 2006; Konstantinou *et al.*, 2006; Taymaz *et al.*, 2007c; Nikolintaga *et al.*, 2008, Skarlatoudis *et al.*, 2009). The epicenter was determined at $36.208^\circ\text{N } 23.445^\circ\text{E}$, just 20 km east of the island of Kythera and the depth at 75 km (Nicolintaga *et al.*, 2008). This earthquake was the largest event of the equivalent seismic sequence. The aftershocks, which lasted almost 3 weeks, lie in 55 to 75 km depths, thus defining as the fault plane the ENE-WSW striking plane with an almost vertical dip angle (dip= 75°) (Nicolintaga *et al.*, 2008). This consideration is consistent with the NW-SE compression which follows the local trend of the Hellenic arc and the NE-SW down-dip extension parallel to the dip of the subducting slab (Taymaz *et al.*, 1990; Kiratzi and Papazachos, 1995; Benetatos *et al.*, 2004).

3.3.1 Focal mechanism determination from P-wave polarities

The procedure follows the same steps that have already been extensively mentioned in Chapter 3.2.1. Forty three IRIS stations were used between 10° and 90° epicentral distance, having adequate azimuthal coverage and high signal-to-noise ratio. Fig. 3.13 shows the focal mechanism obtained with MECSTA, which corresponds to two strike-slip faults with significant reverse component, one striking 54° N-S and the other striking steeper (71°) ENE-WSW while the axis of compression being more horizontal (11°) than the tensional one (40°).

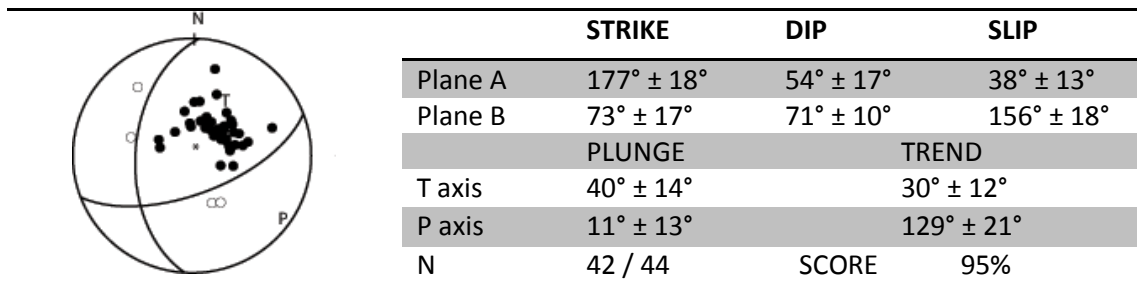


Fig. 3.13 Determination of the fault plane solution as lower hemisphere equal area projection for the January 8, 2006 $M_w=6.6$ Kythera earthquake. Notations and symbols are the same as in Fig. 3.2.

Fig. 3.14 shows the fault plane solution obtained from the gCMT catalog. Most differences are trivial. The greatest changes are observed for the strike of the N-S fault; after gCMT it extends 24° more to the east, striking NNE-SSW. Generally, each plane and axis is steeper according to gCMT ($\pm 16^\circ$ for plane B, $\pm 10^\circ$ for plane A; $\pm 25^\circ$ for the tensional and $\pm 5^\circ$ for the compressional axis). According to the present study, motion on the fault is mostly strike-slip with some dip-slip (reverse), as it is denoted by the value of slip (38° and 156° for plane A and B, respectively). On the contrary, motion is mostly dip-slip (reverse) with some strike-slip, according to the gCMT solution.

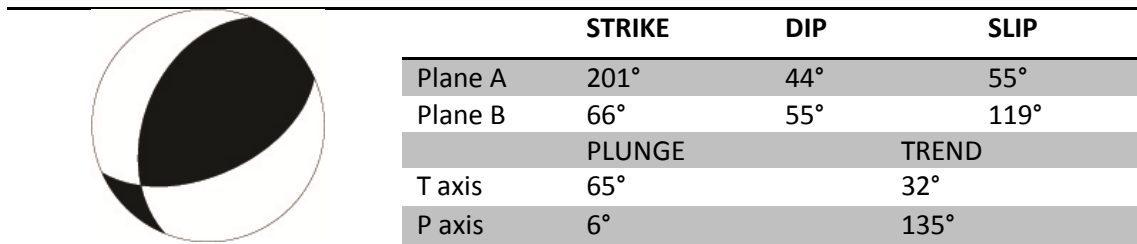


Fig. 3.14 Fault plane solution as lower hemisphere equal area projection for the January 8, 2006 $M_w=6.6$ Kythera earthquake, according to the global Centroid Moment catalog (gCMT, www.globalcmt.org). Black quadrants denote areas of compression; empty quadrants denote areas of dilatation.

3.3.2 Depth determination

For the depth determination only P-waves were considered, with depths varying from 50 km to 90 km, the step being 10 km. The selection of this range was based upon published studies results (Table 3.2). The least rms was observed between 65 and 75 km depth (0.4863-0.4852, Fig. 3.15). Since the rms errors shows no significant differentiation, no further examination is considered necessary, and a depth of 70 km (rms=0.4851) is accepted.

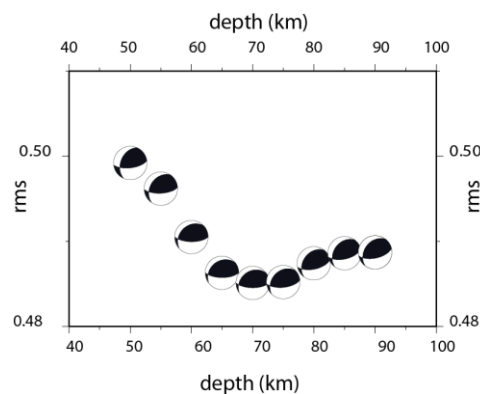


Fig. 3.15 Rms to depth diagram with a step of 10 km for the January 8, 2006 $M_w=6.6$ Kythera earthquake. Symbols are the same as in Fig. 3.5.

3.3.3 Constraints on the fault plane

In order to firstly constrain the strike, inversion is carried out with this parameter varying from 55° to 85° (Fig. 3.16). All source time functions endure 12 seconds. The only significant change observed is for BRVK station, the amplitude of which decreases with the increase of strike, ending in almost zero for the last value (85°). For the first three values of strike, differences are minimal and thus the one with the least rms is chosen (rms=0.4108 for 65°).

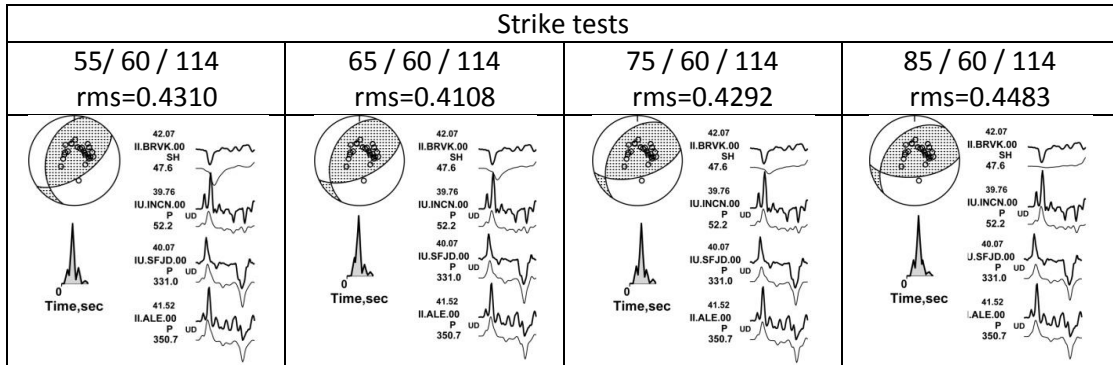


Fig. 3.16 Strike test results of the January 8, 2006 $M_w=6.6$ Kythera earthquake. The notations and symbols are the same as in Fig. 3.11.

The dip was tested taking values from 50° to 80° , changing 10° at a time. The best fitting solution is for 60° . The synthetic waveforms, with the change of dip, range as far as the amplitude is concerned. For example, BRVK and SSE synthetic waveforms show the same polarity in all four tests, but the amplitude increases from lower to steeper angles (Fig. 3.17). The opposite applies for INCN and XAN (i.e. amplitudes decrease for steeper angles).

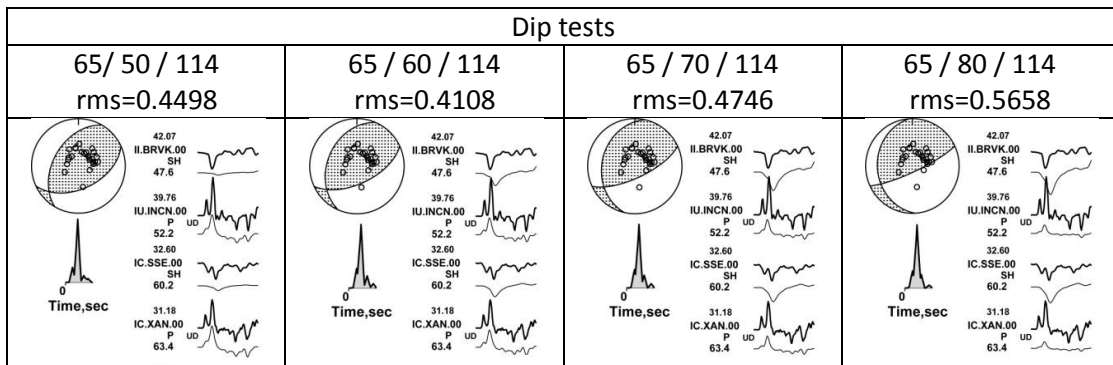


Fig. 3.17 Dip test results of the January 8, 2006 $M_w=6.6$ Kythera earthquake. The notations and symbols are the same as in Fig. 3.11.

The final step for the determination of the fault plane is to fix the rake value. Tests from 94° to 124° were applied (Fig. 3.18). Significant changes are noted only for ALE station, where the amplitude of the synthetic waveform increases with the increase of the rake. The best solution is considered to be that for 114° . Here, only 3 out of the 25 waveforms are shown. The fourth solution seems to best fit the observed data that are presented in the strike tests. However, the rms error which gives a general assessment of the solution accounts for the total fit between observed and synthetic waveforms. Thus, the rake preferred is the one that correspond to the least rms (114° , rms=0.4108).

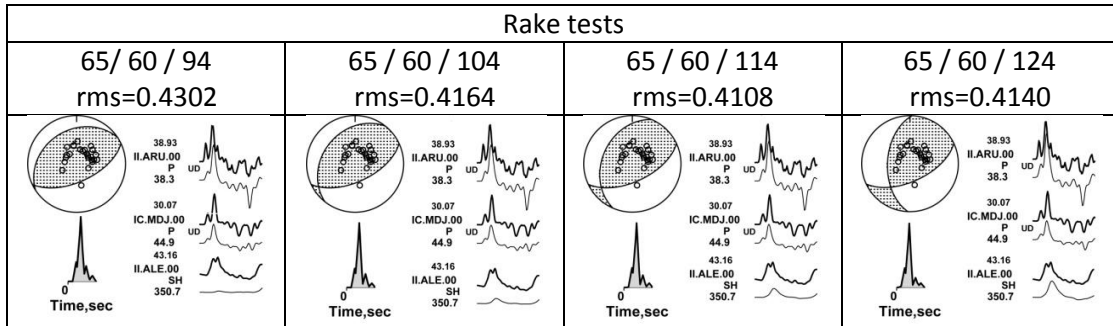


Fig. 3.18 Rake test results of the January 8, 2006 $M_W=6.6$ Kythera earthquake. The notations and symbols are the same as in Fig. 3.11.

3.3.4 Results

Fig. 3.19 shows the results of the bodywave inversion application. As in most earthquakes, a double couple and a triangular source time function are assumed. The duration of the source time function is 12 seconds and the total duration of the waveform to be inverted is 40 seconds, so as to contain the entire P and SH wave arrival. The focal mechanism corresponds to a thrust fault with one nodal plane trending NNE-SSW and the other trending ENE-WSW and being steeper than the first one. Considering the seismotectonic frame of the area (Kiritzi and Papazachos, 1995; Benetatos *et al.*, 2004), the form of the Benioff zone (Papazachos *et al.*, 2000) and the distribution of aftershocks of particular event (Nikolintaga *et al.*, 2008) the fault plane is recognized as the ENE-WSW plane. On this plane, five asperities are considered to have broken, resulting in the source time function presenting one great peak and several more, being particularly smaller. The synthetic waveforms obtained for this source time function agree with the observed ones as far as the polarities are concerned. Also, the waveform details are simulated in most of the stations. The magnitude, $M_W=6.6$, and the scalar moment $M_0=0.868 \cdot 10^{19}$ Nm are determined. Table 3.2 lists source parameters provided by different Institutions.

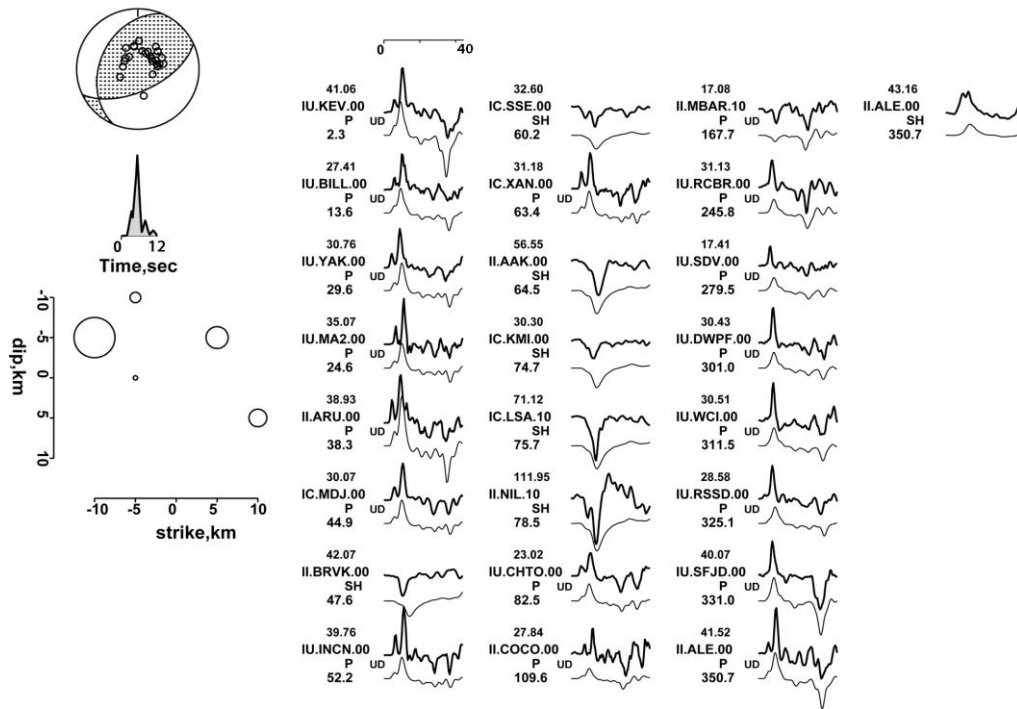


Fig. 3.19 Detailed inversion for the January 8, 2006 $M_w=6.6$ Kythera earthquake. The notations and symbols are the same as in Fig. 3.8.

Table 3.2 Fault plane solutions from different references for the January 8, 2006 $M_w=6.6$ Kythera earthquake. Given parameters are the depth in km, the M_w , the orientation of the compressional and tensional axes, the nodal planes orientation, the duration in seconds of the source time function and the scalar moment in Nm. AUTH: Aristotle University of Thessaloniki; GEOSCOPE: GEOSCOPE Observatory, Paris; HRV:CMT-Harvard; INGV: Istituto Nazionale di Geofisica e Vulcanologia; KAN: Kandilli Observatory and Earthquake Research Institute; NOA: National Observatory of Athens; SED: Swiss Seismological Service at ETH Zürich; USGS: U.S. Geological Service.

| Depth (km) | M_w | P-plunge (°) | P-azimuth (°) | T-plunge (°) | T-azimuth (°) | Strike (°) | Dip (°) | Slip (°) | STF (s) | Mo ($\times 10^{19}$ Nm) | References |
|------------|------------------|--------------|---------------|--------------|---------------|------------|---------|----------|---------|---------------------------|-----------------------------------|
| 64 | 6.6 | - | - | - | - | 76 | 63 | 160 | 15 | - | Agalos, 2009 |
| - | - | - | - | - | - | 71 | 52 | 120 | - | - | AUTH |
| - | - | 9 | 126 | 15 | 65 | 55 | 58 | 117 | - | - | GEOSCOPE |
| 64 | 6.7 | 6 | 135 | 65 | 32 | 66 | 55 | 119 | 11 | 1.51 | HRV |
| 49 | 6.7 | 4 | 138 | 78 | 28 | 59 | 50 | 105 | 12 | 1.68 | INGV |
| - | - | - | - | - | - | 69 | 46 | 166 | - | - | KAN |
| - | - | 9 | 138 | 45 | 39 | 81 | 67 | 139 | - | - | MEDNET |
| 75 | 6.7 | 1 | 296 | 21 | 28 | 70 | 75 | 165 | - | - | Nikolintaga <i>et al.</i> , 2008 |
| 100 | 6.4 | - | - | - | - | 75 | 42 | 102 | - | 0.38 | NOA |
| 55 | 6.8 | 6 | 134 | 47 | 36 | 75 | 63 | 137 | 15 | - | SED |
| 66 | 6.7 | 6 | 125 | 69 | 18 | 52 | 55 | 115 | - | 1.70 | USGS |
| 60 | 6.5 | - | - | - | - | 62 | 57 | 121 | 7 | 0.82 | Yolsal and Taymaz, 2012 |
| - | 6.0 ⁴ | 11 | 129 | 40 | 30 | 73 | 71 | 156 | - | 0.80 ⁵ | This study – polarities / spectra |
| 70 | 6.6 | - | - | - | - | 65 | 60 | 114 | 12 | 0.87 | This study - inversion |

3.4 February 2008 – Methoni earthquakes

On February 14, 2008 at 10:09:25 UTC a $M_w=6.6$ earthquake occurred in the southwestern part of the Hellenic Arc at 34.779°N 23.397°E (<http://geophysics.geo.auth.gr>), with focal depth 34.6 km. It was followed by two more strong events, one struck two hours later (12:08:56 UTC) at 36.438°N 22.026°E , with magnitude $M_w=6.0$ and depth 34 km. The last one occurred six days later, on

⁴ Moment magnitude obtained by the empirical relation of Hanks and Kanamori (1979).

⁵ Scalar moment obtained by far-field displacement amplitude spectra of P-waves.

February 20, 2008, at 36.363°N 21.907°E, with magnitude $M_w=6.0$ and focal depth 9.4 km.

3.4.1 14 February 2008 $M_w=6.6$ earthquake

The first earthquake epicenter was determined south of the town of Methoni, in the entrance of Messiniakos Gulf, S Peloponnese. The earthquake was felt in the southern half of Greece, as well as in Cairo (Egypt) and southern Italy. No injuries were reported and only minor damage was observed (ITSACK, 2008; Roumelioti *et al.*, 2009). The focal mechanism was given as a pure thrust fault with one nearly horizontal and another nearly vertical plane (gCMT, <http://www.globalcmt.org/>). This earthquake lies in the trench of the Hellenic subduction zone, along which deformation is taken up by reverse low-angle thrust faulting (Taymaz *et al.*, 1990; Kiratzi and Louvari, 2003; Benetatos *et al.*, 2004). Considering this seismotectonic frame of the focal region, the low-dipping plane is identified as the fault plane (Papazachos and Papazachou, 1997; Sokos *et al.*, 2008; Roumelioti *et al.*, 2009).

3.4.1.1 Focal mechanism solution from P-wave polarities

For the determination of the fault plane solution with the method of P-wave polarities, 32 IRIS stations between 10° and 90° epicentral distance with adequate azimuthal coverage were used. Fig. 3.20 shows the solution obtained, corresponding to a reverse fault with nodal planes trending NW-SE with one plane almost vertical (dip=78°) and the other almost horizontal (dip=12°). Besides the orientation of the nodal planes, the orientation of the T and P axes is also calculated, with the first being steeper, as expected for reverse faults. Fig. 3.21 shows the equivalent solution obtained by gCMT, being similar to the one previously determined in this study. According to the well-known seismotectonic frame of the under study area, the low-dipping plane is identified as the fault plane (Papazachos *et al.*, 1998; Sokos *et al.*, 2008; Roumelioti *et al.*, 2009).

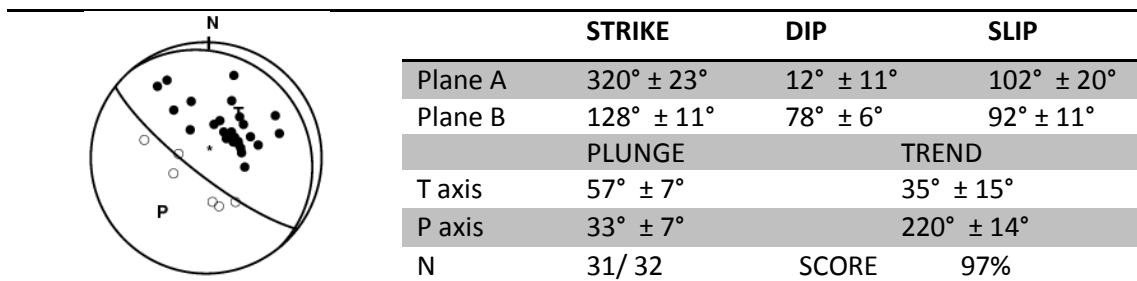


Fig. 3.20 Fault plane solution as lower hemisphere equal area projection for the February 14, 2008 $M_w=6.6$ Methoni earthquake. The notations and symbols are the same as in Fig. 3.2.

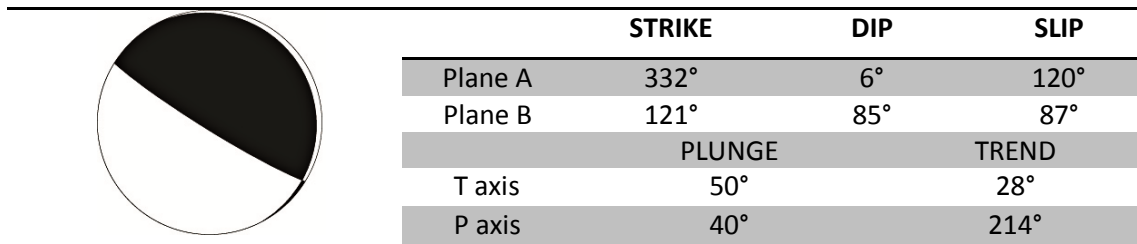


Fig. 3.21 Fault plane solution as lower hemisphere equal area projection for the February 14, 2008 $M_w=6.6$ Methoni earthquake according to gCMT. Black quadrants denote areas of compression, empty quadrants denote areas of dilatation.

3.4.1.2 Depth determination

Depths ranging from 10 km to 60 km with an interval of 5 km were considered at first. The depths that show less rms error are between 25 km and 35 km, the least being at 30 km (0.2810, Fig. 3.22). A more detailed test of the depth using an interval of 1 km, defines the optimal depth to be at 30 km, too (Fig. 3.23).

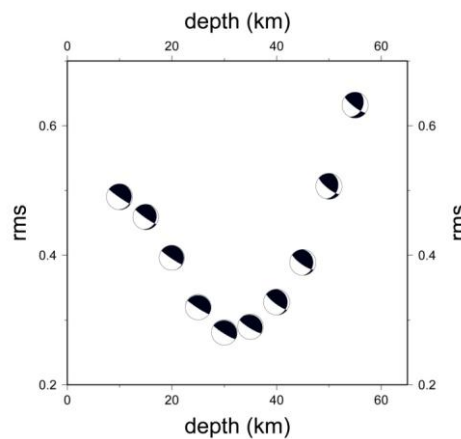


Fig. 3.22 Rms to depth diagram with an interval of 5 km for the February 14, 2008 $M_w=6.6$ Methoni earthquake. Symbols are the same as in Fig. 3.5

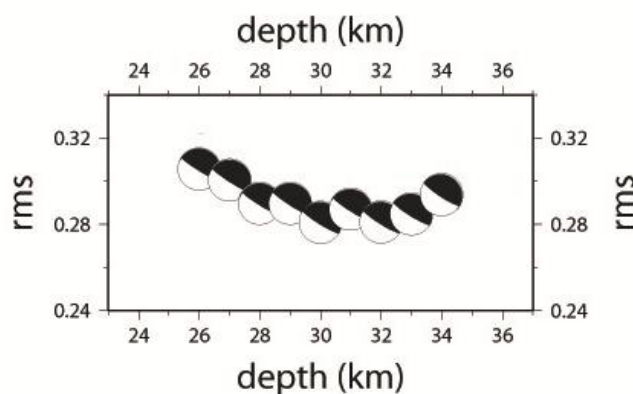


Fig. 3.23 Rms to depth diagram for the February 14, 2008 $M_w=6.6$ Methoni earthquake, with an interval of 1 km. Symbols are the same as in Fig. 3.5

Altogether, 12 P and 7 SH waveforms were chosen for the inversion, which had agreement between observed and synthetic seismograms and high signal-to-noise ratio. Trying to avoid upper mantle triplications and interference from the outer core, the distance range of the data was between 30° and 90° here too.

As in most body wave inversions, a double couple source was assumed. The source time function selected was a triangular one, with rise time $\tau_r=2$ seconds. This result was the best obtained for a number of different combinations. The duration of the source time function is equal to 18 seconds and consists of 6 subevents with the same duration but different amplitudes. The duration of the data to be inverted is 40 seconds and the fault plane solution is the one that has been obtained by MECSTA, having undergone some changes by experience, in order for the fit to be the best possible.

3.4.1.3 Constraints on the fault plane

Strike values vary between 310° and 325° , every 5° (Fig. 3.24). It is pointed out that the changes in the rms as well as in the synthetic waveforms are small. The most representative of them are cited. All solutions show the same satisfactory results for AAK station; the amplitude of the synthetic waveform is similar in every test. A slight difference is noted in ENH station; for 310° the amplitude of the synthetic wave is a little greater than for the other values and for the observed waveform. The same goes for MBAR station, only the amplitude corresponding to 310° fits best the observed amplitude. Finally, station CHTO shows no significant changes, as noted already for AAK. For the value of 325° , generally smaller amplitudes than the observed are noted for the synthetic waveform. This is reflected upon the rms error, which, though small, is greater than all other values. In order to conclude to the best strike, the rms again plays the most significant role, since the waveform differences between 315° and 320° are trivial to optical evaluation. Thus, the best strike is settled on 315° , in contrast with the solution obtained by MECSTA.

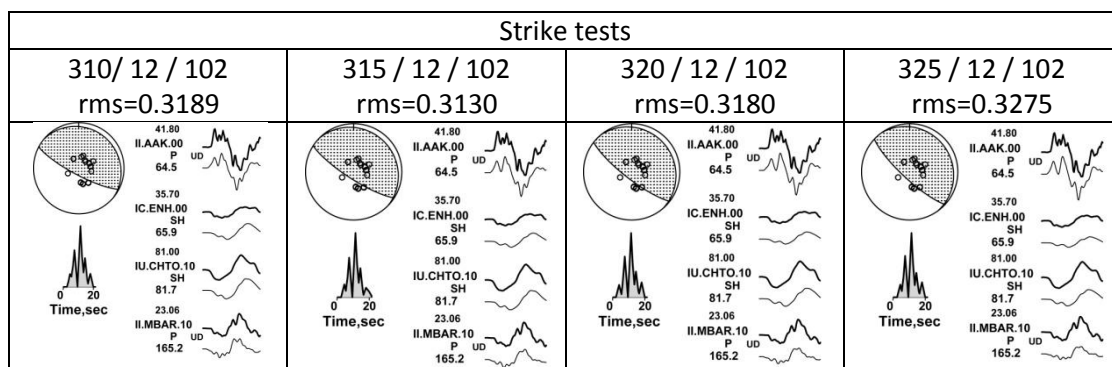


Fig. 3.24 Results of the strike test for the February 14, 2008 $M_W=6.6$ earthquake. The notations and symbols are the same as in Fig. 3.9.

By keeping the strike and rake constant and changing the dip between 2° and 17° every 5° , the best fitting dip value is found (Fig. 3.25). Here, too, the differences between the stations for different values are minimal. The most important is the smaller amplitude of station PALK for 2° and 7° . Once again, the value that corresponds to the smallest rms, since no obvious visual differences are noted, is that of 12° , in accordance to MECSTA calculations.

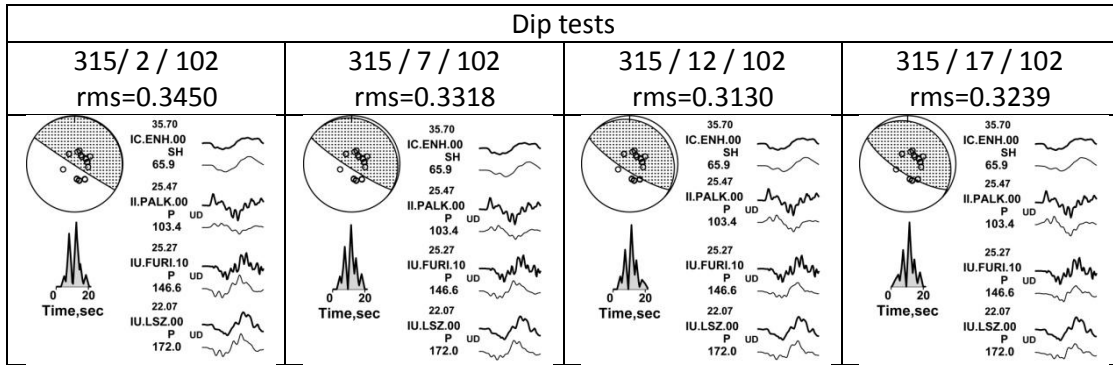


Fig. 3.25 Results of the dip test for the February 14, 2008 $M_W=6.6$ earthquake. The notations and symbols are the same as in Fig. 3.9.

Keeping the strike and dip values constant, the best rake is obtained (from 92° to 122° , Fig. 3.26). Here, the rms changes are greater and reflected more clearly upon the synthetic waveforms. Station XAN returns an almost straight line for the first value. For 102° the curve is “corrected”. For the rest of the values, the curves and amplitudes of the waveforms are bigger than the observed. For station LSZ, the upward peak is best inverted for the second value; for 92° it is quite smaller with no obvious polarity, for 112° and 122° it is greater but still smaller than for 102° . In station RCBR, for the first, third and fourth values, i.e. 92° , 112° and 122° , the initial part of the waveform does not show any polarity. Finally, FFC shows insignificant changes in all four tests. Therefore, the best rake is of 102° , in accordance with the solution obtained by MECSTA.

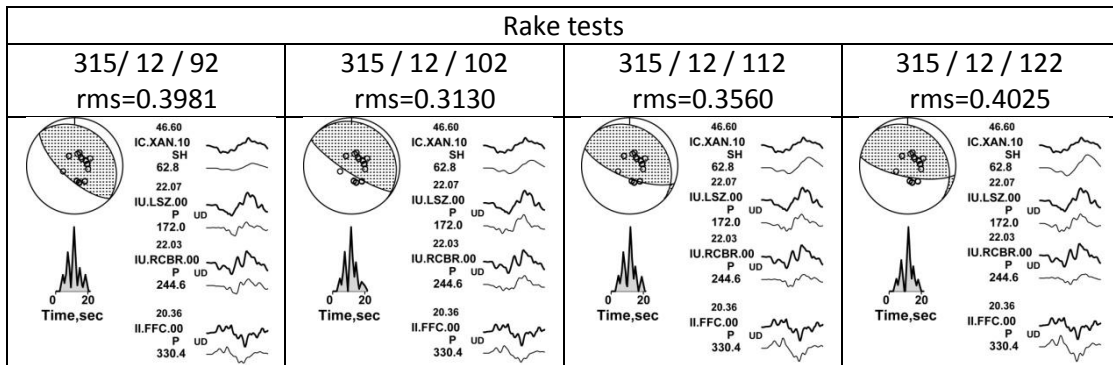


Fig. 3.26 Results of the rake test for the February 14, 2008 $M_W=6.6$ earthquake. The notations and symbols are the same as in Fig. 3.9.

3.4.1.4 Results

The results of the final inversion are shown in Fig. 3.27. The source time function has already been described before the tests. The final plane orientation is shown in the beach ball. The source time function, below the diagram is of 18 s, whereas the waveform duration is 40 minutes (scale over the waveforms). The magnitude of the earthquake is $M_W=6.6$ and the scalar moment $M_0=1.07 \cdot 10^{19}$. The diagram of dip and strike, which is a representation of the seismic fault, shows the asperities that were broken causing the earthquake. Each asperity has different size corresponding to different amplitudes represented in the source time function. An important aspect is that in the same area of the fault, two asperities broke. With this

method determining the time series of the rupturing asperities is not possible. Good agreement is noted between the synthetic and observed waveforms. The amplitude, as well as the first polarities and the majority of the peaks have been imprinted on the inverted data. The small rms error of this solution accounts for it. The weights of P and SH waves and the amplitude normalization factors the values are as described above. Table 3.3 lists information on source parameters provided by different Institutions.

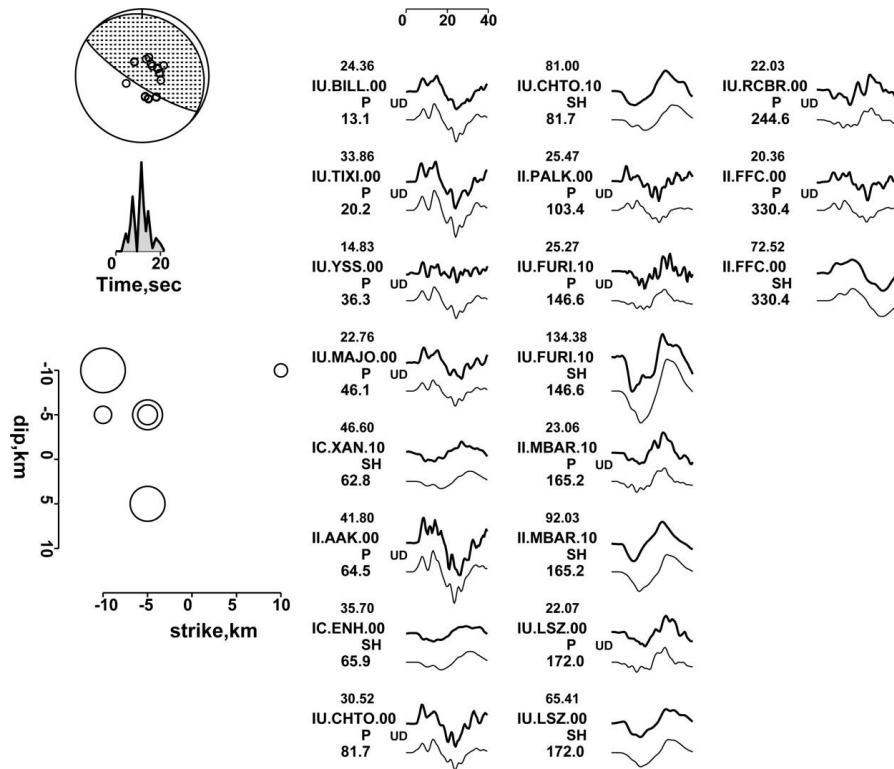


Fig. 3.27 Final inversion of the February 14, 2008 $M_w=6.6$ Methoni earthquake. The notations and symbols are the same as in Fig. 3.8.

Table 3.3 Fault plane solutions from different references for the February 14, 2008 $M_w=6.6$ Methoni earthquake. Given parameters are the depth in km, the M_w , the orientation of the compressional and tensional axes, the nodal planes orientation, the duration in seconds of the source time function and the scalar moment in Nm. AUTH: Aristotle University of Thessaloniki; HRV:CMT-Harvard; INGV: Istituto Nazionale di Geofisica e Vulcanologia; NOA: National Observatory of Athens; USGS: U.S. Geological Service.

| Depth (km) | M_w | P-plunge (°) | P-azimuth (°) | T-plunge (°) | T-azimuth (°) | Strike (°) | Dip (°) | Slip (°) | STF (s) | Mo ($*10^{19}$ Nm) | References |
|------------|-------|--------------|---------------|--------------|---------------|------------|---------|----------|---------|---------------------|---------------------------------|
| 34 | 6.7 | - | - | - | - | 290 | 10 | 70 | - | 1.24 | AUTH |
| 20 | 6.8 | 40 | 214 | 50 | 28 | 332 | 6 | 120 | 15 | 2.37 | HRV |
| 39 | 6.7 | 29 | 226 | 60 | 32 | 333 | 17 | 111 | - | 1.20 | INGV |
| 29 | 6.6 | - | - | - | - | 302 | 7 | 116 | - | 0.84 | NOA |
| 30 | 6.7 | - | - | - | - | 288 | 10 | 73 | 16 | 1.46 | Roumelioti <i>et al.</i> , 2009 |
| 29 | 6.9 | 35 | 219 | 55 | 32 | 325 | 11 | 108 | - | 1.48 | USGS |
| - | - | 33 | 220 | 57 | 35 | 301 | 12 | 94 | - | - | This study – polarities |
| 30 | 6.6 | - | - | - | - | 315 | 12 | 102 | 18 | 1.07 | This study - inversion |

3.4.2 14 February 2008 $M_w=6.0$ earthquake

On February 14, 2008, at 12:08:57 UTC, two hours after the $M_w=6.6$ first earthquake, a $M_w=6.0$ strong event followed to the southeast of the same area. The

epicenter was at 36.438°N – 22.026°E, south of Peloponnese and to the SE of the first event. The focal depth was estimated at 8.6 km (<http://geophysics.gro.auth.gr>). The focal mechanism was given as a pure thrust fault with one nearly horizontal and another nearly vertical plane (global CMT catalog, <http://www.globalcmt.org/>), similar to the solution for the first event. According to the well-known seismotectonic frame of the under study area, the low-dipping plane is identified as the fault plane (Papazachos *et al.*, 1998; Sokos *et al.*, 2008; Roumelioti *et al.*, 2009).

3.4.2.1 Focal mechanism solution from P-wave polarities

The first P-wave arrivals from 27 IRIS stations between 10° and 90° epicentral distance were used for the determination of the fault plane orientation and plane solution. The solution obtained corresponds to a thrust fault with nodal planes extending NW-SE, one being horizontal and the other vertical (dip=12° and dip=78° respectively, Fig. 3.28). Besides the orientation of the nodal planes, the orientation of the T and P axes were also calculated with the same program. As expected in thrust faults, the P axis is more horizontal (33°) than the T axis (57°).

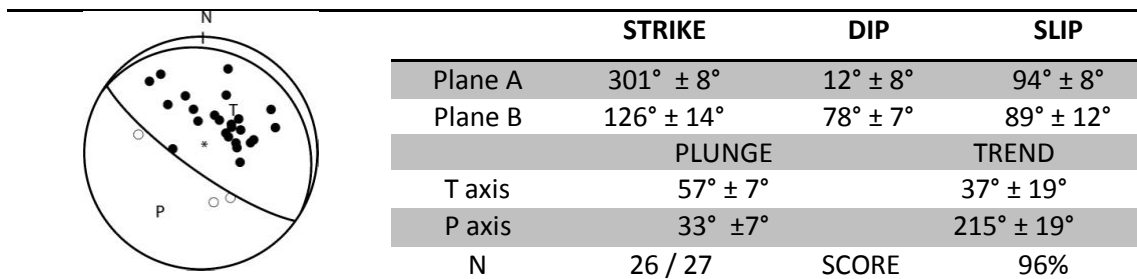


Fig. 3.28 Fault plane solution as lower hemisphere equal area projection for the February 14, 2008 $M_w=6.0$ Methoni earthquake. The notations and symbols are the same as in Fig. 3.2.

In Fig. 3.29 the fault plane solution of gCMT is cited. Differences concern the strike and dip of the shallow-dipping plane; in the gCMT the strike extends more to the north and the angle of dip is smaller than the solution of proposed by this study.

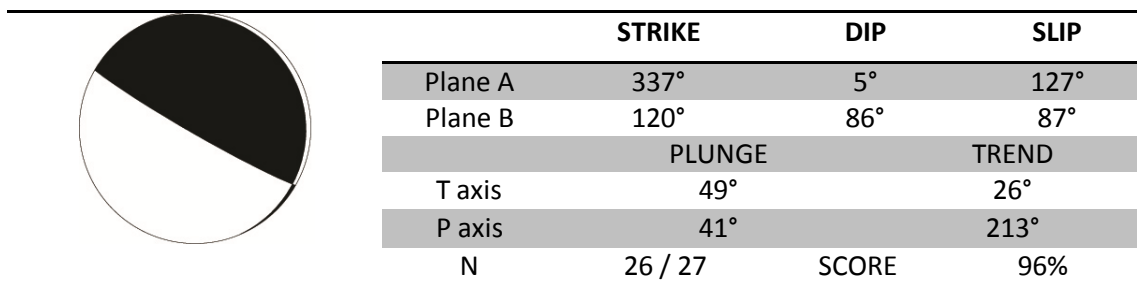


Fig. 3.29 Fault plane solution as lower hemisphere equal area projection for the February 14, 2008 $M_w=6.0$ Methoni earthquake according to gCMT. Black quadrants denote areas of compression, empty quadrants denote areas of dilatation.

A comparison between this earthquake and the first strong February, 2008 event shows similar fault plane solutions, consequently connecting the two events in time (rupture with two hours time difference), geographical region (same epicentral area) and faulting mechanism.

3.4.2.2 Depth determination

For the depth determination, 13 P waveforms were processed. Trying to avoid upper mantle triplications and interference from the outer core, the distance range of the data was between 30° and 90°. Fig. 3.30 shows the rms to depth distribution. Only P-waves were considered, with depths ranging from 20 km to 50 km with a 5 km interval. The least rms errors are observed between 25 km and 35 km (0.4537 and 0.4143, respectively).

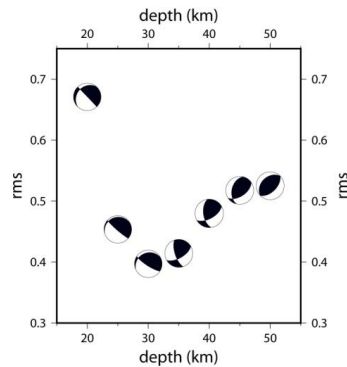


Fig. 3.30 Rms to depth diagram with an interval of 5 km for February 14, 2008 $M_w=6.0$ Methoni earthquake. Symbols are the same as in Fig. 3.5.

Next, refinement of the depth is performed for the above said depth ranges by changing the depth approximation with a step of 1 km. The difference in rms is little for depths between 29 km and 33 km (Fig. 3.31). Nevertheless, the least error is observed at 32 km, and thus this is considered to be the focal depth.

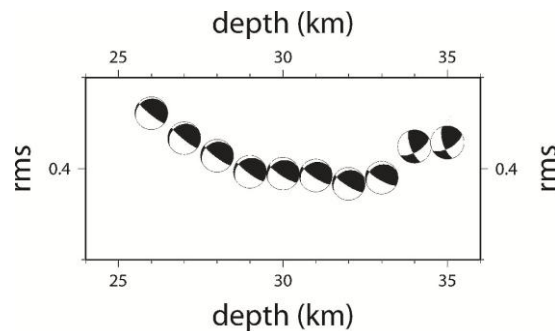


Fig. 3.31 Rms to depth diagram with an interval of 1 km for the February 14, 2008 $M_w=6.0$ Methoni earthquake. Symbols are the same as in Fig. 3.5.

3.4.2.3 Constraints to the fault plane

As far as the strike is concerned, the best value is 301°, as seen in Fig. 3.32. For all stations, a progressive reduction of the amplitude is observed, from 291° to 321°. The best fitting strike is understood by the least rms and the concordance of observed and synthetic data.

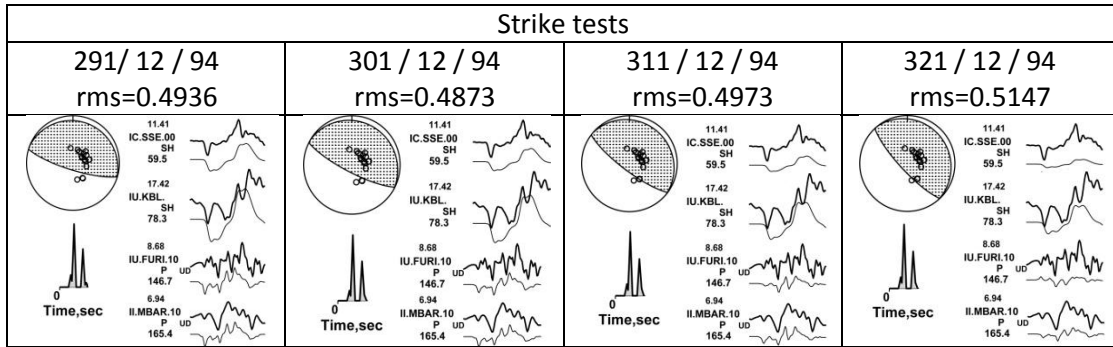


Fig. 3.32 Results of the strike test for the February 14, 2008 $M_W=6.0$ Methoni earthquake. The notations and symbols are the same as in Fig. 3.9.

For the dip of the fault, the most remarkable change during the tests is for PALK station (Fig. 3.33). For the first value of 2° , the synthetic waveform is nearly a straight line. With the progressive increase of the dip, the amplitude increases. Since the differences are minimal, apart from PALK, the least rms provides the best dip of the seismic fault. Hence, so far the strike and dip have been determined ($301^\circ / 15^\circ$).

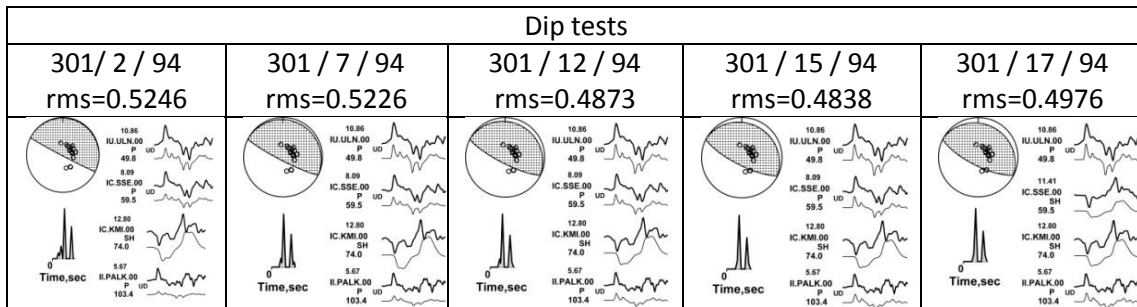


Fig. 3.33 Results of the dip test for the February 14, 2008 $M_W=6.0$ Methoni earthquake. The notations and symbols are the same as in Fig. 3.9.

Finally, for the rake, the test values are between 74° and 104° (Fig. 3.34). While changing these values with an interval of 10° , the amplitude of SSE, FURI (P-waveform) and ALE increases, whereas the amplitude of FURI (SH-waveform) decreases progressively. The best fit between this increase and decrease is settled for 94° , in agreement with P-wave polarities results.

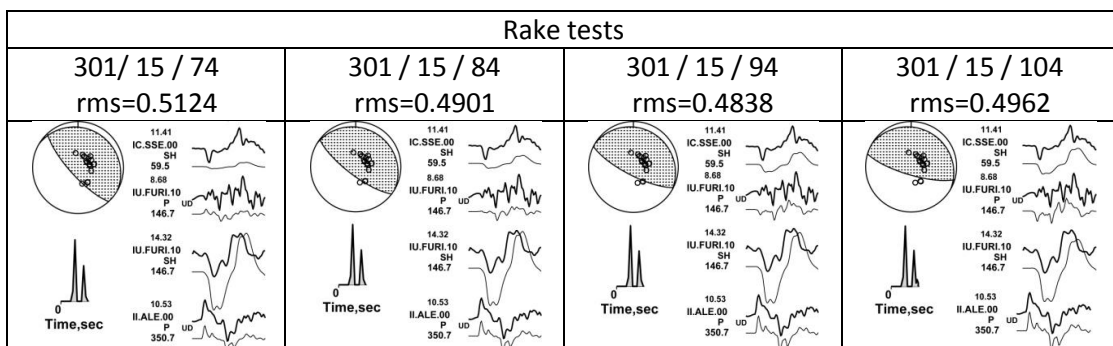


Fig. 3.34 Results of the rake test for the February 14, 2008 $M_W=6.0$ Methoni earthquake. The notations and symbols are the same as in Fig. 3.9.

3.4.2.4 Results

For the inversion, a double couple source was assumed. The source time function selected was a triangular one, with rise time $\tau_r=1$ second. The duration of the source time function is of 7 seconds and consists of 4 subevents (Fig. 3.35). The duration of the data to be inverted is 40 seconds and the fault plane solution is the one that has been obtained by MECSTA, having undergone some changes by experience, in order for the fit to be the best possible. Two were biggest asperities ruptured at the same area. The magnitude of the earthquake is determined to be $M_w=6.0$ and scalar moment $M_0=0.143 \cdot 10^{19}$. Table 3.4 lists information on source parameters provided by different Institutions.

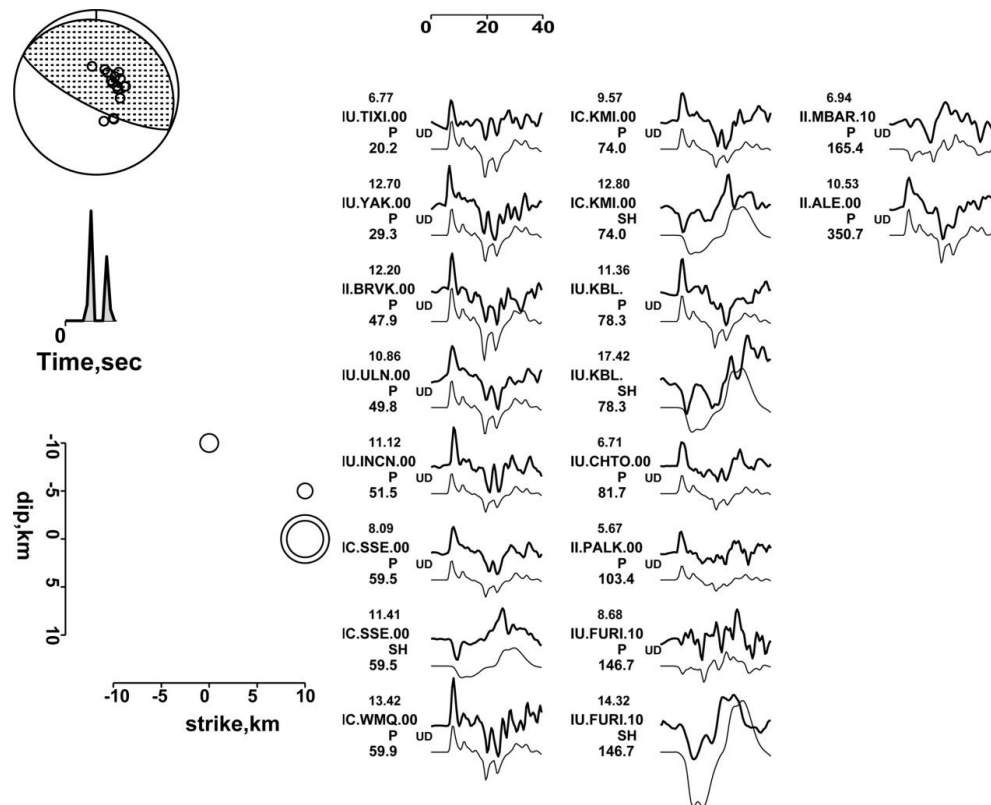


Fig. 3.35 Final inversion of the February 14, 2008 $M_w=6.0$ Methoni earthquake. The notations and symbols are the same as in Fig. 3.8.

Table 3.4 Fault plane solutions from different references for the February 14, 2008 $M_w=6.0$ Methoni earthquake. Given parameters are the depth in km, the M_w , the orientation of the compressional and tensional axes, the nodal planes orientation, the duration in seconds of the source time function and the scalar moment in Nm. AUTH: Aristotle University of Thessaloniki; HRV:CMT-Harvard; INGV: Istituto Nazionale di Geofisica e Vulcanologia; NOA: National Observatory of Athens; USGS: U.S. Geological Service.

| Depth (km) | M_w | P-plunge (°) | P-azimuth (°) | T-plunge (°) | T-azimuth (°) | Strike (°) | Dip (°) | Slip (°) | STF (s) | M_0 ($\cdot 10^{19}$ Nm) | References |
|------------|-------|--------------|---------------|--------------|---------------|------------|---------|----------|---------|-----------------------------|---------------------------------|
| 34 | 6.2 | - | - | - | - | 292 | 8 | 74 | - | 0.19 | AUTH |
| 15 | 6.5 | 41 | 213 | 49 | 26 | 337 | 5 | 127 | 8 | 0.08 | HRV |
| 12(fixed) | 6.4 | 39 | 212 | 51 | 33 | 298 | 6 | 85 | - | 0.47 | INGV |
| 26 | 6.1 | - | - | - | - | 303 | 20 | 82 | - | 0.16 | NOA |
| 33 | 6.1 | 27 | 220 | 63 | 38 | 312 | 18 | 93 | 10 | 0.17 | Roumelioti <i>et al.</i> , 2009 |
| 28 | 6.5 | 31 | 209 | 59 | 23 | 307 | 14 | 100 | - | 0.13 | USGS |
| - | - | 33 | 215 | 57 | 37 | 301 | 12 | 94 | - | - | This study - polarities |
| 32 | 6.0 | - | - | - | - | 301 | 15 | 94 | 7 | 0.14 | This study - inversion |

3.4.3 20 February 2008 $M_w=5.9$ earthquake

On February 20, 2008 at 18:27:08 UTC, six days after the two strong earthquakes that occurred offshore south Peloponnese, a third strong ($M_w=5.9$) event struck just south of the first event epicenter ($36.363^\circ\text{N } 21.907^\circ\text{E}$) at shallower depth of 9.4 km (<http://geophysics.geo.auth.gr>). In the epicentral area of this earthquake, deformation is mostly taken up by low-angle reverse faults, denoting the subduction process taking place (Taymaz *et al.*, 1990; Papazachos *et al.*, 1998; Kiratzi and Louvari, 2003; Benetatos *et al.*, 2004). For the determination of the fault plane, inversion was carried out on both nodal planes; the nodal plane for which inversion returned the least rms error results was considered to be the fault plane, thus the NNW-SSE striking plane (Chapter 3.4.3.3).

3.4.3.1 Focal mechanism solution from P-wave polarities

The vertical component of 20 IRIS stations between 10° and 90° epicentral distance were used for the determination of the focal mechanism. The data were chosen so that adequate azimuthal coverage and high signal-to-noise ratio were achieved. Fig. 3.36 shows the focal mechanism obtained, which evidences either left lateral motion on an ENE-WSW almost vertical (75°) fault or right-lateral motion on a NNW-SSE vertical (83°) fault.

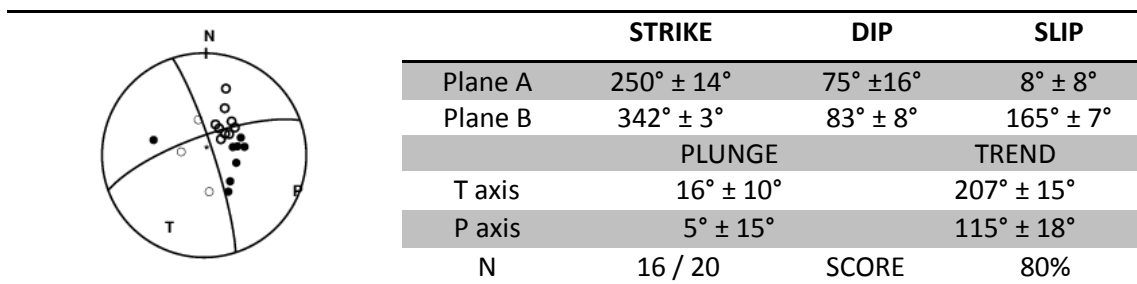


Fig. 3.36 Determination of the fault plane solution as lower hemisphere equal area projection for the February 20, 2008 $M_w=5.9$ Methoni earthquake. The notations and symbols are the same as in Fig. 3.2.

Fig. 3.37 presents the corresponding focal mechanism obtained by the gCMT. Both solutions have very similar features. The only difference is the slip of both planes; this study proposes strike-slip motion with some reverse component whereas gCMT solution proposes strike-slip motion with some normal component.

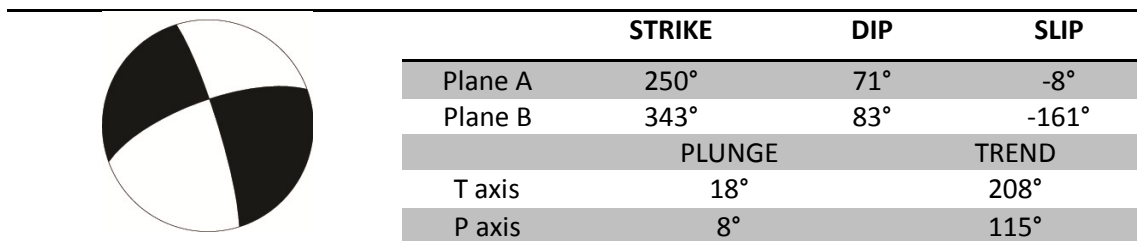


Fig. 3.37 Fault plane solution as lower hemisphere equal area projection for the February 20, 2008 $M_w=5.9$ Methoni earthquake, according to gCMT. Black quadrants denote areas of compression, empty quadrants denote areas of dilatation.

3.4.3.2 Depth determination

Only P-waves were considered and inversion was carried out for different depths from 15 km to 40 km with a 5 km step. This range was chosen after considering the different focal depths listed in Table 3.5. The smallest rms errors are observed between 5 km and 15 km (0.5205 and 0.7808 respectively, Fig. 3.38).

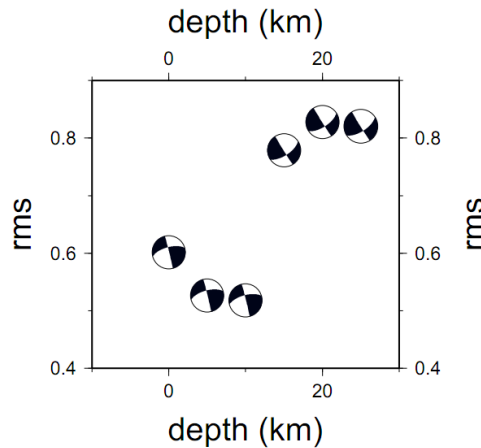


Fig. 3.38 Rms to depth diagram with a 5 km step for the the February 20, 2008 $M_w=5.9$ Methoni earthquake. Only P-waves are inverted.

Depths between these values were further investigated, with 1 km step, giving the rms to depth diagram shown in Fig. 3.39. The final depth is constrained at 11 km (rms=0.4959).

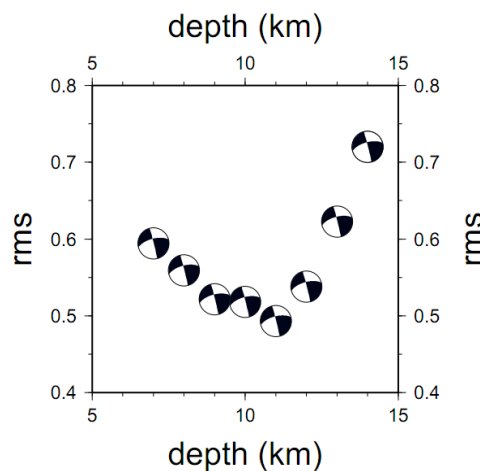


Fig. 3.39 Rms to depth diagram with 1 km step for the February 20, 2008 $M_w=5.9$ Methoni earthquake. Notations and symbols are the same as in Fig. 3.5.

3.4.3.3 Constraints on the fault plane

The two nodal planes from P-wave polarities that were tested with bodywave inversion were $342^\circ/83^\circ/165^\circ$ and $250^\circ/75^\circ/8^\circ$ with the first exhibiting the best fit. Afterwards, the N-S trending plane underwent changes regarding the rake in order to determine whether the value obtained by MECSTA was optimal one. However,

the tests carried out only to the rake provided a range of values from -165° to -145° with -155° being the best fitting solution. The tests following are applied to the aforementioned N-S striking plane

For constraining the strike, values from 337° to 352° were tested, with a 5° step. The waveforms remained mostly unaffected with the change of the strike value, as it can be seen in Fig. 3.40 and this can be confirmed by the small changed in the rms error, the least value of which is observed for 347° . However, the strike value chosen is equal to 342° (in concordance with the MECSTA solution), because in some cases, the least rms strike overdetermines the synthetic waveforms (i.e. in station TIXI, where the synthetic amplitude and slope are greater than the observed). Next, the dip undergoes testing, varying between 78° and 88° with a 5° step, with the intermediate value exhibiting the best fit and least rms (Fig. 3.41). Since no significant changes are observed, this is considered the apt value. Finally, Fig. 3.42 shows the rake tests, changing from -165° to -135° . Although the least rms errors corresponds to the values of -135° and -145° , the value of -155° is chosen for the final inversion because, despite the smaller rms, the amplitudes of most waveforms are best approached for the chosen value.

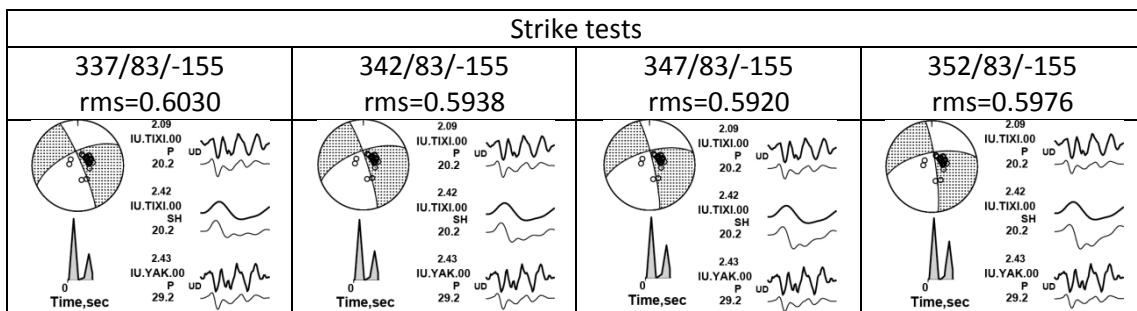


Fig. 3.40 Results of the strike test for the February 20, 2008 $M_W=5.9$ Methoni earthquake. The notations and symbols are the same as in Fig. 3.9.

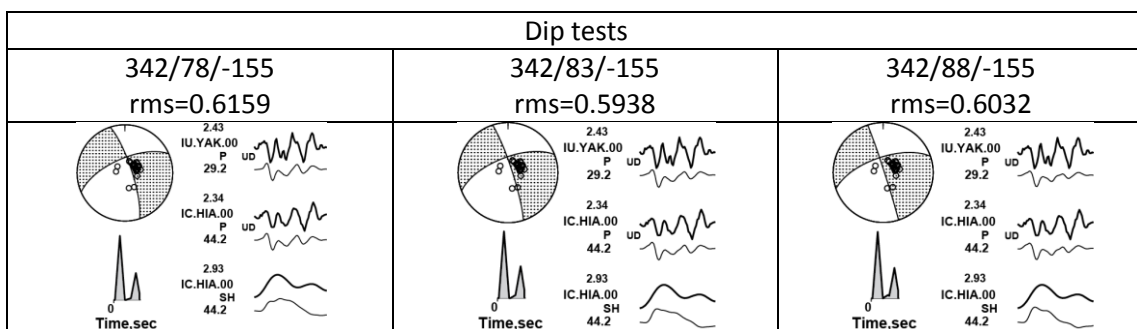


Fig. 3.41 Results of the dip test for the February 20, 2008 $M_W=5.9$ Methoni earthquake. The notations and symbols are the same as in Fig. 3.9.

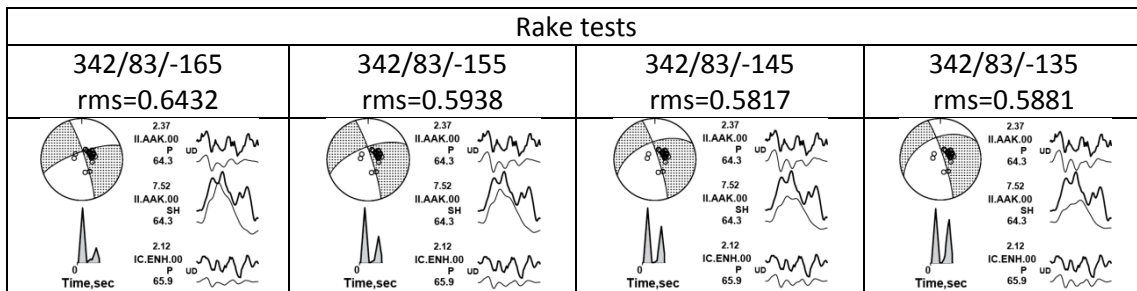


Fig. 3.42 Results of the rake test for the February 20, 2008 $M_w=5.9$ Methoni earthquake. The notations and symbols are the same as in Fig. 3.9.

3.4.3.4 Results

After a series of tests for the February 20, 2008 $M_w=5.9$ Methoni event, the determined parameters were 11 km focal depth and $342^\circ/83^\circ/-155^\circ$ final fault plane solution. Finally, the detailed inversion for the event inferred the results shown in Fig. 3.43. A double couple was assumed and a triangular source time function with rise time 1 second and five subevents of total duration of ~ 8 s. The spatial distribution of these subevents (asperities) is shown in the diagram of strike and dip (top right). The magnitude is $M_w=5.9$ and the scalar moment $M_0=0.097 \cdot 10^{19}$ Nm. Table 3.5 lists information on source parameters provided by different Institutions.

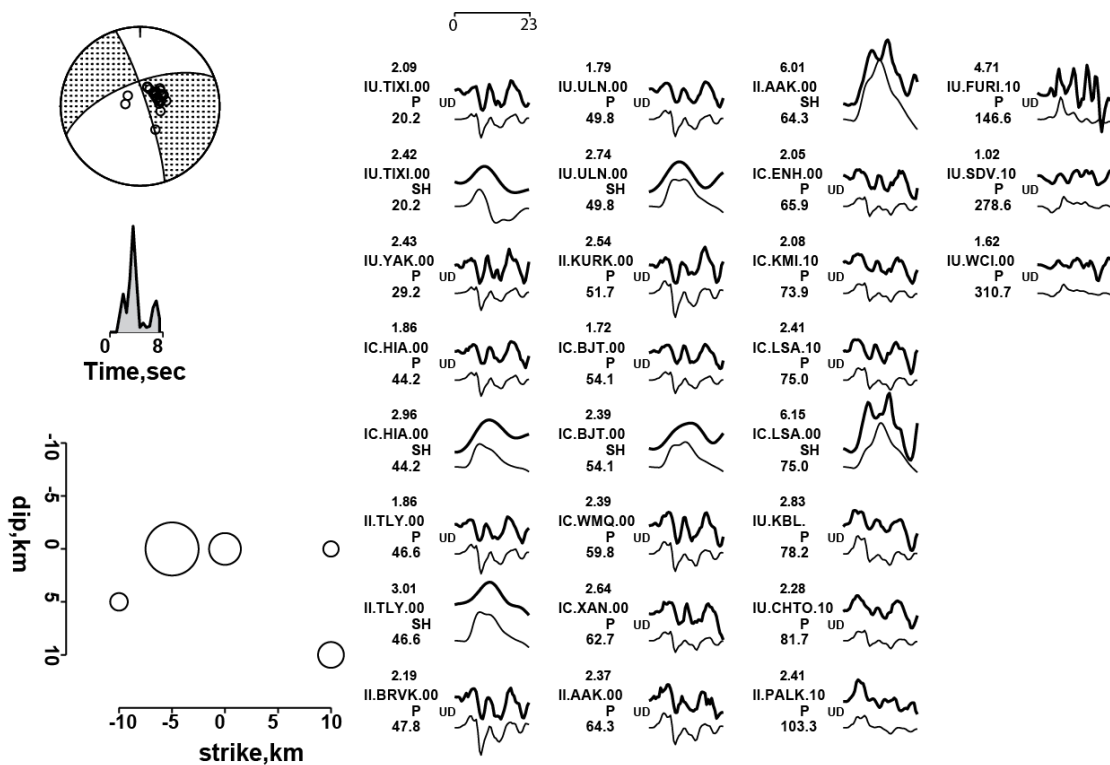


Fig. 3.43 Final inversion of the February 20, 2008 $M_w=5.9$ Methoni earthquake. The notations and symbols are the same as in Fig. 3.8. Fig. 3.35 Final inversion of the February 14, 2008 $M_w=6.0$ Methoni earthquake. The notations and symbols are the same as in Fig. 3.8.

Table 3.5 Fault plane solutions from different references for the February 20, 2008 $M_w=5.9$ Methoni earthquake. Given parameters are the depth in km, the M_w , the orientation of the compressional and tensional axes, the nodal planes orientation, the duration in seconds of the source time function and the scalar moment in Nm. AUTH: Aristotle University of Thessaloniki; HRV:CMT-Harvard; INGV: Istituto Nazionale di Geofisica e Vulcanologia; NOA: National Observatory of Athens; USGS: U.S. Geological Service.

| Depth (km) | M_w | P-plunge (°) | P-azimuth (°) | T-plunge (°) | T-azimuth (°) | Strike (°) | Dip (°) | Slip (°) | STF (s) | Mo ($\times 10^{19}$ Nm) | References |
|------------|-------|--------------|---------------|--------------|---------------|------------|---------|----------|---------|---------------------------|---------------------------------|
| 12 | 6.1 | - | - | - | - | 336 | 85 | 178 | - | 0.15 | AUTH |
| 18 | 6.2 | 8 | 115 | 18 | 208 | 343 | 83 | -161 | 6 | 0.22 | HRV |
| 20 | 6.2 | 10 | 203 | 7 | 294 | 339 | 78 | -178 | - | 0.26 | INGV |
| 16 | 6.1 | - | - | - | - | 344 | 85 | 176 | - | 0.15 | NOA |
| 10 | 6.0 | 19 | 211 | 16 | 296 | 344 | 88 | -155 | 10 | 0.14 | Roumelioti <i>et al.</i> , 2009 |
| 10 | 6.2 | 25 | 204 | 6 | 298 | 343 | 68 | -166 | - | 0.16 | USGS |
| - | - | 5 | 117 | 16 | 207 | 342 | 83 | 165 | - | - | This study - polarities |
| 11 | 5.9 | - | - | - | - | 342 | 83 | -155 | 8 | 0.10 | This study - inversion |

3.5 October 12, 2013 W Crete earthquake

The most recent earthquake studied ($M_w=6.5$) struck on October 12, 2013. Its epicenter was determined at 35.471°N 23.281°E with focal depth 47 km (<http://geophysics.geo.auth.gr>). It was felt in the Island of Crete, continental Southern Greece, eastern Italy and some cities in northern Africa (European-Mediterranean Seismological Centre, <http://www.emsc-csem.org>). Previous studies in the area as well as in subduction zones have shown that faults related to such geodynamic process are characterized by low-angle thrust faults dipping toward the convex side of the arc (see also 3.4.1.1). Therefore, the low-dipping NW-SE striking fault is determined as the fault plane.

3.5.1 Focal mechanism determination from P-wave polarities

The vertical component of 38 IRIS stations between 10° and 90° epicentral distance were used for the determination of the focal mechanism. The data were chosen so that adequate azimuthal coverage and high signal-to-noise ratio were achieved. Fig. 3.44 shows the focal mechanism obtained with MECSTA, evidencing reverse rupture either on a low-dipping (10°) fault or on a nearly vertical (80°) fault. A comparison with the gCMT solution (Fig. 3.45) shows 25° variance in the strike and 7° in the dip.

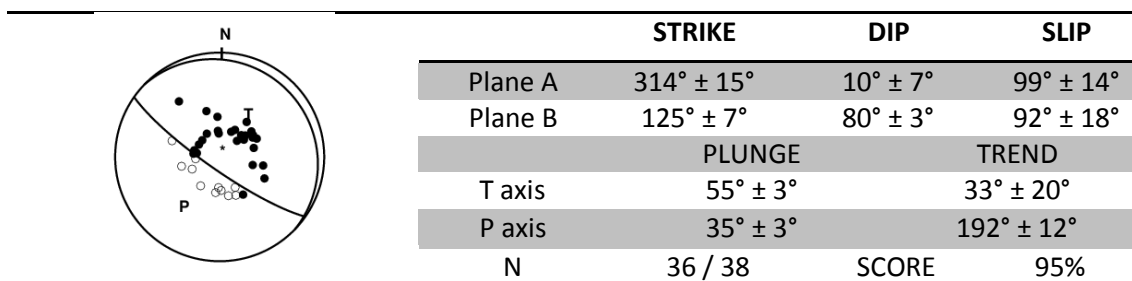


Fig. 3.44 Fault plane solution as lower hemisphere equal area projection for the October 12, 2013 $M_w=6.5$ W Crete earthquake. The notations and symbols are the same as in Fig. 3.2

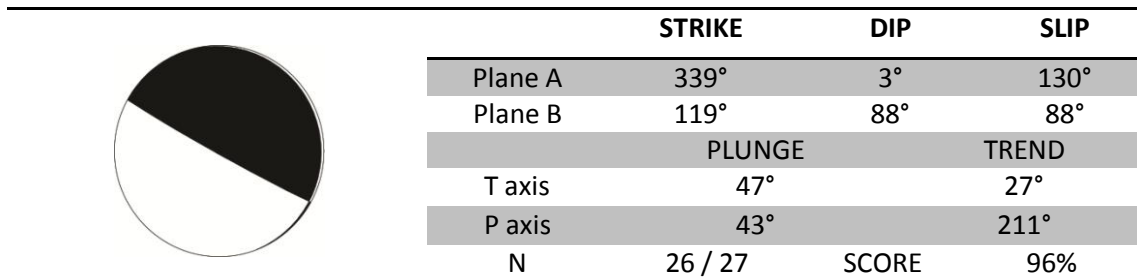


Fig. 3.45 Fault plane solution as lower hemisphere equal area projection for the October 12, 2013 $M_w=6.5$ W Crete earthquake, according to gCMT. Black quadrants denote areas of compression, empty quadrants denote areas of dilatation.

3.5.2 Depth determination

According to the different focal depths proposed by various Institutes (Table 3.6), a range of depths was examined, between 20 km and 65 km with 5 km step. The results of this test are presented in Fig. 3.46. The depth is then refined, by testing values from 40 km to 55 km with a step of 1 km (Fig. 3.47). The focal depth is determined by the least rms error at 49 km ($rms=0.1902$).

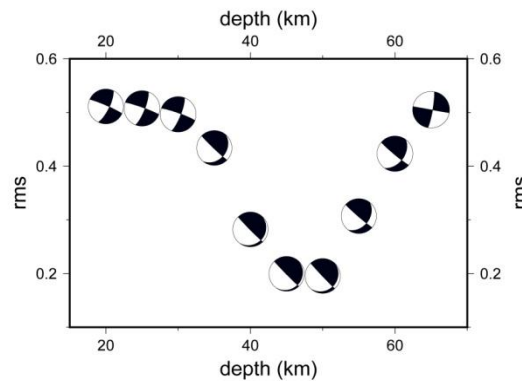


Fig. 3.46 Rms to depth diagram with a 5 km step for the October 12, 2013 $M_w=6.5$ W Crete earthquake. Only P-waves are inverted. Symbols are the same as in Fig. 3.5.

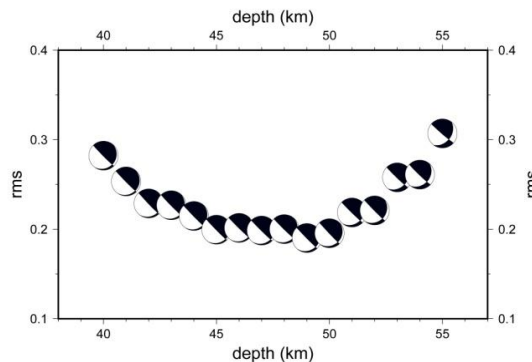


Fig. 3.47 Rms to depth diagram with an interval of 1 km for the October 12, 2013 $M_w=6.5$ W Crete earthquake. Symbols are the same as in Fig. 3.5.

3.5.3 Constraints on the fault plane

Using as a guide the MECSTA results on the fault plane solution (314/10/99) these parameters were further investigated. First the strike was tested for values between 294° and 324° with a 10° step. The least rms as well as best fitting synthetic waveforms were obtained for 314° (Fig. 3.48).

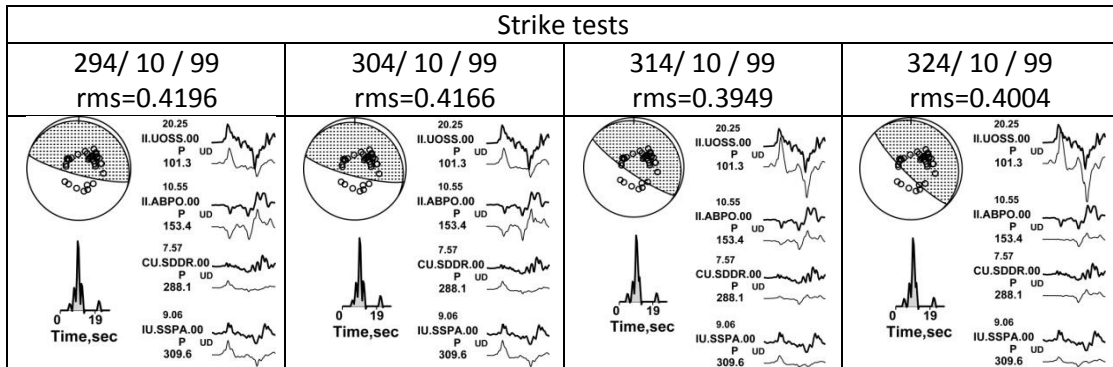


Fig. 3.48 Strike test results of the October 12, 2013 $M_w=6.5$ W Crete earthquake. The notations and symbols are the same as in Fig. 3.11.

Then, the dip of the plane was constrained for values from 5° to 15°. The results did not have significant differences in terms of the rms error (Fig. 3.49). However, while evaluating the waveforms optically, some changes were noticed. For example, the amplitude of ABPO station decreases whereas of WCI station increases for a steeper fault plane. Thus, the best solution would be the one for which both stations simultaneously are best simulated by the synthetic data. This case is confirmed with the smallest rms which is noted for 12°.

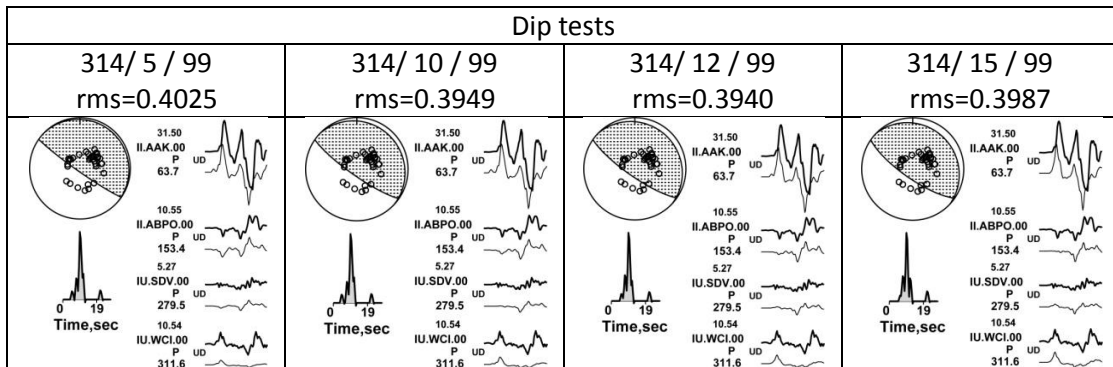


Fig. 3.49 Dip test results of the October 12, 2013 $M_w=6.5$ W Crete earthquake. The notations and symbols are the same as in Fig. 3.11

With 314° strike and 12° dip, the rake was varied between 79° and 109°, every 10° (Fig. 3.50). The reverse polarities observed for the first three values of rake (79°, 89° and 99°) at MSEY and ABPO stations are corrected for the last value. Moreover, the amplitude of the synthetic waveforms increases for all stations for greater rake values. The rms error is slightly greater for 109° than for 99°, but optical evaluation is better for the last value. Therefore, the fault plane is constrained at 314°/12°/109°.

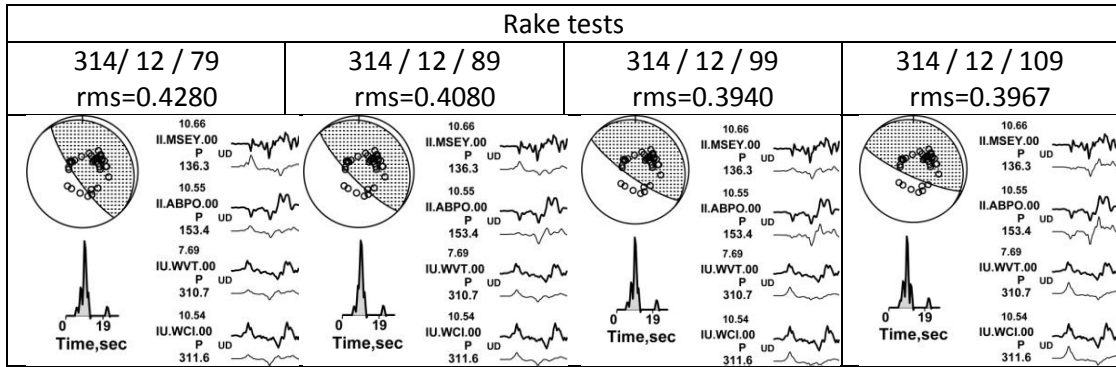


Fig. 3.50 Rake test results of the October 12, 2013 $M_W=6.5$ W Crete earthquake. The notations and symbols are the same as in Fig. 3.11.

3.5.4 Results

After the detailed investigation of the fault orientation, the final inversion is completed with strike 314° , dip 12° and rake 109° (Fig. 3.51). In total, 32 P-waveforms were inverted, using the first 26 seconds of each registration. A double couple was considered and a triangular source time function with 1.5s rise time, with total rupture duration 12s and 6 asperities of different size proportional to their rupture duration with spatial distribution described in the strike to dip diagram. The scalar moment is fund equal to $M_0=0.620 \cdot 10^{19}$ Nm and the magnitude $M_W=6.5$. Table 3.6 lists information on source parameters provided by different Institutions.

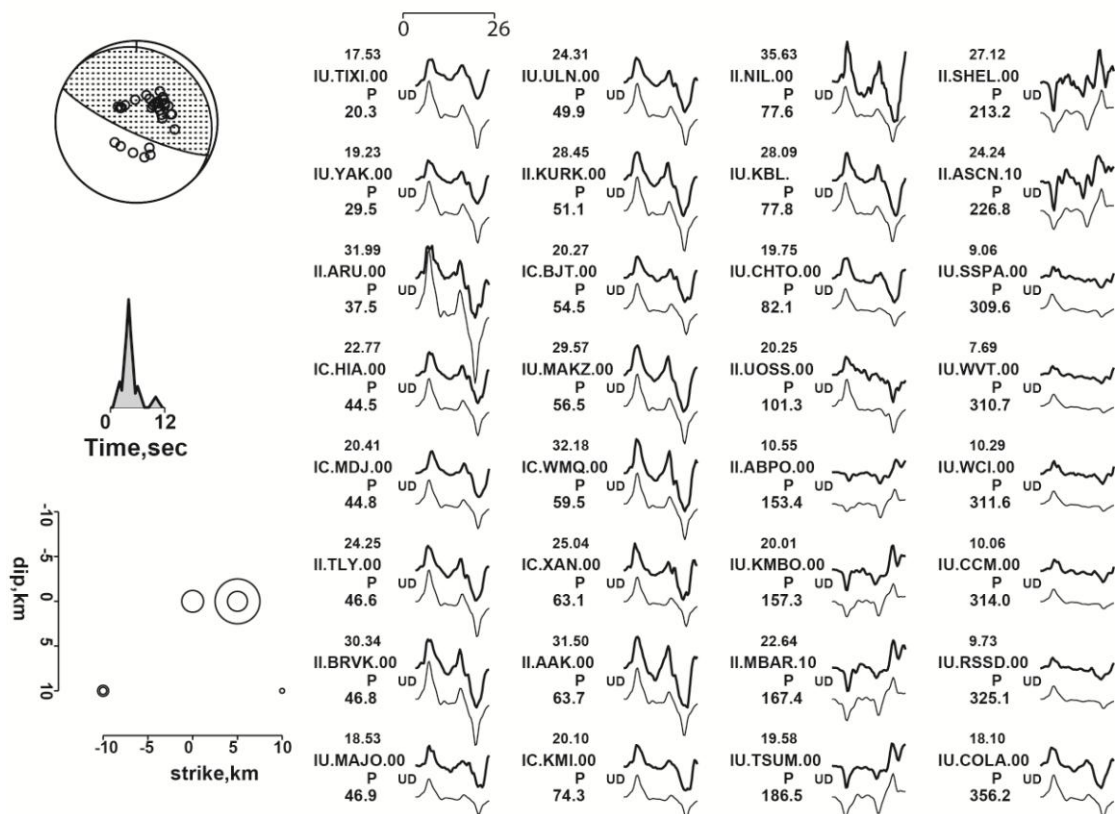


Fig. 3.51 Final inversion of the October 12, 2013 $M_W=6.5$ earthquake. The notations and symbols are the same as in Fig. 3.8.

Table 3.6 Fault plane solutions from different references for the October 12, 2013 W Crete earthquake. Given parameters are the depth in km, the M_w , the orientation of the compressional and tensional axes, the nodal planes orientation, the duration in seconds of the source time function and the scalar moment in Nm. AUTH: Aristotle University of Thessaloniki; AZUR: GEOAZUR, France; CPPT: CEA/DAM France; GFZ: GEOFON Program, Potsdam, Germany; HRV:CMT-Harvard; INGV: Istituto Nazionale di Geofisica e Vulcanologia; KAN: Kandilli Observatory and Earthquake Research Institute; NOA: National Observatory of Athens; USGS: U.S. Geological Service.

| Depth (km) | M_w | P-plunge (°) | P-azimuth (°) | T-plunge (°) | T-azimuth (°) | Strike (°) | Dip (°) | Slip (°) | STF (s) | Mo ($*10^{19}$ Nm) | References |
|------------|------------------|--------------|---------------|--------------|---------------|------------|---------|----------|---------|---------------------|-----------------------------------|
| 25 | 6.5 | 39 | 204 | 50 | 15 | 305 | 33 | 76 | - | 0.62 | AUTH |
| 47 | 6.5 | - | - | - | - | 353 | 15 | 143 | - | - | AZUR |
| 10 | 6.2 | 30 | 241 | 40 | 0 | 25 | 36 | 171 | 6 | 0.22 | CPPT |
| 25 | 6.5 | 39 | 213 | 50 | 44 | 262 | 8 | 44 | - | 0.63 | GFZ |
| 17 | 6.8 | 42 | 211 | 48 | 27 | 340 | 3 | 130 | 12 | 1.44 | HRV |
| 52(f) | 6.5 | 33 | 216 | 56 | 16 | 338 | 15 | 129 | 10 | 0.66 | INGV |
| 32 | 6.4 | - | - | - | - | 307 | 56 | 49 | - | 0.42 | KAN |
| 42 | 6.4 | 45 | 239 | 38 | 21 | 50 | 20 | -168 | - | 0.51 | NOA |
| 17 | 6.6 | 38 | 218 | 52 | 34 | 322 | 7 | 105 | - | 0.84 | USGS |
| - | 6.5 ⁶ | 35 | 192 | 55 | 33 | 314 | 10 | 99 | - | 0.62 ⁷ | This study - polarities / spectra |
| 49 | 6.5 | - | - | - | - | 314 | 12 | 109 | 12 | 0.62 | This study - inversion |

⁶ See Footnote 4.

⁷ See Footnote 5.

CHAPTER 4: FAULT PARAMETERS THROUGH SPECTRAL ANALYSIS

4.1 Introduction

Further insight is given in the largest and the more recent events studied, using the far-field amplitude displacement spectra. The data consist in the long-period P-waves recorded at teleseismic distances (30° - 90° epicentral distance). A time window before the first P-wave arrival and until the S-wave arrival was used. The waveforms were resampled with rate 0.2 s, corrected for the instrument response and attenuation and finally filtered using a band pass filter, according to the signal-to-noise ratio of each station. Fig. 4.1 shows the signal and noise spectra for the January 8, 2006 $M_w=6.6$ Kythera earthquake, as recorded in Yuzhno Sakhalinsk station, in Russia. The apt band pass filter that can be applied to the signal, in order to ensure that only the earthquake signal is processed is between 0.01 and 2 Hz. Finally, the data were also corrected for the radiation pattern, using an average radiation pattern over the focal sphere, which in the case of the P-waves is assigned the value $R_{\theta\phi}=0.52$ (Fletcher, 1980). Fig. 4.2 represents the general SAC script for the amplitude spectral analysis of the earthquakes. This script was applied to around a dozen different stations for each event, ensuring adequate azimuthal coverage. For all the calculations, the value of 6.6 km/sec was used for the P-wave velocity, 3.7 km/sec for S-wave velocity, a density of 2.6 gr/cm^3 was assumed and the shear modulus was considered to be $5.0 \cdot 10^{10} \text{ Nt/m}^2$.

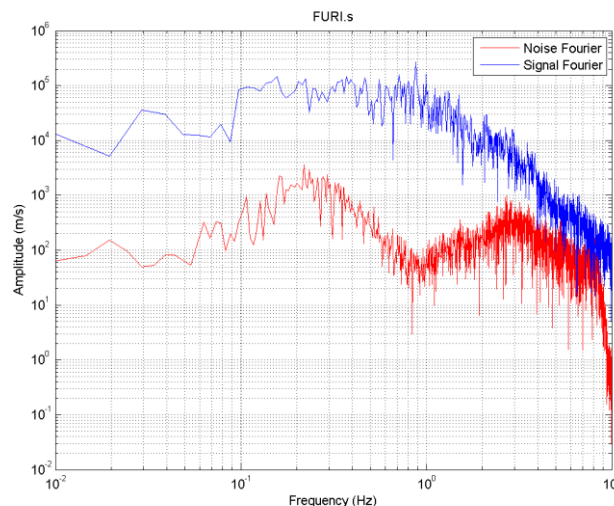


Fig. 4.1 Far-filed amplitude of the signal (blue) and the noise (red) of the January 8, 2006 Kythera earthquake as recorded in Yuzhno Sakhalinsk station, in Russia. The range of frequencies considered depends on the signal-to-noise ratio of the spectra. For the particular station, the filter is chosen between 0.01 and 2 Hz.

```

1 qdp off
2 r *SAC
3 interpolate delta 0.2
4 trans from polezero subtype pzs to vel
5 int
6 rmean
7 rtrend
8 taper type cosine width 0.1
9 bp c 0.01 2 p 2 n 4
10 cut a -t1 t2
11 rmean
12 rtr
13 taper type cosine width 0.1
14 cut off
15 fft
16 grid on
17 psp am

```

Fig. 4.2 SAC script for obtaining the amplitude spectra. Line 2 reads the seismogram; line 3 resamples the waveform with a given sampling rate (here 0.2s); line 4 removes the instrument response returning the velocity; line 5 integrates the seismogram in velocity to obtain the displacement; lines 6 to 8 remove the mean, the trend and apply a cosine taper on the data; line 9 applies a two-way band pass filter excluding frequencies lower than 0.01 Hz and greater than 2 Hz; line 10 cuts the seismogram t1 s before and t2 s after the P-wave arrival; line 15 calculates the fast Fourier transform; line 17 plots only the amplitude of the spectrum.

4.1.1 January 8, 2006 $M_w=6.6$ Kythera earthquake

Spectral analysis of the P-waveforms of 10 stations was carried out, for the January 8, 2006 Kythera earthquake, depicted in Fig. 4.3. Table 4.1 shows stations parameters, such as the distance, the azimuth, the Omega, the corner frequency and the scalar moment.

Table 4.1 Station parameters (distance and azimuth in degrees) and spectra parameters (Omega- Ω_0 in meters, corner frequency f_c in Hz and scalar moment M_0 in Nm) obtained from the far field displacement spectra of the P-waves for the January 8, $M_w=6.6$ Kythera earthquake.

| STATION | Distance (km) | Azimuth (°) | Ω_0 (m*s) | f_c (Hz) | M_0 (Nm * 10^{19}) |
|---------------|---------------|-------------|------------------|------------|-------------------------|
| YSS | 8967 | 37 | 5.70E-05 | 0.10 | 0.904 |
| HIA | 7455 | 44 | 7.00E-05 | 0.11 | 0.794 |
| ULN | 6687 | 50 | 6.60E-05 | 0.08 | 0.629 |
| SDV | 9763 | 80 | 2.00E-05 | 0.15 | 0.961 |
| CHTO | 7521 | 82 | 6.50E-05 | 0.09 | 0.570 |
| FURI | 3418 | 149 | 1.00E-04 | 0.11 | 0.899 |
| TSUM | 6193 | 187 | 3.00E-05 | 0.10 | 0.647 |
| RCBR | 7750 | 246 | 4.00E-05 | 0.10 | 0.813 |
| SJG | 8778 | 285 | 4.00E-05 | 0.09 | 1.024 |
| WVT | 9267 | 311 | 6.00E-05 | 0.09 | 0.941 |
| FFC | 8624 | 332 | 5.00E-05 | 0.09 | 0.901 |
| Average value | | | | | 0.804 |
| M | | | | | 6.6 |

The mean value of the scalar moment was determined using equation (2.14) equal to $M_0=0.804 \cdot 10^{19}$ Nm, in agreement with the equivalent value obtained by waveform inversion ($M_0=0.810 \cdot 10^{19}$ Nm, see Table 3.2). The values of the fault length and average displacement are model dependant, therefore presenting differences. The three circular and the rectangular model parameters are listed in Table 4.2. Brune's circular model obviously overestimates the fault length in comparison with the other model considered. Following equations $\Delta\sigma = \frac{7}{16} \frac{M_0}{r^3}$ (2.19) and $\bar{u} = \frac{M_0}{\mu A}$ (2.20), stress drop and average displacement, respectively, are expected to be underestimated due to the larger fault length. The other circular models account for smaller fault length values, resulting in relatively larger stress drop and displacement values. For the rectangular model, the length was considered equal to the width ($L=w$), approaching the fault area determination by Nikolintaga *et al.* (2008). This assumption resulted in a smaller fault length, a large displacement and an average value of stress drop (Table 4.2). In neither case the value of stress drop approximates the stress drop value expected for interplate earthquakes (Kanamori, 1980). Earthquakes in Greece, however, are generally characterized by low stress drop values, from approximately 1 to 30 bars (Kiritzi *et al.*, 1985).

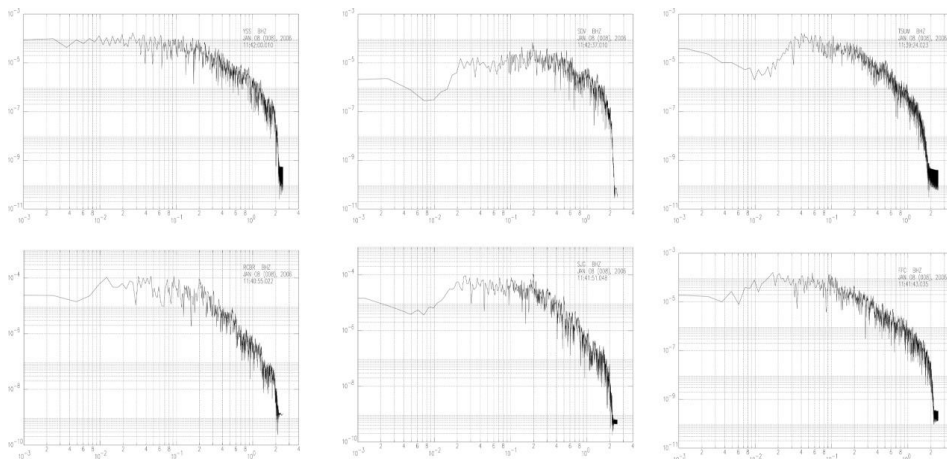


Fig. 4.3 Far-field amplitude displacement spectra used to estimate the fault dimensions and other parameters of the January, 8 2013 $M_w=6.6$ Kythera earthquake. On the horizontal axis the frequency in Hz; on the vertical axis the amplitude in ms. The name and component (all vertical) of each station is noted on the top right side of each spectrum along with the date (year days) and time of recording.

Using the empirical relations of Papazachos *et al.* (2004) for subduction earthquakes, the fault length and average displacement are compared in order to have some insight concerning the values obtained with spectral analysis. Values in Table 4.2 clearly show that for the January 8, 2006 Kythera earthquake, the model that best fits the empirical relations of Papazachos *et al.* (2004) is that of Madariaga's circular model.

Table 4.2 Mean values of fault radius, stress drop in bars, fault length in km, displacement in cm and the equivalent multiplicative factors ($E_{\Delta\sigma}$ for the stress drop, E_L for the fault length and E_u for the average displacement across the fault), for the January 8, $M_w=6.6$ Kythera earthquake.

| Models | Radius (km) | Stress drop (bars) | $E_{\Delta\sigma}$ | Fault length (km) | E_L | Displacement (cm) | E_u |
|-------------------------------------|-------------|--------------------|--------------------|-------------------|-------|-------------------|-------|
| Brune (circular) | 24.5 | 2.4 | 1.07 | 49.0 | 1.01 | 9 | 1.05 |
| Sato & Hirose (circular) | 15.9 | 8.7 | 1.07 | 31.8 | 1.01 | 20 | 1.05 |
| Madariaga (circular) | 11.9 | 21.0 | 1.07 | 23.8 | 1.01 | 36 | 1.05 |
| Rectangular | - | 11.9 | 1.07 | 18.0 | 1.01 | 50 | 1.05 |
| Papazachos et al., 2004 | - | - | - | 26.5 | - | 44 | - |

4.1.2 October 12, 2013 $M_w=6.5$ W Crete earthquake

Further insight is given into the fault parameters of the October 12, 2013 Crete earthquake by determination of the amplitude spectrum of the particular earthquake, as derived by several stations (Fig. 4.4).

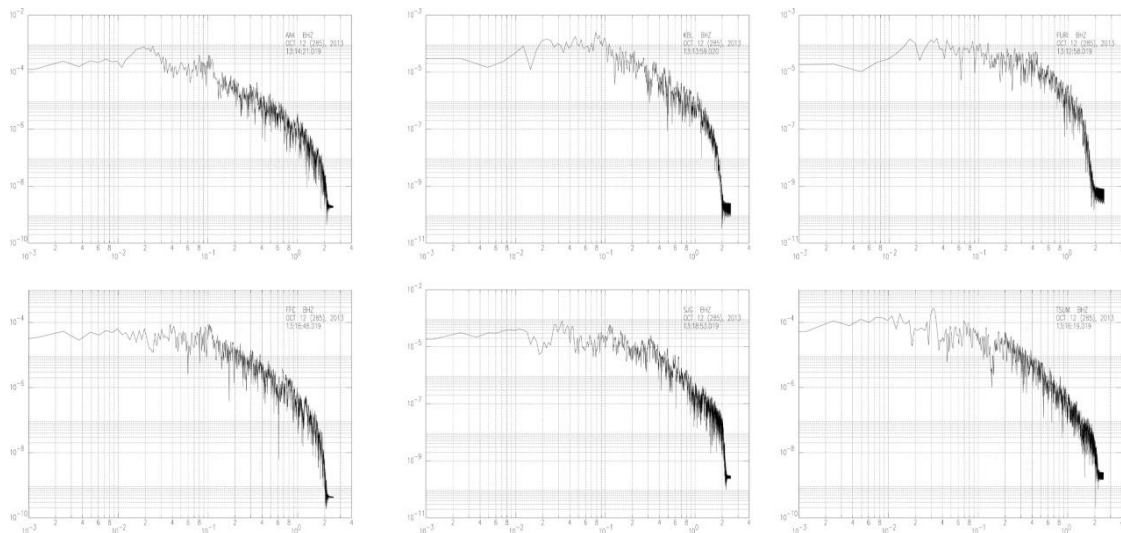


Fig. 4.4 Far-filed amplitude displacement spectra used to estimate the fault dimensions and other parameters of the October 12, 2013 $M_w=6.5$ W Crete earthquake. On the horizontal axis the frequency is given in Hz; on the vertical axis the amplitude in $m*s$. The name and component (all vertical) of each station is noted on the top right side of each spectrum along with the date (year days) and time of recording.

The scalar moment was deduced for every station, using equation (2.14) and the mean value was found equal to $M_0=0.623*10^{19}$ Nm (see Table 4.3), in agreement with the equivalent value obtained by waveform inversion ($M_0=0.605*10^{19}$ Nm, see Table 3.6).

Table 4.3 Station parameters (distance and azimuth in degrees) and spectra parameters (Ω_0 in meters, corner frequency f_c in Hz and scalar moment M_0 in Nm) obtained from the far field displacement spectra of the P-waves for the October 12, $M_W=6.5$ W Crete earthquake.

| STATION | Distance (km) | Azimuth (°) | Ω_0 (m*s) | f_c (Hz) | M_0 (Nm *10 ¹⁹) |
|---------------|---------------|-------------|------------------|------------|-------------------------------|
| YAK | 7344 | 29.47 | 7.00E-05 | 0.09 | 0.947 |
| AAK | 4421 | 63.68 | 9.00E-05 | 0.09 | 0.733 |
| HIA | 7516 | 44.5 | 5.00E-05 | 0.08 | 0.692 |
| KBL | 4129 | 77.78 | 8.00E-05 | 0.11 | 0.608 |
| FURI | 3345 | 148.41 | 6.50E-05 | 0.14 | 0.401 |
| LBTB | 6729 | 177.56 | 5.00E-05 | 0.12 | 0.619 |
| FFC | 8697 | 331.2 | 4.50E-05 | 0.10 | 0.721 |
| SJG | 8792 | 284.58 | 3.00E-05 | 0.11 | 0.486 |
| MACI | 3811 | 269.18 | 7.00E-05 | 0.08 | 0.491 |
| TSUM | 6108 | 186.54 | 5.50E-05 | 0.11 | 0.619 |
| SHEL | 6483 | 313.2 | 6.00E-05 | 0.12 | 0.716 |
| Average value | | | | | 0.623 |
| M | | | | | 6.5 |

Table 4.4 presents the average values and the multiplicative factor of stress drop, fault length and average displacement for different circular models and a rectangular one, considering $L=2w$ aspect ratio, for the October 12, 2013 $M_W=6.5$ W Crete earthquake. Brune's circular model also overestimates the fault length resulting in low stress drop and average displacement values. The rectangular model displays larger average displacement, Sato and Hirose's model provided a small value of this parameter, whereas the fault length is similar to both models. In this case Madariaga's model also seems to be the most comparable to the empirical relations for the Hellenic region. Finally, stress drop exhibits variance, always though having lower values in comparison to interplate events (Kanamori, 1980), in accordance with the ones expected for earthquakes in Greece (Kiritzi *et al.*, 1985).

Table 4.4 Mean values of fault radius, stress drop in bars, fault length in km, displacement in cm and the equivalent multiplicative factors ($E_{\Delta\sigma}$ for the stress drop, E_L for the fault length and E_u for the average displacement across the fault), for the October 12, $M_W=6.5$ W Crete earthquake.

| Circular model | Radius (km) | Stress drop (bars) | $E_{\Delta\sigma}$ | Fault length (km) | E_L | Displacement (cm) | E_u |
|---------------------------------|-------------|--------------------|--------------------|-------------------|-------|-------------------|-------|
| Brune (circular) | 24.7 | 2.0 | 1.10 | 49.4 | 1.24 | 7 | 1.04 |
| Sato & Hirose (circular) | 15.3 | 7.5 | 1.10 | 30.6 | 1.24 | 17 | 1.04 |
| Madariaga (circular) | 11.5 | 18.0 | 1.10 | 23.0 | 1.24 | 30 | 1.04 |
| Rectangular | - | 14.4 | 1.10 | 24.5 | 1.24 | 50 | 1.04 |
| Papazachos <i>et al.</i> , 2004 | - | - | - | 24.2 | - | 40 | - |

CHAPTER 5: DISCUSSION – CONCLUSIONS

5.1 Discussion

During the elaboration of this study, several methods were employed for the determination of earthquake sources in the western Hellenic Arc (i.e. P-wave polarities, bodywave inversion and spectral analysis). Application of these methods provided results that were mainly expected according to the observed seismotectonic framework of the under study area.

However, some difficulties as well as puzzling results came to light regarding either the inversion process or the interpretation of a focal mechanism. The first setback appeared with the addition of SH-waveforms for the October 12, 2013 $M_W=6.5$ W Crete earthquake. While all P-waveforms were well simulated by the synthetic ones even in cases of stations that are near or on the nodal planes (Fig. 3.51), all synthetic SH-waveforms appeared with opposite polarities. Since inversion of P-waves was carried out successfully and the two nodal planes were well constrained, determined and in accordance with other fault plane solutions, the setback was attributed to poor processing of the raw data. S-wave arrivals were hand-picked and some parameters in the *i_conv.farm* and *response* files (see Appendix A) were manually changed and thus it is possible that one or some of them were poorly determined. Nonetheless, inversion with only P-waveforms can give satisfactory results (Lay *et al.*, 2013), so it can be used to determine the source characteristics.

The other drawback regards the seismotectonic interpretation and the fault plane determination for the strike-slip events studied here. As already mentioned, the western Hellenic Arc is characterized by the subduction of the African lithosphere under the Aegean plate, producing a complicated geological and seismotectonic setting (McKenzie, 1972, 1978; Jackson and McKenzie, 1988; Papazachos *et al.*, 1988; Jackson, 1994; Papazachos and Kiratzi, 1996; McClusky *et al.*, 2000; Kiratzi and Louvari, 2003). Thrust fault interface earthquakes are found at shallow depths (30-60 km). This known seismotectonic regime emerges in the present study with the existence of the thrust faulting mechanisms of February 14, 2008 and October 12, 2013 earthquakes. Moreover, intermediate depth strike-slip earthquakes with thrust component occur along the Wadatti-Benioff zone at depths between 60 and 170 km (Papazachos and Comninakis, 1969; LePichon and Angelier, 1979; Papazachos *et al.*, 1998; Yolsal and Taymaz, 2012; Skarlatoudis *et al.*, 2013), along the subducting slab. They exhibit down-dip extension parallel to the dip of the subducting slab, having ~N-S trending T-axes, indicating the expected slab pull and P-axes parallel to the local strike of the subduction zone at south of Crete. This orientation of the P-axes is connected to the along-strike shortening of the African plate, possibly linked to the great curvature of the Hellenic subduction zone. In the

present study, the aforementioned seismotectonic feature of the Hellenic subduction zone is represented by the January 8, 2006 $M_w=6.6$ Kythera event.

On the other hand, the focal mechanism of the shallow strike-slip events cannot be explained by the aforementioned seismotectonic regime, although the best fitting fault planes have been determined by bodywave inversion (see Chapters 3.2.3 and 3.5.3). A theory proposed by Bohnhoff *et al.* (2005b) suggested that the event of March 17, 2004 could reflect brittle failure along pre-existing faults within the upper crust.

5.2 Summary of the results

The objective of this work was to investigate the seismic sources of the western Hellenic Arc. The criteria imposed for this study were the large magnitude and the recent period of origin of the earthquakes generated. The purpose of these criteria was to ensure first of all that many waveforms were available and secondly that the registrations had high signal-to-noise ratio, facilitating the inversion process. Using fault plane solutions obtained by P-wave polarities as a reference, bodywave inversion was carried out, determining finally the focal depth, the source time function, a well-constrained focal mechanism, the magnitude and the scalar moment of each earthquake. Two of the earthquakes were also investigated through spectral analysis of the P-waveforms, in order to give some further insight.

The first event, of March 17, 2004 that struck south of the island of Crete was originated on a strike-slip fault, the focal mechanism of which was first determined with P-wave first motions and then constrained with teleseismic bodywave inversion. The selection of the nodal plane $77^\circ/69^\circ/159^\circ$ was based upon the fact that proper inversion could not be carried out on one of the two nodal planes. With bodywave inversion and assuming a double couple and a triangular source time function composed of six overlapping isosceles triangles with rise time 1s and total rupture time 8s, the focal depth, magnitude and scalar moment were calculated, $h=33$ km, $M_w=6.0$ and $M_0=0.102 \cdot 10^{19}$ Nm, respectively (Table 3.1). The results obtained are similar to those of different institutes. The focal depth presents the greatest variance; this study's determination is closer to USGS and Yolsal and Taymaz (2012).

The next event was the January 8, 2006 $M_w=6.6$ Kythera earthquake. Again a double couple was considered and a triangular source time function described by a series of 5 overlapping triangles with 2s rise time and 12s of total duration, in agreement with INGV and similar to HRV (12s and 11s, respectively). The best fitting depth was constrained at 70 km, in accordance to the depths proposed by several institutes and studies (Nikolintaga *et al.*, 2008; Agalos, 2009; Table 3.2), as well as the magnitude ($M_w=6.6$). The scalar moment defined ($M_0=0.868 \cdot 10^{19}$ Nm) more proximate to the one obtained by Yolsal and Taymaz (2012). Finally, considering the

seismotectonic frame of the area (Kiratzis and Papazachos, 1995; Benetatos *et al.*, 2004), the form of the Benioff zone (Papazachos *et al.*, 2000) and the distribution of aftershocks of particular event (Nikolintaga *et al.*, 2008) the fault plane is recognized as the ENE-WSW plane, defined by a strike of 65° , dip 60° and rake 114° . The fault orientation and mechanism vary significantly throughout different publications (51° - 81° for the strike, 42° - 75° for the dip and 102° - 166° for the dip). Spectral analysis of the P-waveform and adoption of Madariaga's circular model revealed low stress drop (21 bars), in accordance to the general stress drop values observed in the broader Aegean and in the Hellenic arc, particularly. The scalar moment obtained with this analysis is in agreement with the value obtained by waveform inversion ($M_0=0.804 \cdot 10^{19}$ Nm) and the average displacement was found $\bar{u} \approx 55$ cm, on a $L \approx 24$ km fault, assuming a length-to-width ratio of 1.

Next, the seismic events of February 2008 were investigated. Table 3.3 summarizes the characteristics of the first strong event which were determined considering a double couple, a triangular source time function of 2s rise time, consisting of 6 overlapping triangles, corresponding to 18s of total rupture time. These considerations resulted in a depth of 30 km, within the range proposed by other sources, magnitude $M_w=6.6$ and scalar moment $M_0=1.07 \cdot 10^{19}$ Nm. The low-dipping plane was recognized as the fault plane, in agreement with the seismotectonic regime expected to prevail in subduction zones (Papazachos *et al.*, 1998; Sokos *et al.*, 2008; Roumelioti *et al.*, 2009). The strike of the fault is NNW-SSE with an angle of 12° and pure thrust component ($\lambda=102^\circ$). The fault plane solution obtained is similar to that of other institutes, whereas the scalar moment has the second lowest value, after that determined by NOA, not being though significantly lower.

The second largest earthquake of February, 2008 struck only two hours after the first event. It was also studied considering a double couple of forces acting on a point source and a triangular source time function. The overlapping triangles composing it were 4, the rises time 1s and the total rupture duration 7 s. Table 3.4 shows the values obtained for each parameter of the earthquake. The focal depth was determined at 32 km, being closer to the depths calculated by Roumelioti *et al.*, 2004 and AÜT (33 km and 34 km, respectively). The corresponding fault was the low-dipping ($\delta=15^\circ$) NW-SE nodal plane, in accordance with other institutes' plane solutions, such as Roumelioti *et al.* (2009) and USGS and same mechanism as the first event. Finally, the magnitude determined was the smaller compared to the other solutions ($M_w=6.0$) and closer to the results provided by NOA and Roumelioti *et al.* (2009). So was the scalar moment ($M_0=0.14 \cdot 10^{19}$ Nm), but with very close to almost all proposed solutions, except for INGV.

The last strong event of February 2008 occurred 6 days later and was the smallest in terms of magnitude ($M_w=5.9$) and scalar moment ($M_0=0.10 \cdot 10^{19}$ Nm) studied here, but close to the values obtained by AUTH, NOA, Roumelioti *et al.* (2009) and USGS. A double couple and a triangular source time function with 5 triangles of 1s rise time and 8s of total rupture duration were considered, in agreement with the duration proposed by gCMT and Roumelioti *et al.* (2009). The focal depth was determined at 11 km, closer to the focal depths determined by AUTH, USGS and Roumelioti *et al.* (2009), as shown in Table 3.5. The fault plane was constrained according to the nodal plane that demonstrated the least rms error and best fitting synthetic waveforms compared to the observed ones, during the inversion. This was the NNW-SSE nearly vertical ($\delta=83^\circ$) plane.

Finally, the last and most recent earthquake was the October 12, 2013 $M_w=6.5$ earthquake that struck west of the Island of Crete. A double couple and a triangular source time function were here too considered. The rise time was determined at 1.5s for each of the 6 triangles. The total duration of the source time function was 12s, closest to the Harvard and INGV solution (Table 3.6). The depth, which in this study was determined at 49 km, shows great variance between 10 km and 49 km (the depth of INGV is fixed and therefore not considered as a well- constrained solution). The magnitude of the earthquake also exhibits a great range of values (from $M_w=6.2$ for CCPT to $M_w=6.8$ for Harvard) and along with it, the scalar moment (from $M_0=0.23 \cdot 10^{19}$ Nm to $M_0=1.44 \cdot 10^{19}$ Nm for the same institutes). In this study these values are determined equal to $M_w=6.5$ and $M_0=0.604 \cdot 10^{19}$, respectively. Ultimately, the fault was recognized as the low-dipping ($\delta=12^\circ$) nodal plane striking NW-SE, in accordance with fault plane orientations expected along subduction zones (Papazachos *et al.*, 1998; Sokos *et al.*, 2008; Roumelioti *et al.*, 2009). As the aforementioned parameters, the fault plane solution has significant variance. Thus, the strike ranges from 205° (KAN) to 353° (AZUR), the dip from 3° (HRV) to 56° (KAN) and the rake from 44° (GFZ) to 171° (CCPT) and to -168° (NOA). This study's focal mechanism is closer to the one determined by USGS (Table 3.6). Spectral analysis of P-waveforms and selection of Madariaga's circular model revealed low stress drop (18 bars), scalar moment value similar to the one previously obtained ($M_0=0.623 \cdot 10^{19}$ Nm) and an average displacement $\bar{u} \approx 46$ cm on a $L \approx 23$ km fault, assuming length to width ratio equal to 2.

Summing up, this M.Sc. Thesis investigated the source characteristics of strong earthquakes of the past decade in the western Hellenic arc, using P-wave polarities, teleseismic bodywave inversion and, selectively, spectral analysis. The majority of the results obtained were expected, given the well-defined subduction zone that characterizes the western Hellenic arc and hence could easily be explained by the existing seismotectonic regime of the area. However, two of the sources studied could not be explained by the established stress distribution. An effort was made to

give a possible direction for further investigation. It lays in future studies to elucidate the complexity of the Hellenic subduction zone.

REFERENCES

- Agalos, A., 2009. Determination of seismic parameters with the method of seismic moment tensor inversion, PhD Thesis (in Greek), 317p.
- Aki, K., 1966. Generation and propagation of G waves from the Niigata earthquake of June 16, 1964, 2, Estimation of earthquake moment, released energy, and stress-strain drop from G wave spectrum, *Bull. Earthquake Res. Inst., Tokyo Univ.*, 44, 73-88.
- Aki, K. and Richards, P. G., 1980. *Quantitative Seismology, Theory and Methods*, Vol. I and II, W.H. Freeman, San Francisco.
- Ambraseys N.N., Bommer J.J., 1990. Uniform magnitude re-evaluation for the strong-motion database of Europe and adjacent areas, *European Earthquake Engineering*, Vol: IV, Pages: 3-16
- Anderson, H., and Jackson J. A., 1987. Active tectonics of the Adriatic Region, *Geophys. J. R. Astr. Soc.*, 91, 937-983.
- Archuleta, R. J., Cranswick, E., Mueller, C and Spudich, P., 1982. Source parameters of the 1980 Mammoth Lakes, California, earthquake sequence, *J. Geophys. Res.*, 87, 4595-4607.
- Barker. J. S. and Langston, C. A., 1981. Inversion of teleseismic body waves for the moment tensor of the 1978 Thessaloniki, Greece, earthquake, *Bull. Seis. Soc. Am.*, 71, 1423-1444.
- Barker. J. S. and Langston, C. A., 1983. A teleseismic body-wave analysis of the May 1980 Mammoth Lakes, California earthquakes, *Bull. Seis. Soc. Am.*, 73, 419-434.
- Benetatos, C., Kiratzi, A., Papazachos, C. and Karakaisis, G., 2004. Focal mechanisms of shallow and intermediate depth earthquakes along the Hellenic Trench, *J. Geodyn.*, 37, 253-296.
- Bohnhoff, M., Makris, J., Papanikolaou, D. and Stavrakakis, G., 2001. Crustal investigation of the Hellenic subduction zone using wide aperture seismic data, *Tectonophysics*, 343 239-262.
- Bohnhoff, M, Harjes, H.-P. and Meier, T., 2005b. Deformation and stress regimes in the forearc of the Hellenic subduction zone from inversion of focal mechanisms, *J. Seismology*
- Boore D.M., Skarlatoudis A.A., Margaris, B.N., Papazachos, C.B., Ventouzi, C., 2009. Along-Arc and Back-Arc attenuation, Site Response and Source Spectrum for the Intermediate-Depth 8 January 2006 M 6.7 Kythera, Greece, Earthquake, *Bull. Seism. Soc. Am.*, 99, 2410-2434, doi:10.1785/0120080229.

- Brink, U.T. and Lin, J., 2004. Stress interaction between subduction earthquakes and forearc strike-slip faults: modelling and application to the northern Caribbean plate boundary, *J. Geophys. Res.*, 109. doi:10.1029/2004JB003031.
- Brune, J. N., 1970. Tectonic stress and spectra of seismic shear waves from earthquakes, *J. Geophys. Res.*, 75, 4997-5009.
- Brune, J. N., 1971. Correction, *J. Geophys. Res.*, 76, 5002.
- Bufo, E., Udias, A. and Mezcua, J., 1988. Seismicity and focal mechanisms in south Spain, *Bull. Seism. Soc. Am.*, 78, 2008-2024.
- Bufo, E., Udias, A. and Madariaga, R., 1991. Intermediate and deep earthquakes in Spain, *P. Appl. Geoph.* 136, 375-393.
- Bufo, E., Coca, P., Udias, A. And Lasa, C., 1997. Source mechanism of intermediate and deep earthquakes in southern Spain, *J. Seism.*, 1, 113-130.
- Delibasis, N., 1968. Focal mechanism of intermediate earthquakes and their correlation with intensities, PhD Thesis, Athens University (in Greek).
- DeMets, C., Gordon, R., Argus, D. and Stein, C., 1990. Current plate motions, *Geophys. J. Int.*, 101, 425-478.
- Deschamps, A., H. Lyon-Caen et R. Madariaga, Mise au point sur les méthodes de calcul de sismogrammes synthétiques de longue période. *Ann. Geophys.*, 36, 167-178, 1980.
- Dewey, J. F., 1988. Extensional collapse of Orogens, *Tectonics*, 7, 1123-1139.
- Estabrook, C., 1999. Body wave inversion of the 1970 and 1963 South American large deep-focus earthquakes. *J. Geophys. Res.*, 104: doi: 10.1029/1999JB900244. issn: 0148-0227.
- Futterman, W.I., 1962. Dispersive body waves, *J. Geophys. Res.*, 67, 5279-5291.
- Goldstein, P., Dodge, D., Firpo, M., Minner, Lee, 2003. "SAC2000: Signal processing and analysis tools for seismologists and engineers, Invited contribution to "The IASPEI International Handbook of Earthquake and Engineering Seismology", Edited by WHK Lee, H. Kanamori, P.C. Jennings, and C. Kisslinger, Academic Press, London.
- Goldstein, P., Snoke, A., 2005. "SAC Availability for the IRIS Community", Incorporated Institutions for Seismology Data Management Center Electronic Newsletter. <http://ds.iris.edu/ds/newsletter/vol7/no1/sac-availability-for-the-iris-community/>
- Grimison, N. and Cheng, W., 1986. The Azores-Gibraltar plate boundary: focal mechanism, depths of earthquakes and the tectonic implications, *J. Geophys. Res.*, 91, 2029-2047.
- Hanks T. C. and Kanamori, H., 1979. A moment magnitude scale, *J. Geophys. Res.*, 84, 2348-2350.

- Hanks, T C. and McGuire, . K., 1981. The character of high frequency strong ground motion, Bull. Seism. Soc Am., 71, 2071-2095.
- Hanks, T. C. and Wyss, M., 1972. The use of body-wave spectra in the determination of seismic-source parameters, Bull. Seism. Soc. Am., 62, 561-589.
- Haskell, N. A., 1964. Total energy and energy spectral density of elastic wave radiation from propagating faults, Bull. Seism. Soc. Am., 54, 1811-1841.
- Hatzfeld, D. and Frogneux, M., 1978. Intermediate deep seismicity in the western Mediterranean unrelated to subduction of oceanic lithosphere, Nature 292, 443-445.
- Hatzfeld, D., Pedotti, G., Hatzidimitriou, P., Panagiotopoulos, D., Scordilis, M., Drakopoulos, I., Makropoulos, K., Delibasis, N., Latousakis, I., Baskoutas, J. & Frogneux, M., 1989. The Hellenic subduction beneath the Peloponnesus: first results of a microearthquake study, Earth planet. Sci. Lett., 93, 283-291.
- Hatzidimitriou, P. M., Scordilis, E. M., Papadimitriou, E. E., Hatzfeld, D., Christodoulou, A. A., 1991. Microearthquake study of the Thessaloniki area (northern Greece). Terra Nova, 3, 648-654.
- Hodgson J., and Cock, J., 1956. Direction of faulting in the Greek earthquakes of August 9-13, 1953, Publ. Dom. Obs., 18, 149-167.
- Ioannidou, E., 1989. Characteristic parameters of seismic source by the method of body wave inversion: Greece and the surrounding area. Ph. D. Thesis, Athens University, 282pp.
- ITSAK, Institute of Engineering Seismology and Earthquake Engineering, 2008. The earthquake of Koroni, Scientific Report, <http://www.itsak.gr/documents/Report?Koroni-2008.pdf>, in Greek.
- Jackson, J. A., 1994. Active tectonics of the Aegean region. Annu. Rev. Earth Planet. Sci. 22, 239-271.
- Jackson, J. A. & McKenzie, D., 1988. The relationship between plate motions and seismic moment tensors, and the rates of active déformation in the Mediterranean and the Middle East, Geophys. J., 93, 45-73.
- Jeffreys, H. and Bullen, K. E. 1940. "Seismological Tables." British Association for the Advancement of Science, London
- Karakaisis, G.F., Papazachos, C.B. and Skordillis, E.M., 2010. Seismic sources and main seismic faults in the Aegean and surrounding area, Bull. Geol. Teor. Aplic., 48, 371-383.
- Karakostas, V.G., Papadimitriou, E.E., Karakaisis, G.F., Papazachos, C.B., Scordilis, E.M., Vargemezis, G. and Aidona, E., 2003. The 2001 Skyros, Northern Aegean, Greece, earthquake sequence: off - fault aftershocks, tectonic implications, and seismicity

- triggering. *Geophysical Research Letters* 30: doi: 10.1029/2002GL015814. issn: 0094-8276.
- Karakostas, C., Makarios, T., Lekidis, V., Salonikios, T., Sous, S., Makra, K., Anastasiadis, A., Klimis, N., Dimitriou, P., Margaritis, B., Papaioannou, C., Theodulidis, N. and Savvaidis, A., 2006. The Kythira earthquake of January 8, 2006: Preliminary report on strong motion data, geotechnical and structural damage, http://www.eeri.org/lfe/pdf/greece_kythira_ITSAK.pdf
- Kastens, K.A., Gilbert, L.E., Hurst, K.J., Veis, G., Paradissis, D., Billiris, H., Schluter, W. and Seeger, H., 1996. GPS evidence for arc-parallel extension along the Hellenic arc, Greece, *Tectonophysics*, submitted.
- Keary, P., Klepeis, K.A., Vine, F.J., 2009. *Global Tectonics*, Third Edition, Wiley-Blackwell.
- Keilis-Borok, V. I., 1959. An estimation of the displacement in an earthquake source and of source dimensions, *Ann. Geofis. (Rome)*, 12, 205-214.
- Kikuchi, M. and Kanamori, H., 1982. Inversion of complex body waves-I, *Bull. Seism. Soc. Am.*, 72, 391-506.
- Kikuchi, M. and Kanamori, H., 1986. Inversion of complex body waves-II, *Phys. Earth and Planet. Int.*, 43, 205-222.
- Kikuchi, M. and Kanamori, H., 1991. Inversion of complex body waves-III, *Bull. Seism. Soc. Am.*, 81, 2335-2350.
- Kikuchi, M., Kanamori, H. and Satake, K., 1993. Source complexity of the 1988 Armenian Earthquake: Evidence for a slow After-Slip Event, *J. Geophys. Res.*, 98, 15797-15808.S
- Kikuchi, M. and Kanamori, H., 2003. Note on teleseismic body-wave inversion program, <http://www.eri.u-tokyo.ac.jp/ETAL/KIKUCHI/>.
- Kiratzi, A. A. and Langston, C. A., 1989. Estimation of earthquake source parameters of the May 4 1972 event of the Hellenic arc by the inversion of waveform data, *Phys. Earth Planet. Int.*, 57, 225-232.
- Kiratzi, A. A., and Langston, C. A., 1991. Moment tensor inversion of the January 17, 1983 Kefallinia event, Ionian islands (Greece), *Geophys. J. Int.*, 105, 529-535.
- Kiratzi, A., and Louvari, E., 2003. Focal mechanisms of shallow earthquakes in the Aegean Sea and the surrounding lands determined by waveform modeling: a new database, *J. Geodyn.*, 36, 251-274.
- Kiratzi, A. A., and Papazachos, C. B., 1995. Active seismic deformation in the southern Aegean Benioff zone, *J. of Geodynamics*, 19, 65-78.

- Kiratzi, A. A., Karakaisis, G. F., Papadimitriou, E. E. and Papazachos, B. C., 1985. Seismic Source-Parameter Relations for Earthquakes in Greece, *Pure Appl. Geophys.*, 123, 27-41.
- Kiratzi, A. A., Papadimitriou, E. E., and Papazachos B. C., 1987. A microearthquake survey in the Steno dam site in northwestern Greece, *Annales Geophysicae*, 5, 529-535.
- Kiratzi, A., Wagner, G., and Langston, C., 1991. Source parameters of some large earthquakes in Northern Aegean determined by body waveform modeling, *Pure Appl. Geophys.*, 105, 515-527.
- Konstantinou, K.I and Melis, N.S., 2006. High frequency shear-wave propagation across the Hellenic subduction zone, *Bull. Seismol. Soc. Am.*, 98, 797-803.
- Koyama, J., 1997. The complex of faulting process of earthquakes, Kluwer Academic Publishers.
- Lay, T., Lingling, Y., Kanamori, H., Yamazaki, Y., Cheung, K.F., Ammon Ch.J., 2013. The February 6, 2013 M_w 8.0 Santa Cruz Islands earthquake and tsunami, 2013. *Tectonophysics*, 608, 1109-1121.
- LePichon, X., and Angelier, J., 1979. The Hellenic Arc and Trench system: a key to the neotectonic evolution of eastern Mediterranean area. *Tectonophysics*, 60, 1-42.
- LePichon, X. and Angelier, J., 1981. The Aegean Sea, *Phil. Trans. R. Soc. Lond.* 300, 357-372.
- Lowrie, W., 2007. *Fundamentals of Geophysics*, Second Edition, Cambridge University Press, ISBN: 1139465953, 9781139465953.
- Madariaga, R., 1983. High frequency radiation from dynamic earthquake fault models. *Ann. Geophys.*, 1, 17-23.
- Madariaga, R., 1976. Dynamics of an expanding circular fault. *Bull. Seism. Soc. Am.*, 66, 639-666.
- Main, I.G. & P.W. Burton (1990). Moment-magnitude scaling in the Aegean area, *Tectonophysics* 179, 273-285.
- Margaris, V. and Papazachos, C. B. , 1999. Moment-magnitude relations based on strong motion records in Greece and surrounding area, *Bull. Seism. Soc. Am.*, 89, 442-455.
- McClusky, S., Balassanian, S., Barka, A., Demir, C., Ergintav, S., Georgiev, J., Gurkan, O., Hamburger, M., Hurst, K., Kahle, H., Kastens, K., Kekelidze, G., King, R., Kotzev, V., Lenk, O., Mahmoud, S., Mishin, A., Nadariya, M., Ouzounis, A., Paradissis, D., Peter, Y., Prilepin, M., Reilinger, R., Sanli, I., Seeger, H., Tealeb, A., Tosksöz, N. M., and Veis, G., 2000. Global Positioning System constraints on plate kinematics and dynamics in the eastern Mediterranean and Caucasus, *J. Geophys. Res.*, 105, 5695-5719.

- McKenzie, D. P., 1970. The plate tectonics of the Mediterranean region, *Nature* 226, 239-243.
- McKenzie, D. P., 1972. Active tectonics of the Mediterranean region. *Geophys. J. astron. Soc.*, 30, 109-185
- McKenzie, D. P., 1978. Active tectonics of the Alpine-Himalayan belt: the Aegean Sea and surrounding regions, *Geophys. J. R. astr. Soc.*, 55, 217-254.
- Morales, J., Serrano, I., Jabaloy, A., Galindo-Zaldivar, J., Zhao, D., Torcal, F., Vidal, F. And Gonzales-Lodeiro, F., 1999. Active continental subduction beneath the Betic Cordillera and the Alboran Sea, *Geology*, 27, 735-738.
- Nábelek, J., 1984. Determination of Earthquake Source Parameters from Inversion of Body Waves. PhD Thesis, Mass. Inst. of Tech.
- Nikolintaga, I., Karakostas V., Papadimitriou E. and Vallianatos, F., 2007: Velocity models inferred from P-waves travel time curves in South Aegean, *Bull. Geol. Soc. Greece*, XXXX, 1187-1198.
- Nikolintaga, I., Karakosta, V., Papadimitriou, E. and Vallianatos, F., 2008. The 2006 Kythera (Greece), $M_w=6.7$ slab-pull event: tectonic implications and the geometry of the Hellenic Wadati-benioff zone, *Ann. Geophys.*, 51, 823-837.
- Panagiotopoulos, D. G., Papazachos, B. C., 1985. Travel times of Pn-waves in the Aegean and surrounding area. *Geophys. J. R. Astr. Soc.* 80, 165-176.
- Papadimitriou, E. E., 1993. Focal mechanism along the convex side the Hellenic arc, *Boll Geofis. Teor. Appl* XXXV, 401-426.
- Papadimitriou, P., 1988. Étude de la structure du manteau supérieur de l'Europe et modélisation des ondes de volume engendrées par des séismes Égéens, *These de Doctorat de l' Université Paris VII*, 211pp.
- Papazachos, B. C., 1961. A contribution to the research on fault plane solutions of earthquakes in Greece, PhD Thesis, University of Athens, 75pp.
- Papazachos B.C., 1989. Measures of the earthquake size in the area of Greece, 1st Scientific Congress of the Hellenic Geophysical Union, Athens, April 1989, 437-447.
- Papazachos, B. C., 1990. Seismicity of the Aegean and Surrounding Area, *Tectonophysics* 178, 287-308.
- Papazachos, B. C., and Comninakis, P. E., 1969. Geophysical features of the Greek island arc and eastern Mediterranean ridge, *C. R. Séances de la Conference Réunion a Madrid*, 16, 74-75.

- Papazachos B. C. and Comninakis, P.E., 1970. Geophysical features of the Greek island arc and eastern Mediterranean ridge, Com. Ren. Des Sceances de la Conference Réunion a Madrid, 1969, 16, 74-75.
- Papazachos, B. C. and Comninakis, P. E., 1971. Geophysical and tectonic features of the Aegean arc. J. Geophys. Res., 76, 8517-8533.
- Papazachos, B. C., and Delibasis, N. D., 1969. Tectonic stress field and seismic faulting in the area of Greece, Tectonophysics, 7, 231-255.
- Papazachos, B. C., Kiratzi, A. A., Hatzidimitriou, P. M., and Rocca A. Ch., 1984. Seismic faults in the Aegean area. Tectonophysics, 106, 71-85.
- Papazachos, B. C., Kiratzi, A. A., Karakostas, B., Panagiotopoulos, D., Scordilis, E. & Mountrakis, D. M., 1988. Surface fault traces, fault plane solution and spatial distribution of the aftershocks of September 13, 1986 earthquake of Kalamata (Southern Greece), Pure appl. Geophys., 126, 55-68.
- Papazachos, B., Kiratzi, A. and Papadimitriou, E., 1991. Regional focal mechanisms for earthquakes in the Aegean area, Pure Appl. Geophys., 136, 407-420.
- Papazachos, B. C., Kiratzi, A. A. And Karakostas, B. G., 1997. Toward a homogeneous moment magnitude determination in Greece and surrounding area, Bull. Seism. Soc. Am., 87, 474-483.
- Papazachos, B. C., Papadimitriou, E. E., Kiratzi, A. A., Papazachos C. B. and Louvari, E. K., 1998. Fault plane solutions in the Aegean Sea and the surrounding area and their tectonic implications, Boll. Geof. Teor. Appl., 39, 199-218.
- Papazachos B.C., Karakostas, B.G., Papazachos C.B. and Scordilis E.M., 2000. The geometry of the Wadati-Benioff zone and lithospheric kinematics in the Hellenic arc, Tectonophysics 319, 275-300.
- Papazachos, B. C., Mountrakis, D. M., Papazachos, C. B., Tranos, M. D., Karakaisis, G. F., and Savaidis, A. S., 2001. The faults that caused the known string earthquakes in Greece and surrounding areas during 5th century B.C. up to present, 2nd Conf. Earthq. Engin. And Engin. Seism., 28-30 September 2001, Thessaloniki, I, 17-26.
- Παπαζάχος, Β.Κ., Καρακώστας, Β.Κ., Κυρατζή, Α.Α, Μάργαρης, Β.Ν, Παπαζάχος, Κ.Β. και Σκορδύλης, Ε.Μ., 2001. Η καταλληλότητα των κλιμάκων μεγέθους που χρησιμοποιούνται στον καθορισμό σχέσεων υπολογισμού των παραμέτρων της ισχυρής σεισμικής κίνησης στην Ελλάδα, 2 ο Παν. Συν. Αντισεισμικής Μηχανικής & Τεχνικής Σεισμολογίας, Τ.Ε.Ε., Θεσσαλονίκη, 28-30 Σεπτεμβρίου 2001, 1, 55-64.

- Papazachos, B. C., Karakostas, V. G., Kiratzi, A. A., Margaris, B. N., Papazachos, C. B. and Scordilis, E. M., 2002. Uncertainties in the estimation of earthquake magnitudes in Greece, *Journal of Seismology*, 6, 557-570.
- Papazachos, B. C., Scordilis, E. M., Panagiotopoulos, D. G., Papazachos, C. B. and Karakaisis, G. F., 2004. Global relations between seismic fault parameters and moment magnitude of earthquakes, *Bull. Geol. Soc. Greece* vol XXXVI, Proceedings of the 10th International Congress, Thessaloniki, April 2004, 1482-1489.
- Papazachos, C. B. and Kiratzi, A. A., 1996. A detailed study of the active crustal deformation in the Aegean and the surrounding area, *Tectonophysics*, 253, 129-153.
- Papazachos, C. B. and Kiratzi, A.A., 1992. A formulation for reliable estimation of active crustal deformation and its application to central Greece, *Geophysical Journal International*, 111, 424 - 432.
- Papazachos, C. B. and Nolet, G., 1997. P and S deep velocity structure of the Hellenic area obtained by robust nonlinear inversion of travel times, *J. Geophys. Res.*, 102, 8349-8367.
- Ritsema, A. R., 1974. Mechanism of the Balkan region, *R. Netherl. Meteorol. Inst. Sci. Rep.*, 74, 36 pp.
- Roumelioti, Z., Benetatos, Ch. And Kiratzi, A., 2009. The 14 February 2008 earthquake (M6.7) sequence offshore south Pelopones (Greece): Source models of the three strongest events. *Tectonophysics*, 471, 3-4, 272-284.
- Sato, T. and Hirose, T., 1973. Body wave spectra from propagating shear cracks, *J. Phys. Earth.*, 21, 415-431.
- Scholz, C., 1990. *The Mechanics of Earthquakes and Faulting*, Cambridge Univ. Press, Cambridge, U. K.
- Scordilis, E. M., Karakaisis, G. F., Karakostas, B. G., Panagiotopoulos, D. G., Comninakis, P. E. and Papazachos, B. C., 1985. Evidence of transform faulting in the Ionian Sea. The Cephalonia island earthquake sequence of 1983, *Pure Appl. Geophys.*, 123, 388-397.
- Shomali, H.Z. and Slunga, R., 2000. Body wave moment tensor inversion of local earthquakes: an application to the South Iceland Seismic Zone. *Geophys. J. Int.*, 140, 63-70.
- Skarlatoudis, A.A., Papazachos C.B., Margaria B.N., Papaioannou, Ch., Ventouzi, Ch., Vamvakaris, D., Bruestle, A., Meier, T., Friedrich, W., Stravrakakis, G., Taymaz, T., Kind, R., Vafidis, A., Dahm, T. and the ENGELADOS groups, 2009. Combination of strong-and weak-motion recording for attenuation studies: The case of the January 8, 2006 Kythera intermediate-depth earthquake, *Bull. Seismol. Soc. Am.*, 99, 694-704.

- Skarlatoudis, A. A., Papazachos, C. B., Margaris, B. N., Ventouzi, C, Kalogeras, I. And the EGELADOS group, 2013. Ground-motion Prediction Equations of the Intermediate-Depth Earthquakes in the Hellenic Arc, Southern Aegean Subduction Area, Bull. Seism. Soc. Am., 103, 1952-1968.
- Sokos E., Serpetsidaki, A., Zahradnik, J., Tselentis, G.A., 2008. Quick assessment of the fault plane, for the recent event in Southern Greece (14 February 2008, M6.9). Scientific Reort, European Mediterranean Seismological Centre, (http://www.emsc-csem.org/current/evt/14_Feb_event_Sokos_et_al.pdf, last assessed on October 20, 2008).
- Soufleris C. and Stewart, G.S., 1981. A source study of the Thessaloniki (northern Greece) 1978 earthquake sequence, Geophys. J. R. astr. Soc., 67, 343-358.
- Stein, S. and Wysession, M., 2003. An introduction to seismology, earthquakes and earth structure, Blackwell Publishing, Oxford, 498 pp.
- Taymaz, T., Jackson, J., and Westaway, R., 1990. Earthquake Mechanisms in the Hellenic Trench Near Crete, Geophys. J. Int. 102, 695-731.
- Taymaz, T., Jackson, J. and McKenzie, D., 1991. Active tectonics of the north and Central Aegean Sea, Geophys. J. Int., 106, 433-490.
- Taymaz, T., Yılmaz, Y. and Dilek, Y. 2007. The Geodynamics of the Aegean and Anatolia: Introduction. In: The Geodynamics of the Aegean and Anatolia (eds. Tuncay Taymaz, Yücel Yılmaz & Yıldırım Dilek), pp. 1-16, The Geological Society of London, Special Publications Book, Vol: 291, ISBN: 978-1-86239-239-7.
- Udías, A., 1991. Source mechanism of earthquakes. Adv. Geophys., 33, 81-140.
- Udías, A., 1999. Principles of Seismology, Cambridge University Press, 475 pp.
- Udías, A., Brillinger, D., Buforn, E. and Bolt, B.A., 1984. Program MECSTA. In: Documentation of earthquake algorithms. World Data Center Solid Earth. Geophys. Report 28.
- Wessel, P. and Smith, W.H.F., 1998. New improved version of the Generic Mapping Tools released, EOS Transactions AGU 79, 579.
- Widiyantoro, S., van den Hilst, R. D. and Wenzel, F., 2004. Deformation of the Aegean Slab in the Mantle Transition Zone, Int. J. Tomogr. Stat.; D04:1-14.
- Yolsal-Çevikbilen, S. and Taymaz, T., 2012. Earthquake Source Parameters Along the Hellenic Subduction Zone and Numerical Simulations of Historical Tsunamis in the Eastern Mediterranean. Tectonophysics, Vol: 536-537, pp. 61-100. doi:10.1016/j.tecto.2012.02.019.

Zhong, S. and Gurnis, M., 1995. Mantle Convection with Plates and Mobile, Faulted Plate Margins, *Science*, 267, 838-843.

European Mediterranean Seismological Centre, <http://www.emsc-csem.org>

gCMT catalog, <http://www.globalcmt.org>

APPENDIX A: DATA TREATMENT

Introduction

For the application of the inversion program of Kikuchi and Kanamori (2003), three-component (BHZ, BHN and BHE) broadband teleseismic seismograms were retrieved from stations of the Global Seismographic Network (GSN) with Wilber III of the IRIS database (<http://www.iris.edu/wilber3/>).

Data acquisition and preparation

The seismograms were obtained from stations at teleseismic distances between 30° and 90°, to avoid the upper mantle and core triplications (Barker and Langston, 1981). The selection of the seismograms was based on the identification of the P-wave first motion, the high signal-to-noise ratio and the stations geographical distribution.

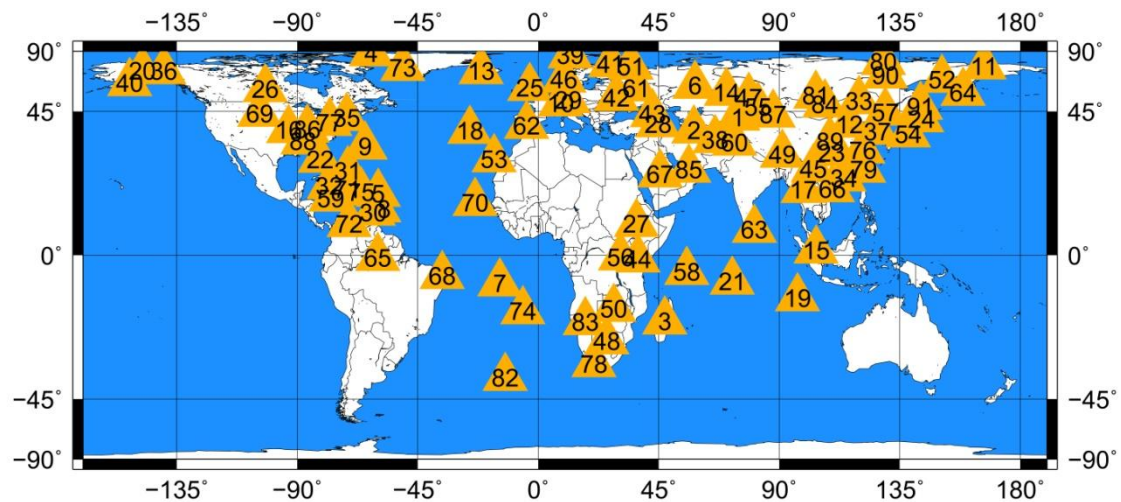


Fig. A.5.1 Map of all the available teleseismic stations. Station names corresponding to the number are listed in Appendix B, long with the network and region of each station.

For seismogram processing, installation of rdseed software (<http://www.iris.edu/>) and the Seismic Analysis Code (Goldstein et al., 2003; Goldstein and Snoko, 2005) was necessary. Using rdseed, the seismograms, primarily in seed format, were converted to sac binary, using the “R” and “d” options. Moreover, two input files manually prepared were required (hypo and sacmacros). The first of these contains information on the hypocenter and the range of epicentral distance of the stations. In the first line of hypo lies the date and time of the event as well as the location of the event (yyyymmddhhmm event-location). In the following line the geographical coordinates, the depth, the time (hh mm ss), the id and the maximum and minimum epicentral distances are stated. The id takes the values 0, 1, 2 and 3 and determines the type of data to be used. In this case, the waveforms represent displacement of the earthquake (id=0, Table A.1).

Table A.1 The manually prepared *hypo* file for the 14/02/2008, $M_w=6.6$ west Hellenic Arc earthquake. The first line stands for the ID of the event. The second line represents the longitude, latitude, depth, origin time (hours, minutes, seconds), type of data (dislocation, velocity, acceleration), minimum and maximum epicentral distances of the stations.

| | | |
|------------|---------|-----------------------|
| 0802141009 | METHONI | GREECE |
| 36.52 | 21.67 | 31.5 10 09 23 0 30 90 |

The next program is the *mk_conv.farm.pl* (written by Y. Yamanaka, July, 2003) which converts the data in SAC format and produces two output files, the response file and the *i_conv.farm*. The response file contains the normalization factor, A_0 , the poles and zeroes and the sensitivity of the seismometer. Resetting the parameters in the *mk_conv.farm.pl* is necessary. The new parameters are $du=80$, $pre_ev=20$, $sample=0.5$, $low_pass_co=1$, $high_pass_co=0.01$, where du is the duration of the seismogram, pre_ev is the duration of the data before the first P and S arrival, $sample$ is the sampling rate, low_pass_co is the cut-off frequency of the low-pass filter and $high_pass_co$ is the cut-off frequency of the high-pass filter (Table A.2). In *i_conv.farm* the station code names and the user-defined values of the parameters in *mk_conv.farm.pl* are listed. Since the seismogram is retrieved in velocity, *mk_conv.farm.pl* executable integrates the seismogram, in order to obtain the displacement.

Table A.2 Parameters set in *mk_conv.farm.pl* program for the data preparation. A bandpass filter is applied between 0.01 Hz and 1 Hz. The duration of the data is set to 80 seconds, 20 of which before the arrival of the first waves. The sampling rate is 0.5 seconds.

| |
|---------------------|
| high_pass_co = 0.01 |
| low_pass_co = 1 |
| du = 80 |
| pre_ev = 20 |
| sample = 0.5 |

The definition of these values is of great importance for the inversion that follows, because they determine the correct time window of the vertical (BHZ) component of the seismogram, containing the first motion of the direct P phase as well as the pP and sP phases. Therefore, the cutting window should be properly selected with caution. Moreover, the entire first S-wave arrival must be included in the same window as the other two components (BHN and BHE). The other two features of this step are the sampling rate of the seismogram, here being 0.5 seconds, and the filter. In this case, a bandpass filter is applied, where all frequencies below 0.01 Hz and above 1 Hz are excluded, in order for the noise to be reduced and the signal to be enhanced.

The next step is to run the *conv.sac.farm* program (written by M. Kikuchi, modified by Y. Yamanaka) with the equivalent input file (*i_conv.farm.pl*) to get the

output file *fort.22*. This program calculates the station parameters, such as the azimuth, the geometrical factor, the epicentral distance, the ray parameter and the filtered seismograms for each station, in the output file *fort.22*. It is of great importance to define firstly the Earth's structure, given as the velocity variation with depth, since the inversion results depend on the depth of the reference point. For this reason, it is important to proceed with the inversion only after having determined a realistic velocity model for the focal region.

The final step of the data preparation for the inversion is running the *rotSH* program, an executable that rotates the coordinates in order to extract the SH component from the NS and EW components of the S-waves in the seismograms. The output file is the *fort.1* file, which includes the observed seismograms and the parameters of the stations and is the input file for the inversion programs. In case only P-waves are used, *rotSH* simply changes the format of *fort.22*. Fig. A.5.2 shows a schematic representation of all the steps followed until the preparation of the final input file for the Kikuchi and Kanamori (1991) bodywave inversion program.

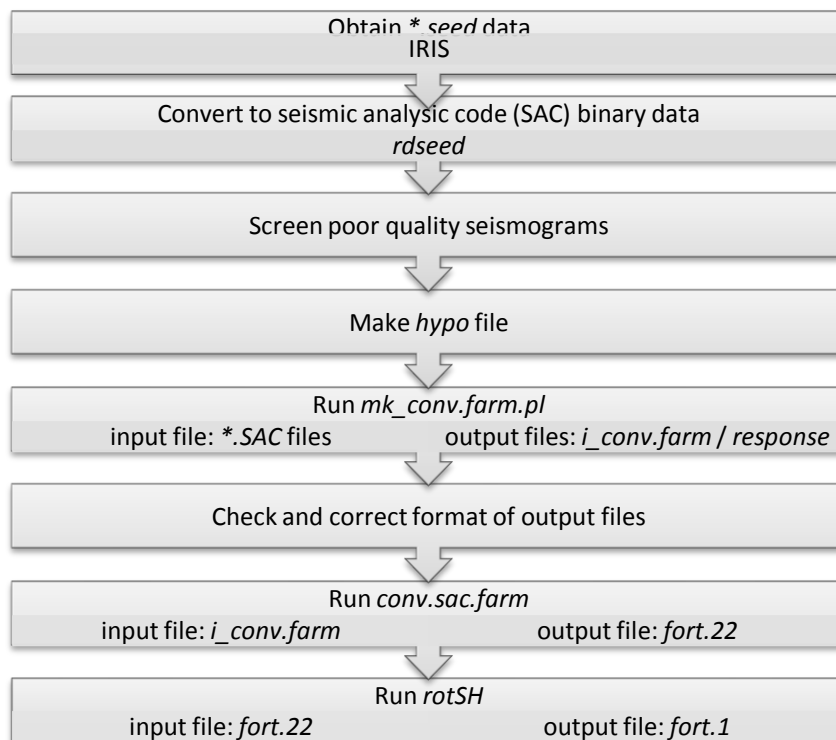


Fig. A.5.2 Representation of the data processing in order to obtain the teleseismic bodywave inversion program input file, *fort.1*.

Teleseismic bodywave inversion

General inversion

A point source is considered where the energy is released from a single point, the focus or hypocenter, since the observations are at a great distance compared to

the source dimensions. This approximation allows the calculation of Green's functions that are associated with the geometry between the station and the source. Experience and judgment are required, since inversion varies a lot with different event sizes, mechanisms etc.

The first step of the inversion process is to calculate the Green's function. For this, the Jeffreys and Bullen's seismic velocity model (J-B model) was used (given by Kikuchi and Kanamori, 2003) for the structure model of the station and the PP bounce point. For the determination of the crustal structure in the under study area, the regional velocity model proposed by Panagiotopoulos and Papazachos (1985) was used, being composed of two layers above a half space (Table A.3) plus a layer of water, the thickness of which changes (x) from 2 to 5 km depending on the area of the earthquakes studied here. The S-wave velocity was found using the ratio $V_p/V_s=1.78\pm 0.01$ (Panagiotopoulos and Papazachos, 1985; Nikolintaga *et al.*, 2007). Synthetic amplitudes were corrected for attenuation using Futterman's (1962) factor with $t^*=1s$ for P- and $t^*=4s$ for S-waves. It is important to note that, since the inversion depends on the depth of the reference point, h , if the depth at which the inversion is being carried out is wrong, the resulting focal mechanism will be incorrect. In order to obtain the appropriate depth, the same method was applied for a number of depths, keeping all the other parameters the same for every event. The final depth was determined by selecting the one with the minimum residual mean square error.

Table A.3 Crustal model of two layers above a half-space and a water layer (Panagiotopoulos and Papazachos, 1985; Nikolintaga *et al.*, 2007).

| P-wave velocity, V_p (km/s) | S-wave velocity, V_s (km/s) | Density, ρ (gr/cm ³) | Thickness, h (km) |
|----------------------------------|----------------------------------|---------------------------------------|------------------------|
| 1.5 | 0.0 | 1.0 | x |
| 6.0 | 3.37 | 2.65 | 19.0 |
| 6.6 | 3.7 | 2.94 | 12.0 |
| 7.9 | 4.43 | 3.26 | 0.0 |

The Green's function is found by running the program *green*, giving as input the file *i_green*. The Green's functions are calculated in the frequency domain, supposing a point source located on a rupture plane. The parameters for the file are shown in Fig. A.5.3. NT is the number of points given as a power of two, DT is the sampling interval, H0 is the depth of the reference point and the rest of the parameters determine the down-dip location of the point sources to be placed on a dipping plane.

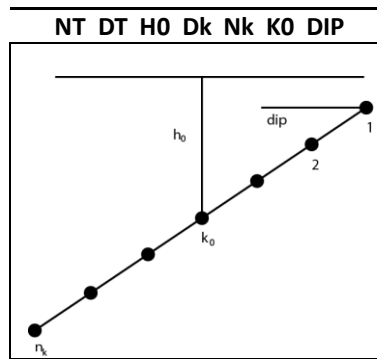


Fig. A.5.3 Top: Input file *i_green* for the calculation of the Green's functions. NT is the number of points given as a power of two, DT is the sampling interval, H0 is the depth of the reference point and the rest of the parameters determine the down-dip location of the point sources to be placed on a dipping plane. Bottom: Linear distribution of the point sources (modified from Kikuchi and Kanamori, 1991). h_0 is the depth of the reference point, n_k is the n -th point source, dk is the interval between every point source and k_0 is the location of the reference point.

In order to proceed with the inversion, the output file of the *green* program is necessary (*fort.3*) which contains the calculated green's functions for the synthetic seismograms in binary format, as well as the output file of the data preparation process (*fort.1*) and the *i_inversion* file, which contains the parameters for the inversion. The focal mechanism solution is obtained by minimizing the difference between the synthetic and the observed data (seismograms).

In Fig. A.5.4 the parameters of the *i_inversion* file are listed, on the left. ID is the identification of the event, Tw is the duration of the data to be inverted, Vr is the maximum rupture speed, Ms is the type chosen for the source time function, T1 is the rise time and T2 is the rise time plus duration of slip, Ne is the number of subvents for the source time function, Te is the time interval for the grid search of each subevent, Ns is the number of waveforms to be inverted and FC(j) the weight for each waveform, Idly is the shift of the data in sampling points, Isr and IFP are parameters controlling the type of source and the geometry of grid scheme, respectively. If IFP=0, then Nlen is the number of grid points, R the distance and Fi the azimuth. If IFP=1, Str is the strike, DI is the grid spacing, NI the number of grid points and L0 the index of the reference point, hence the epicenter (Fig. A.5.4, right).

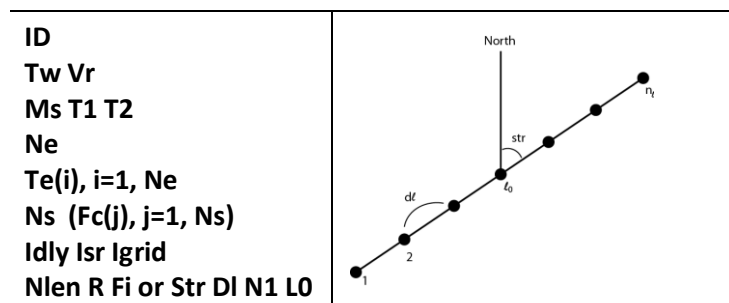


Fig. A.5.4 Left: *i_inversion* file parameters (for explanation, see text). Right: Geometry of grid scheme in *i_inversion* (modified from Kikuchi and Kanamori, 1991).

Fixed mechanism inversion

With this second set of programs, the data are inverted using a fixed mechanism for the determination of the distribution of the rupture on the fault plane. The source time function and the location of the sources are deduced. The procedure is similar to that of the general inversion. If, from the result of the first inversion, no significant change in the mechanism is observed, this second inversion may be used to refine the rupture pattern. An input file with specific parameters is required (Table A.4). The parameters are the same as is *i_green*, with the addition of the Str (strike), Dip (dip) and Rak (rake). The preliminary mechanism taken as reference in this second inversion is the one obtained by the first motion of P-waves at each station, determined with MECSTA (Udías *et al.*, 1984).

Table A.4 Input file *i_green3*. Str, Dip, Rak stand for the fault plane solution of the earthquake. All other parameters are the same as in Fig. A.5.3.

| |
|--------------------------------------|
| NT DT Str Dip Rak H0 Dk Nk K0 |
|--------------------------------------|

Once the Green's functions are obtained, the inversion is carried out. The input file is the *i_inversion3* (Table A.5), which has similar, but fewer parameters. The only significant change is that in this file, the strike of the fault is missing, since it is incorporated in the *i_green3* file (Table A.4).

Table A.5 Inversion input file *i_inversion3*. For explanation of the parameters, see Fig. A.5.4.

| |
|--------------------------|
| ID |
| Tw Vr Te |
| Ms T1 T2 |
| Ne |
| DI NI LO |
| ldly |
| Ns, (Fc, j=1, Ns) |

Some of the aforementioned parameters had values that changed for every event, in order to best describe the source time function and fault mechanism. Such parameter are the thickness of the water column, the focal depth, the reference fault plane solution and the parameter controlling the source time function (rise time, duration, number of asperities etc.). On the other hand, some parameters remained unchanged, since they are the same for earthquakes striking within a small region. These are the rupture velocity, which for a range of 2.4 to 3.0 km/s produced the same source time function and fault plane solutions, the weights of the P and SH waves (1 and 0.2, respectively), the double couple assumption etc.

APPENDIX B: TELESEISMIC STATIONS

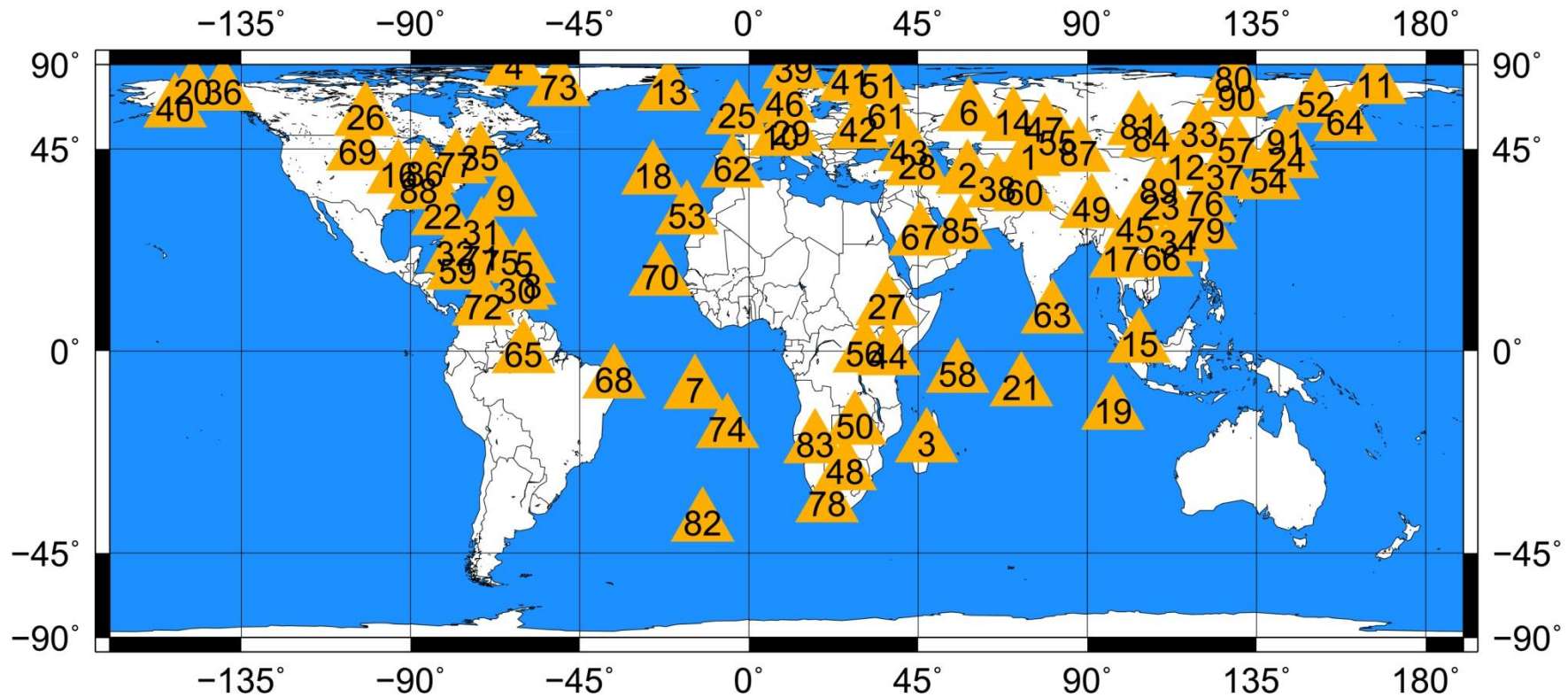


Fig. B.1 World map showing the teleseismic IRIS station between 10° and 90° epicentral distances, used for the bodywave inversion in this study. Station names are listed in Table A.1.

The code name of every station cited in Chapter 3 results from the network of each station (i.e. II), its code name (i.e. AAK) and the instrument code number (i.e. 00) resulting in II.AAK.00, for example.

Table B.1 Station identification number with the station name, network, latitude and longitude and region. Epicentral distance is not given, since it changes for every earthquake. CU: Caribbean Network (USGS); USGS National Earthquake Information Center (NEIC); GT: Global Telemetered Seismograph Network (USAF/USGS), Albuquerque Seismological Laboratory (ASL)/USGS; IC: New China Digital Seismograph Network, Albuquerque Seismological Laboratory (ASL)/USGS; II: Global Seismograph Network (GSN-IRIS/IDA); Scripps Institution of Oceanography (SIO); IM: International Miscellaneous Stations: None; IU: Global Seismograph Network (GSN-IRIS/USGS); Albuquerque Seismological Laboratory (ASL)/USGS.

| | Station | Network | Latitude | Longitude | Region |
|-----------|----------------|----------------|-----------------|------------------|---|
| 1 | AAK | II | 42.64 | 74.49 | Ala Archa, Kyrgistan |
| 2 | ABKT | II | 37.93 | 58.12 | Alibek, Turkmenistan |
| 3 | ABPO | II | -19.02 | 47.23 | Ambohimpanompo, Madagascar |
| 4 | ALE | II | 82.50 | -62.35 | Alert, N.W.T., Canada |
| 5 | ANWB | CU | 17.67 | -61.79 | Willy Bob, Antigua and Barbuda |
| 6 | ARU | II | 56.43 | 58.56 | Arti, Russia |
| 7 | ASCN | II | -7.93 | -14.36 | Butt Crater, Ascension Island |
| 8 | BBGH | CU | 13.14 | -59.56 | Gun Hill, Barbados |
| 9 | BBSR | IU | 32.37 | -64.70 | Bermuda Institute of Ocean Sciences, St. George |
| 10 | BFO | II | 48.33 | 8.33 | Black Forest Observatory, Schiltach, Germany |
| 11 | BILL | IU | 68.07 | 166.45 | Bilibino, Russia |
| 12 | BJT | IC | 40.02 | 116.17 | Baijiatuan, Beijing, China |
| 13 | BORG | II | 64.75 | -21.33 | Borgarfjordur, Asbjarnarstadir, Iceland |
| 14 | BRVK | II | 53.06 | 70.28 | Borovoye, Kazakhstan |
| 15 | BTDF | MS | 1.36 | 103.77 | Bukit Timah Dairy Farm, Singapore |
| 16 | CCM | IU | 38.06 | -91.24 | Cathedral Crave, Missouri, USA |
| 17 | CHTO | IU | 18.81 | 98.94 | Chiang Mai, Thailand |
| 18 | CMLA | II | 37.76 | -25.52 | Cha de Macela, Sao Miguel Island, Azores |
| 19 | COCO | II | -12.19 | 96.83 | West Island, Cocos (Keeling) Islands |
| 20 | COLA | IU | 64.87 | -147.86 | College Outpost, Alaska, USA |
| 21 | DGAR | II | -7.41 | 72.45 | Diego Garcia, Chagos Islands, Indian Ocean |
| 22 | DWPF | IU | 28.11 | -81.43 | Disney Wilderness Preserve, Florida, USA |
| 23 | ENH | IC | 30.28 | 109.49 | Enshi, Hubei Province, China |
| 24 | ERM | II | 42.02 | 143.16 | Erimo, Hokkaido Island, Japan |
| 25 | ESK | II | 55.32 | -3.21 | Eskalemuir, Scotland, UK |
| 26 | FFC | II | 54.73 | -101.98 | Flin Flon, Canada |
| 27 | FURI | IU | 8.9 | 36.68 | Mt. Furi, Ethiopia |
| 28 | GNI | IU | 40.15 | 44.74 | Garni, Armenia |
| 29 | GRFO | IU | 49.69 | 11.22 | Grafenberg, Germany |
| 30 | GRGR | CU | 12.13 | -61.65 | Grenville, Grenada |
| 31 | GRTK | CU | 21.51 | -71.13 | Grand Turk, Turks and Caicos Islands |
| 32 | GTBY | CU | 19.93 | -75.11 | Guantanamo Bay, Cuba |
| 33 | HIA | IC | 49.27 | 119.74 | Hailar, Neimenguu Autonomous Region, China |
| 34 | HKPS | HK | 22.28 | 114.14 | Po Shan, Hong Kong |

| | | | | | |
|----|------|----|--------|---------|---|
| 35 | HRV | IU | 42.51 | -71.56 | Adam Dzewonski Observatory (Oak Ridge), Massachusetts |
| 36 | IL31 | IM | 64.77 | -146.86 | ILAR Array, Elison, AK, USA |
| 37 | INCN | IU | 37.48 | 126.62 | Inchon, Republic of Korea |
| 38 | KBL | IU | 34.54 | 69.04 | Kabul, Afghanistan |
| 39 | KBS | IU | 78.92 | 11.94 | Ny-Alesund, Spitzbergen, Norway |
| 40 | KDAK | II | 57.78 | -152.58 | Kodiak Island, Alaska, USA |
| 41 | KEV | IU | 69.76 | 27.00 | Kevo, Finland |
| 42 | KIEV | IU | 50.7 | 29.22 | Kiev, Ukraine |
| 43 | KIV | II | 43.96 | 42.69 | Kislovodsk, Russia |
| 44 | KMBO | IU | -1.13 | 37.25 | Kilima Mbongo, Kenya |
| 45 | KMI | IC | 25.12 | 102.74 | Kunming, Yunnan Province, China |
| 46 | KONO | IU | 59.65 | 9.6 | Kongsberg, Norway |
| 47 | KURK | II | 50.72 | 78.62 | Kurchatov, Kazakhstan |
| 48 | LBTB | GT | -25.02 | 25.60 | Lobaste, Botswana, Africa |
| 49 | LSA | IC | 29.70 | 91.13 | Tibet, China |
| 50 | LSZ | IU | -15.28 | 28.19 | Lusaka, Zambia |
| 51 | LVZ | II | 67.90 | 34.65 | Lovozero, Russia |
| 52 | MA2 | IU | 59.58 | 150.77 | Magadan, Russia |
| 53 | MACI | IU | 28.25 | -16.51 | Morro de la Arena, Canary Islands |
| 54 | MAJO | IU | 36.55 | 138.20 | Matsuhira, Japan |
| 55 | MAKZ | IU | 46.81 | 81.98 | Makanchi, Kazakhstan |
| 56 | MBAR | II | -0.60 | 30.74 | Mbarara, Uganda |
| 57 | MDJ | IC | 44.62 | 129.59 | Mudanjiang, Heilongjiang Province, China |
| 58 | MSEY | II | -4.67 | 55.48 | Mahe, Seychelles |
| 59 | MTDJ | CU | 18.23 | -77.53 | Mount Denham, Jamaica |
| 60 | NIL | II | 33.65 | 73.27 | Nilore, Pakistan |
| 61 | OBN | II | 55.11 | 36.57 | Obninsk, Russia |
| 62 | PAB | IU | 39.54 | -4.35 | San Pablo, Spain |
| 63 | PALK | II | 7.27 | 80.70 | Pallekele, Sri Lanka |
| 64 | PET | IU | 53.02 | 158.65 | Petropavlovsk, Russia |
| 65 | PTGA | IU | -0.73 | -59.97 | Pitinga, Brazil |
| 66 | QIZ | IC | 19.03 | 109.84 | Qionzhong, Hainan Province, China |
| 67 | RAYN | II | 23.52 | 45.50 | Ar Rayn, Saudi Arabia |
| 68 | RCBR | IU | -5.83 | -35.90 | Riachuelo, Brazil |
| 69 | RSSD | IU | 44.12 | -104.04 | Black Hills, South Dakota, USA |
| 70 | SACV | II | 14.97 | -23.61 | Santiago Island, Capo Verde |
| 71 | SDDR | IU | 18.98 | -71.29 | Presa de Sabenta, Dominican Republic |
| 72 | SDV | IU | 8.88 | -70.63 | Santo Domingo, Venezuela |
| 73 | SFJD | IU | 67.00 | -50.62 | Sondre Stromfjord, Greenland |
| 74 | SHEL | II | -15.96 | -5.75 | Horse Pasture, St. Helena Island |
| 75 | SJG | IU | 18.11 | -66.15 | San Juan, Puerto Rico |
| 76 | SSE | IC | 31.09 | 121.19 | Shanghai, China |
| 77 | SSPA | IU | 40.64 | -77.89 | Standing Stone, Pennsylvania |
| 78 | SUR | II | -32.38 | 20.81 | Sutherland, South Africa |
| 79 | TATO | IU | 24.97 | 121.50 | Taipei, Taiwan |

| | | | | | |
|-----------|------|----|--------|--------|--|
| 80 | TIXI | IU | 71.63 | 128.87 | Tiksi, Russia |
| 81 | TLY | II | 51.68 | 103.64 | Talaya, Russia |
| 82 | TRIS | IU | -37.07 | -12.32 | Tristan da Cunha |
| 83 | TSUM | IU | -19.20 | 17.58 | Tsumeb, Namibia |
| 84 | ULN | IU | 47.87 | 107.05 | Ulanbaatar, Mongolia |
| 85 | UOSS | II | 24.95 | 56.20 | University of Sharjah, Sharjah, United Arab Emirates |
| 86 | WCI | IU | 38.23 | -86.29 | Wyandotte Cave, Indiana, USA |
| 87 | WMQ | IC | 43.81 | 87.70 | Urumqi Xinjiang Province, China |
| 88 | WVT | IU | 36.13 | -87.83 | Waverly, Tennessee, USA |
| 89 | XAN | IC | 34.03 | 108.92 | Xi'an, China |
| 90 | YAK | IU | 62.03 | 129.68 | Yakutsk, Russia |
| 91 | YSS | IU | 46.96 | 142.76 | Yuzhno Sakhalinsk, Russia |